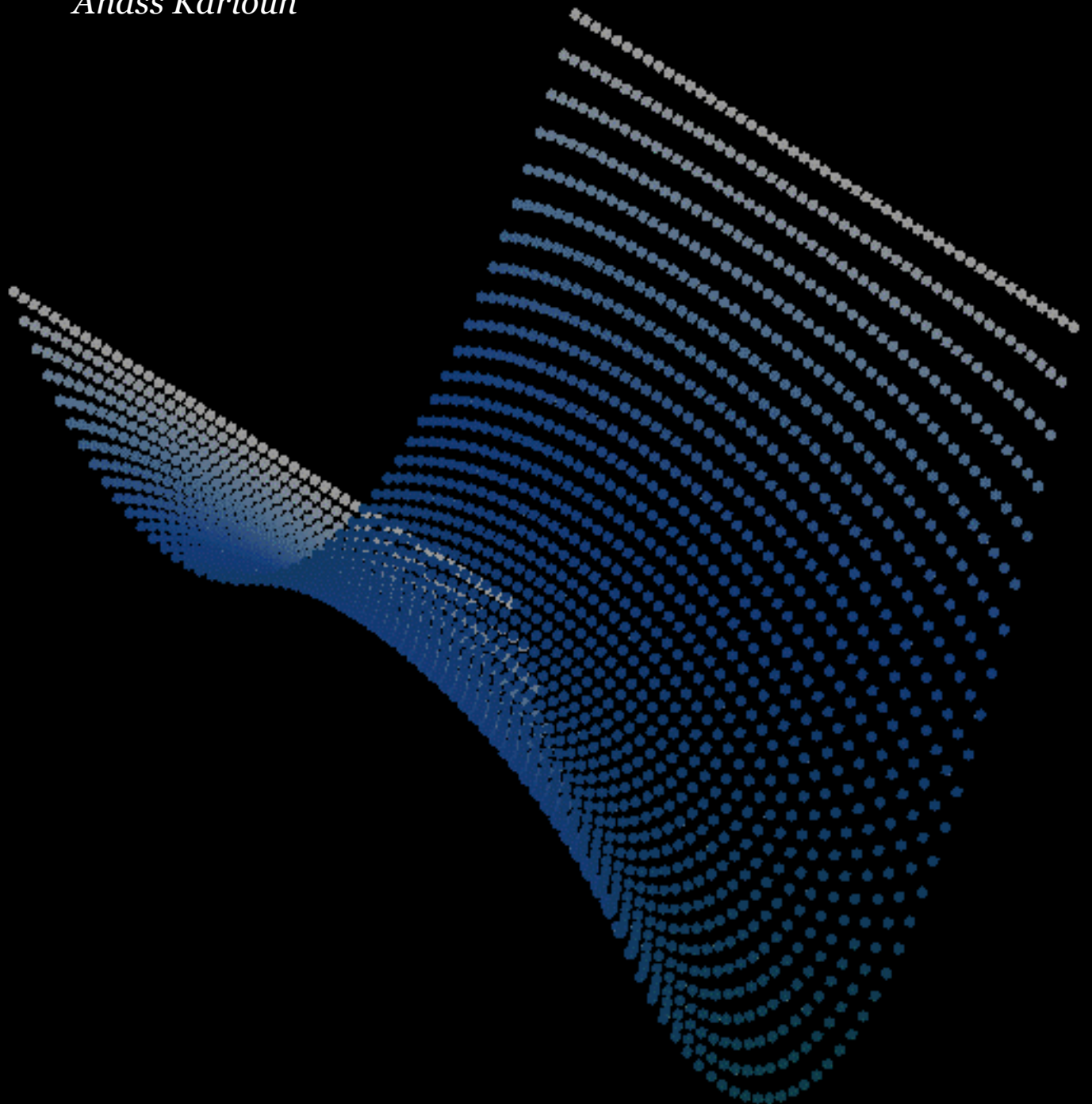


# FLEXIBLY FORMED CONCRETE

Exploiting the deformation behaviour of weft-knitted formworks caused by concrete pressure

*Anass Kariouh*





# **Flexibly formed concrete**

**Exploiting the deformation behaviour of weft-knitted  
formworks caused by concrete pressure**

*A thesis submitted in partial fulfilment for the degree of*

Master of Science (MSc)

from the Delft University of Technology

*presented by*

**Anass Kariouh**

born on 07.09.1998

citizen of Morocco and the Netherlands

*accepted on the recommendation of*

Dr. Mariana Popescu

Dr. ir. Yuguang Yang

Dr. ir. Andrei Faragau

Dr. ir. Athanasios Tsetas

2023



# Abstract

To reduce the construction industry's negative influence on global climate, emissions related to concrete consumption need to be addressed. This implies reducing the amount of concrete used, by creating material-efficient structures. One of concrete's main advantages is that it can be moulded into virtually any shape. Despite the fact that modern digital design tools enable the effortless design and calculation of lightweight and graceful structures, this potential often goes unrealised. This can be attributed to the challenges associated with constructing intricate and custom geometries using conventional formwork techniques that depend on single-use cut timber or milled foam. Not only do these methods make the construction of these types of structures labour and cost intensive, they also cause them to be wasteful.

KnitCrete, which uses knitted technical textiles as stay-in-place moulds for concrete structures, has proven to be a solution for building doubly curved structures, eliminating the need for time-consuming, costly, and wasteful moulds. However, due to its inherent high flexibility and the challenges of predicting and controlling the geometry during the casting process, the technology relies on coating procedures using high-strength cement paste coating to stiffen the geometry before concrete can be poured.

This research addresses both issues and proposes a design approach, which models the deformation behaviour of the uncoated knitted formwork under concrete pressure to determine the final geometry of flexibly formed concrete structures, hence gaining better understanding on the deformation behaviour of knitted textile formworks and bypassing the stiffening steps during fabrication.

Developing a method to predict the final geometry of flexibly formed concrete structures involves various research disciplines, including material science, and structural mechanics. The research approach is divided into three parts. The first part investigates the stress-strain relationship of various textiles with different knitting patterns, alongside the rheological and mechanical strength properties of different cementitious mixtures. The second stage focuses on developing (semi-)analytical models to predict the deflection behaviour of membranes subjected to varying boundaries, loads, and material properties. Finally, the accuracy of the models are validated by the construction of multiple prototypes.

In conclusion, this thesis introduces a fabrication system that exploits the deflection behaviour of flexible formworks to create funicular shell structures and lays the foundation for implementing (semi-)analytical approaches to model these deformations.

# Acknowledgements

I want to start off by saying that all praise is due to Allah. If it was not for Him, I would not be where I am today, and I would not have been blessed with all the amazing people that have contributed directly and indirectly to this thesis.

I cannot thank my chair, Dr. Mariana Popescu, enough for all her continuous guidance, support, and availability throughout this project. Mariana, you are a great inspiration to me – not only are you a great mentor, but even a greater human being. I hope our work together does not end here and that we will work on great projects in the future. I would also like to extend my gratitude to Dr. ir. Yuguang Yang for his enthusiastic attitude towards this project, and for all his technical advice and critical questions during our meetings. I want to express my appreciation to Dr. ir. Andrei Faragau and Dr. ir. Athanasios Tsetas for their pivotal help in the modelling part of the thesis. In the short time we have worked together, I have learned so much from you both, and if it weren't for you, I would have never come as far as I did.

I would like to thank my colleague in the Tailored Materiality Research group, Nikoletta Christidi, for always being willing to assist me with the knitting part of my research.

Furthermore, I want to thank my brothers Anas Abbasi, Daa Abbasi, Oguzhan Kobya, and Mohammed Suleman, for making my time at the university more pleasant and spiritually uplifting. Another special thank you goes to my brothers Ufuktan Kilinc and Romano van Teijlingen, who have been true sources of support and laughter for over a decade now.

Finally, I want to express my love and gratitude to my family, and more specifically my parents Kenza and Youssef Kariouh. I would not be the man I am today if it were not for you. You have raised me, nurtured me, taught me, loved me, and always supported me – and I am forever grateful for that. I hope I have made you proud.

# Contents

Abstract.....	v
Acknowledgements .....	vi

## I. Introduction

1. Introduction .....	3
1.1 Context.....	3
1.2 Problem statement and research objectives .....	5
1.3 Project plan.....	6
1.4 Thesis structure.....	7
2. State of the art .....	8
2.1 Form finding .....	8
2.1.1 Physical form finding .....	9
2.1.2 Computational form finding .....	11
2.2 Numerical and analytical methods .....	13
2.2.1 Finite element method.....	13
2.2.2 Semi-analytical method .....	14
2.3 Formwork systems .....	15
2.3.1 Subtractive moulding methods.....	15
2.3.2 Adaptable moulds .....	17
2.3.3 Additive manufacturing.....	18
2.3.4 Fabric formworks .....	22
2.4. Summary .....	25

## II. Approach

3. Methodology .....	29
3.1 Overview .....	29
3.2 Material characterisation.....	31
3.3 Membrane modelling.....	31

3.4 Prototyping .....	32
4. Material characterisation .....	33
4.1 Knit properties .....	33
4.1.1 Knit design and sample preparation .....	33
4.1.2 Biaxial test configuration .....	35
4.1.3 Derivation of the material properties .....	36
4.1.4 Results and discussion .....	37
4.2 Mortar properties .....	41
4.2.1 Mixture design and sample preparation .....	41
4.2.2 Flexural and compressive test configuration .....	43
4.2.3 Results and discussion .....	45
5. Membrane model .....	49
5.1 Introduction to membrane theory .....	49
5.2 Derivation of vertical equilibrium equation for uniformly loaded rectangular membranes .....	50
5.3 Derivation of linear membrane deflection solution .....	51
5.3.1 Assumptions .....	52
5.3.2 Linear solution .....	52
5.4 Derivation of nonlinear membrane deflection solution .....	53
5.4.1 Energy-method solution .....	55
5.4.2 Fourier series expansion method .....	56
 <b>III. Results</b>	
6. Prototypes .....	61
6.1 Prototyping framework and construction strategy .....	61
6.1.1 System .....	61
6.1.2 Prefabrication .....	63
6.1.3 Construction .....	64
6.2 Squared shell .....	66
6.2.1 Design .....	66
6.2.2 Model .....	66
6.2.3 Measurement and comparison .....	69
6.3 Rectangular shell .....	71



6.3.1 Design.....	72
6.3.2 Model.....	72
6.3.3 Measurement and comparison.....	73
6.4 Discussion.....	75
<b>IV. Reflection</b>	
7. Discussion .....	79
7.1 Design.....	79
7.2 Construction .....	80
8. Conclusions .....	81
8.1 Contributions.....	81
8.1.1 Material characterisation .....	81
8.1.2 Membrane modelling .....	82
8.1.3 Prototyping.....	82
8.2 Advantages .....	82
8.3 Limitations .....	83
8.4 Future work.....	85
Bibliography.....	87





**Part I:  
Introduction**



# 1. Introduction

## 1.1 Context

Concrete is the most used construction material due to its cost-effectiveness and widespread availability, with approximately 2.8 Gt of cement produced annually worldwide (Schneider et al., 2011). This extensive consumption results in cement accounting for 5-8% of global carbon emissions (Castaldelli et al., 2014). As the global urban population is projected to increase by 2.5 billion by 2050 (Swilling et al., 2018), concrete's role and impact as a building material becomes crucial in meeting the growing infrastructure demands, especially in emerging economies (Uratani & Griffiths, 2023). Structural engineers play a critical role in achieving an environmentally sustainable society, as the responsibility for minimising concrete's ecological footprint intensifies. Apart from material-level innovations such as reducing cement and clinker content or enhancing carbon capture, optimising structural design can significantly contribute to reducing material usage and improving the ecological impact of concrete structures (Gibbons & Orr, 2020).

Form finding methods have been demonstrated by prominent architects and engineers like Heinz Isler, Eduardo Torroja, and Félix Candela to enable materially-efficient structural design, as depicted in Figure 1.1. These innovative approaches led to the creation of funicular(-like) structures such as vaults, domes, and shells, characterised by their efficient load transfer over large spans (Adriaenssens et al., 2014), resulting in lightweight and material-efficient constructions. However, the construction of such structures often requires custom-made formworks, a costly, time-consuming, and labour-intensive process, constituting up to 70% of construction expenses (García de Soto et al., 2018). Moreover, these formworks are frequently used only once, leading to significant construction waste. Consequently, the construction industry has increasingly adopted geometrically simpler (monolithic) elements, like flat slabs with constant depths, using standardised formworks. This shift prioritises economic optimisation in the construction process rather than reducing the embodied carbon footprint (Mata-Falcón et al., 2022).

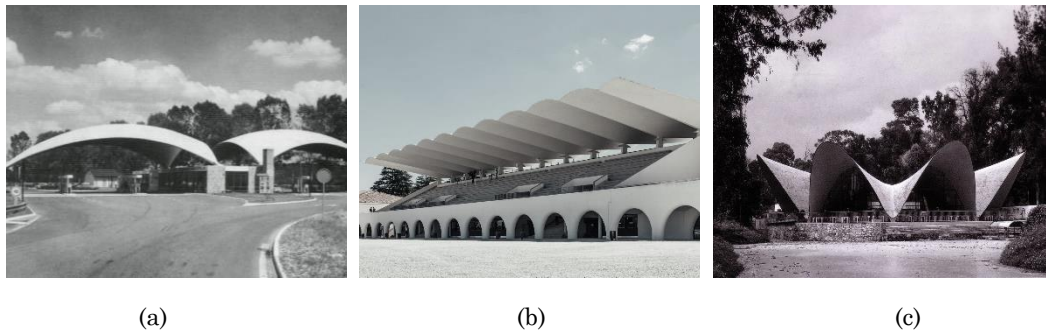


**Figure 1.1:** Material-efficient structures by prominent architects and engineers: (a) Service Station by Heinz Isler, Deitingen, Switzerland, 1965; (b) La Zarzuela Racetrack by Eduardo Torroja, Madrid, Spain, 1930; (c) Los Manantiales Restaurant by Félix Candela, Xochimilco Mexico, 1958 (photo credit: (a) ETH Zurich; (b) Ximo Michavila; (c) RIBA Collections).

Digital fabrication offers architects and structural engineers the ability to create intricate and customised shapes in a fast and less labour-intensive manner. Consequently, this leads to a lower carbon footprint and improved sustainability through reduced concrete consumption and waste production. Digital fabrication for concrete(-like) structures is performed in various ways. A considerable amount of research has focused on digital fabrication of concrete using direct extrusion 3D printing, with several review articles covering the topic (Bos et al., 2016; Wangler et al., 2016). However, this method has inherent geometric limitations, such as restricted building heights, volumes, and cantilevers (Jipa & Dillenburger, 2022). Additionally, 3D printing fails to fully capitalise on fresh concrete's mouldability. In contrast, digital fabrication of formworks address this issue by moulding concrete into bespoke shapes (Jipa & Dillenburger, 2022). Some examples of these digitally fabricated formworks are, computer numerically controlled (CNC) milled or hot wire cut moulds, adaptable moulds, 3D printed formworks and fabric formworks. Specifically, weft-knitted formworks, created using CNC knitting machines, enable the fabrication of custom double-curved geometries by varying the textiles width and length through the addition or removal of loops within the knit architecture, enabling the realisation of non-developable shapes and spatial features (Lee, 2023).

KnitCrete is an example of flexible formwork technology that uses weft-knitted textiles to fabricate intricate concrete structures with unconventional geometries (Popescu, 2019). The versatility of this approach has been demonstrated in both small-scale and large-scale projects. Notable examples include the KnitCrete Bridge (Figure 1.2a), a 1.2 x 2.1 x 0.26 m shell bridge prototype (Popescu et al., 2018), and the KnitNervi pavilion (Figure 1.2b), with a circular outer diameter and maximum height of 9 m and 3.5 m, respectively (Scheder-Bieschin et al., 2023). Nevertheless, the technology still relies on gradually stiffening and strengthening the textile using a high-strength cement paste coating to support the casting of concrete with minimal deformation. This is due to the inherent challenges in predicting and controlling the geometry while pouring the concrete and calculating the final deformed shape with these flexible systems. Nonetheless, there remains an aspiration to employ this flexible formwork technology, bypassing the coating step, particularly for cases where deformations during the casting process are integral to the design.

Therefore, developing an accurate deformation modelling strategy is crucial for effectively designing and realising the desired final geometries while also capitalising on the system's flexibility which allows for the creation of specific (funicular) structural shapes.



**Figure 1.2:** Structures built using KnitCrete: (a) KniCrete Bridge, Zurich, Switzerland, 2018; (b) KnitNervi, Rome, Italy, 2022 (photo credit: (a) BRG; (b) Mariana Popescu)

## 1.2 Problem statement and research objectives

Currently there is no established method for predicting the deformation behaviour of weft-knitted textile formworks. This thesis explores the potential of modelling this deformation behaviour for different boundary shapes, load cases and textile properties.

The main objective of this research is to:

*Determine the final geometry of flexibly formed concrete structures by modelling the deformation behaviour of the uncoated knitted formwork under concrete pressure.*

To achieve this objective, several sub-goals are pursued:

- **Design:** establish a forming system that facilitates the fabrication of funicular concrete(-like) structures and eliminates the need for single-use wasteful custom formworks.
- **Characterization:** fabricate and test samples to get a fundamental understanding of the material behaviour of different knit architectures and mortar mixture designs.
- **Modelling:** create a modelling workflow consisting of a set of equilibrium equations that are solved (semi-)analytically to predict the deflection behaviour of weft-knitted membranes for different loads and boundaries.
- **Construction:** validate the moulding system and deflection model by building physical prototypes and comparing the resulting geometries with the shapes predicted by the models.

## 1.3 Project plan

Figure 1.3 provides an overview of the research plan, which comprises three distinct parts. The first part includes the material characterization of diverse cementitious mixture designs (Figure 1.3a) and knitting patterns (Figure 1.3b). This phase is dedicated to acquiring mechanical properties of the materials, serving as vital input parameters for the deflection model. The subsequent part involves the development of the deflection model (Figure 1.3c) aimed at predicting knitted fabric membrane deflection under hydrostatic loads. Lastly, the model's validation is conducted by comparing its outcomes with those of physically constructed prototypes (Figure 1.3d), which are fabricated using the developed formwork system. The conglomeration of findings from all three parts are used to provide comprehensive recommendations and conclusions concerning the forming system and models (Figure 1.3e).

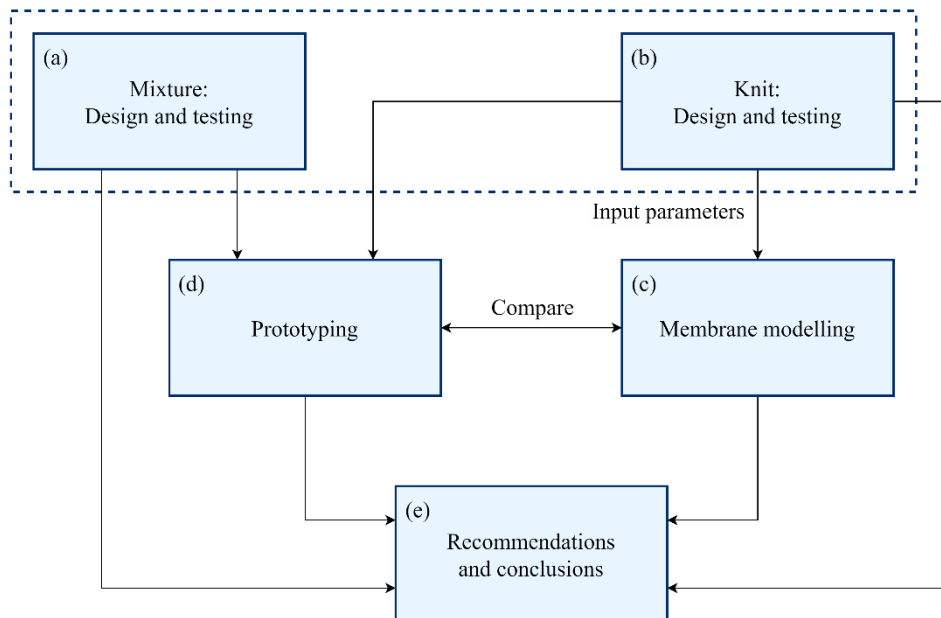


**Figure 1.3:** Overview of research project: (a) cementitious mix characterisation; (b) knit characterisation; (c) membrane modelling; (d) physical prototyping; (e) Final recommendations and conclusion.



## 1.4 Thesis structure

The thesis is structured into four parts, each addressing specific aspects of the research. Part I serves as an introduction, commencing with Chapter 1, which provides an overview of the research topic, outlines the research objectives and the proposed project plan. Following that, Chapter 2 presents the current state of the art, identifying key findings in the field.

Part II delves into the methodological details of the research. Chapter 3 presents a comprehensive overview of methodology. Chapter 4 focuses on the material characterization approaches used during the research, highlighting the methods employed to analyse the properties of the materials. Chapter 5 elaborates on the analytical and numerical methodologies used in the modelling approach.

Part III revolves around prototyping and validating. Chapter 6 showcases the prototypes created throughout the research. Furthermore, it provides a critical comparison between the theoretical models developed and the practical outcomes achieved with the prototypes.

Finally, Part IV offers a reflective analysis of the contributions made by the research. Chapter 7 introduces a structured thinking exercise, aimed at obtaining a more profound comprehension of the research findings and their practical applicability. It explores the nuances of how the findings can be effectively applied in real-world scenarios. Chapter 8 evaluates the research's implications and potential applications. Moreover, it explores possible avenues for future work, suggesting areas where further investigation and improvements could be pursued.

## 2. State of the art

This chapter provides an overview of various design methods employed throughout history and in contemporary practice to achieve the intricate geometries of concrete shell structures. Additionally, it delves into the latest formwork advancements in concrete construction essential for realising bespoke geometries. Section 2.1 offers an overview of existing form finding methods, focusing on both traditional physical techniques from the past and the state-of-the-art computational methods currently in use. Section 2.2 introduces alternative design approaches using numerical and analytical analysis methods. Section 2.3 presents an overview of existing formwork systems, focussing on the emergence of novel subtractive and additive digital fabrication approaches, as well as adaptable and flexible formwork systems that have recently come into prominence.

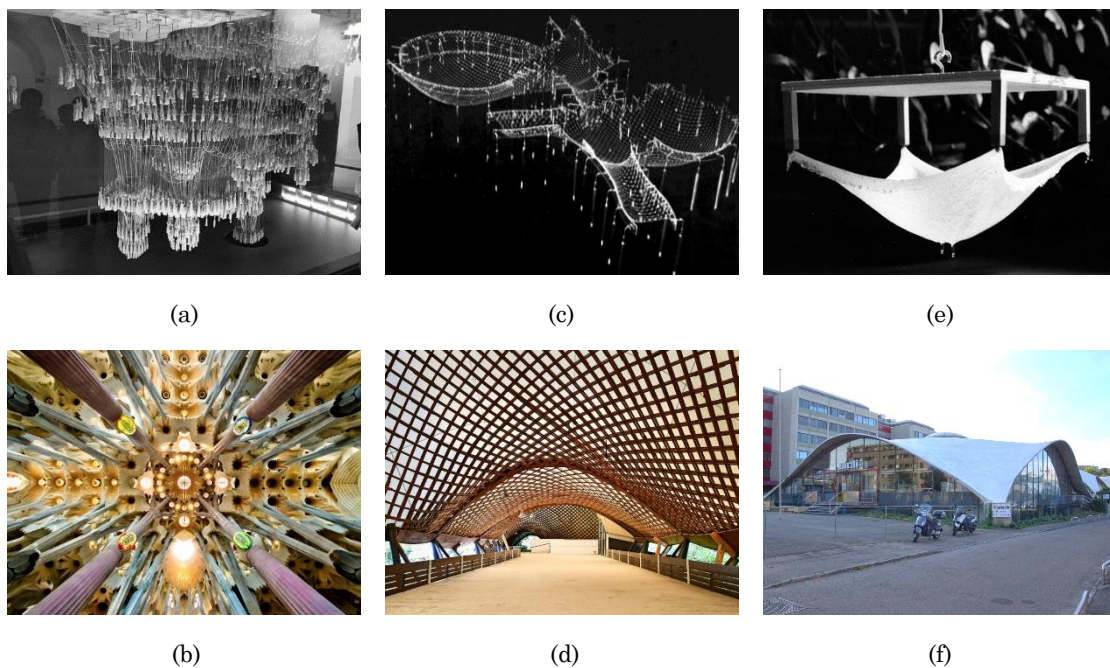
### 2.1 Form finding

Form finding is an iterative procedure whereby the design parameters of a structural design keep getting altered until the ‘optimal’ design is found that provides a state of static equilibrium for the given design load (Adriaenssens et al., 2014). Form finding methods exhibit wide applicability across various applications and materials, such as gridshells, tension structures, lightweight architectures, fabric membranes, and cable-supported systems. However, in the realm of concrete construction, their primary role lies in the design of shell structures. This is achieved through either the direct design of concrete structures primarily subject to compression loads or by determining the shape of supporting structures like gridshells or membrane systems, which serve as formwork for the eventual casted concrete structure.

Two eminent methods for form finding of concrete shell structures are the physical form finding methods and computational form finding methods. Physical form finding procedures often involve the fabrication of small scale prototypes, such as hanging models, soap film models, and to a lesser extent, pneumatic models. These prototypes are crafted to provide valuable insights into the intended equilibrium shape. Computational form finding methods involve using mathematical and computational techniques to determine the shape of the structure. Some of the more well known and established computational form finding methods are the dynamic relaxation method (Happold & Liddell, 1975), the force density method (Linkwitz & Schek, 1971), and the particle-spring system (Ochsendorf & Kilian, 2005). Additionally, finite element analyses (FEA) and (semi-)analytical approaches can be used to find the resulting shape of structures that necessitate deformations prior to achieving their final geometry.

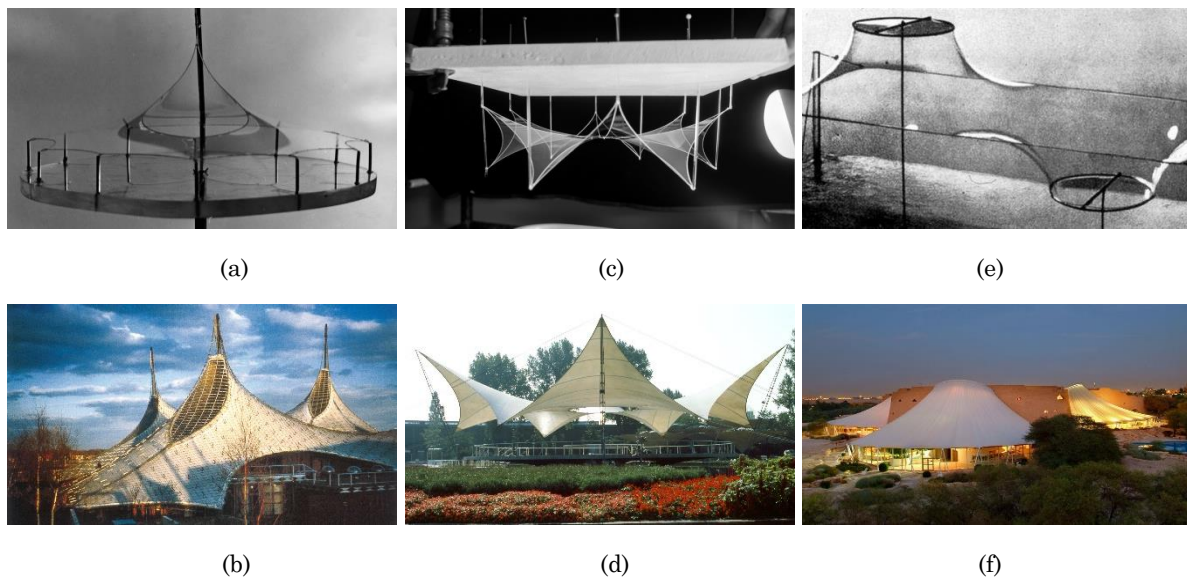
### 2.1.1 Physical form finding

Hanging model experiments involve subjecting a chain or flexible membrane to a form determining load case, resulting in a catenary shape characterised by pure tension and no bending (Ramm, 1991). This shape can be inverted to obtain the form for a shell with a pure compression stress state. Architects and engineers have historically employed this form finding technique for various materials. For instance, Antoni Gaudí used the hanging model principle for the vaulted ceiling design of the Sagrada Familia (Figure 2.1a-b), constructed using masonry and natural stone. Similarly, Frei Otto employed a hanging chain net model for the funicular design of the Mannheim Multihalle gridshell (Figure 2.1c-d), predominantly composed of timber elements. Heinz Isler employed hanging membranes to create efficient and economical concrete shell structures, as exemplified by the SICLI pavilion (Figure 2.1e-f).



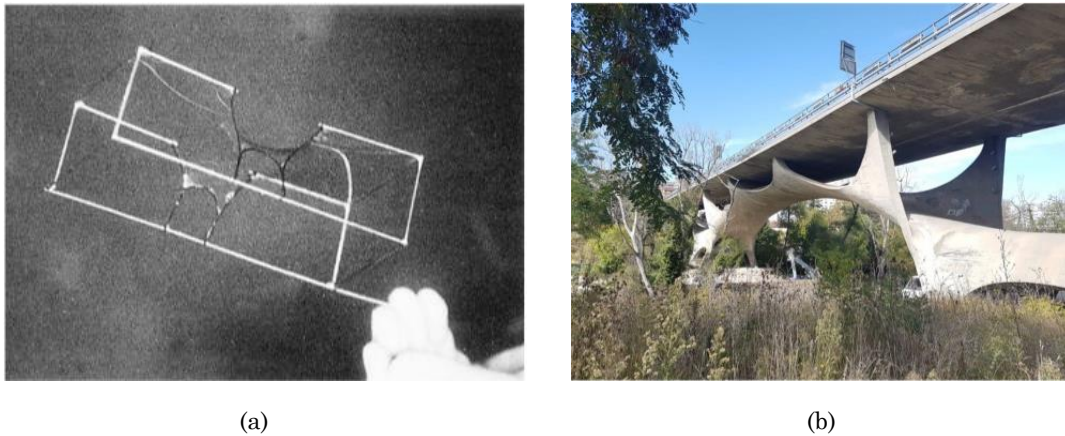
**Figure 2.1:** Examples of hanging models and the final structures that resulted from them: (a) Recreation of Antoni Gaudí's hanging model for the Sagrada Familia; (b) Vaulted ceiling of the Sagrada Familia by Antoni Gaudí, Barcelona, Spain; (c) Otto's hanging chain net model of the Mannheim Multihalle gridshell; (d) The funicular inner space of Frei Otto's Mannheim Multihalle gridshell, Mannheim, Germany, 1975; (e) Heinz Isler's hanging model for one of his experiments; (f) SICLI concrete shell structure by Heinz Isler, Geneva, Switzerland, 1970 (photo credit: (a) Dan Scorpio; (b) SBA73; (c) Atelier Frei Otto + Partner; (d) Uwe Anspach; (e) Chilton pp. 37; (f) Nicolas Janberg).

Soap films, a well-established physical form finding method popularised by Frei Otto, offer surfaces of minimal potential energy confined within pre-set (closed) boundaries (Otto & Rasch, 1995). These obtained minimal surfaces are characterised by (i) local area minimization, (ii) zero area variation, (iii) equal stresses in all directions, and (iv) zero mean curvature. Due to their fully tensioned geometries, Frei Otto employed soap films to design various membrane (tent) structures, including examples like the 1967 International and Universal Exposition (Figure 2.2a-b), Dance Pavilion at the Federal Garden Exhibition (Figure 2.2c-d), and Diplomatic Club (Figure 2.2e-f).



**Figure 2.2:** (a) Soap film model of the chalice-shaped column for the 1967 International and Universal Exposition or Expo 67; (b) the German pavilion at Expo 67, Montreal, Canada, 1967; (c) a hypar shaped soap film prototype; (d) Dance Pavilion at the Federal Garden Exhibition, Cologne, Germany, 1957; (e) an anti-symmetric conic membrane structure modelled using soap films; (f) Diplomatic Club, Riyadh, Saudi Arabia, 1980 (photo credit: (a) Atelier Frei Otto Warmbronn; ETH Zürich; (b) Frei Otto; (c) saai; (d) Atelier Frei Otto Warmbronn; (e) Frei Otto; (f) Ali Al Mubarak)

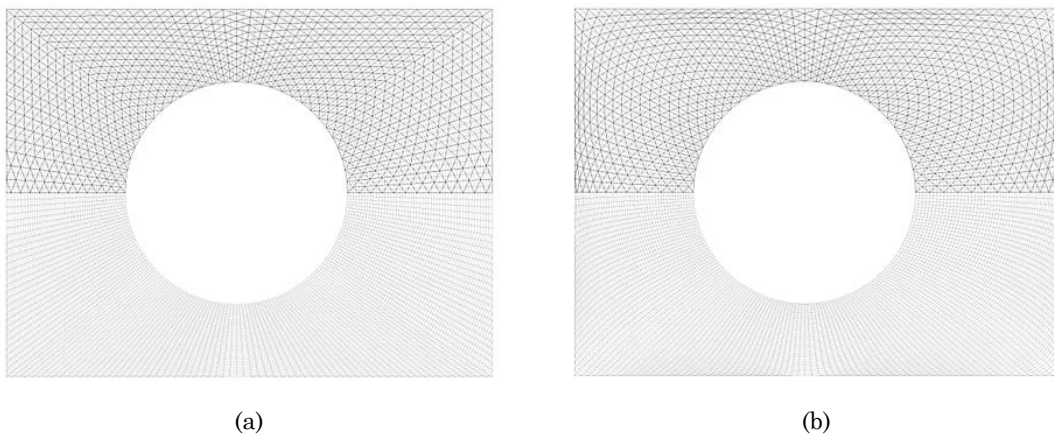
Despite obtaining only fully tensioned geometries from soap films, Sergio Musmeci employed this method in the early design stages of the Basento Bridge (Figure 2.3) to identify a form that could be subsequently adapted and reinforced with concrete (Ingold & Rinke, 2015). Soap films allowed Musmeci to study the structure's pure tension behaviour, revealing shapes that could efficiently distribute forces along specific paths. The form finding process using soap films provided valuable insights into force distribution within the bridge, assisting in the development of a preliminary shape later reinforced with steel and concrete to address areas of tension weakness.



**Figure 2.3** : (a) soap film model for the Basento bridge; (b) Basento bridge by Sergio Musmeci, Potenza, Italy, 1976 (photo credit: (a) Fenu, et al, 2020; (b) Carlo Atzeni).

### 2.1.2 Computational form finding

The dynamic relaxation method (Happold & Liddell, 1975) is used to find the shape of grid, net, and membrane structures, by letting the structure relax to an equilibrium situation (Figure 2.4a-b). The structure is modelled as a system of nodes, which are connected by members. The stiffness of each node depends on the strain of each member. Dynamic relaxation has an iterative, converging process where in the end an equilibrium should be reached. On one hand, the velocity of displacements converges to zero and the stiffness of the structure increases. An advantage of this method over matrix methods is that this method does not have to solve matrices, which decreases the calculation time. Another benefit is the ability to deal with local instabilities, like wrinkling of a membrane. The dynamic relaxation method has been used for the form finding of the gridshell glass roof of the Great Court of the British Museum by Foster + Partners (Figure 2.4c-d).



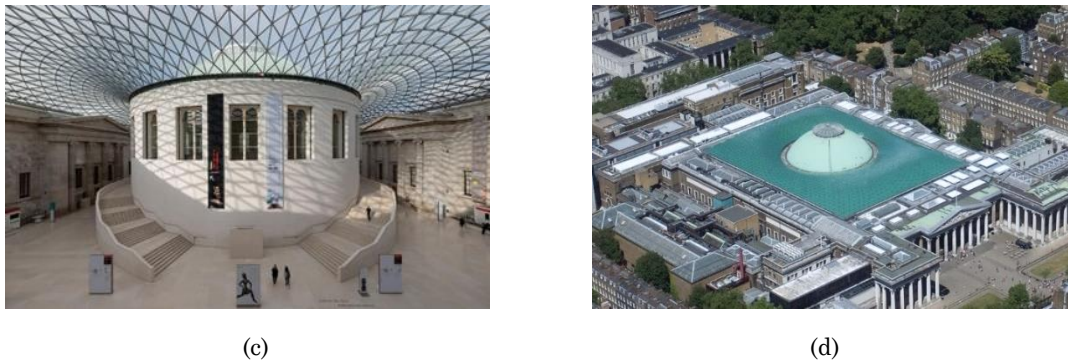


**Figure 2.4:** Design to final roof structure of the Great Court: (a) starting grid; (b) relaxed grid; (c) inner space of the Great Court by Foster + Partners, London, United Kingdom, 2000; (d) Top view the gridshell roof of the British Museum (photo credit: (a-b) C. J. K. Williams, 2016; (c) British Museum; (d) Waagner Biro steel and glass GmbH).

The force density method (Linkwitz & Schek, 1971) employs an analytic technique to linearise the form finding equation for a tension net. This method involves specifying force density ratios (cable force divided by cable length) for each element, resulting in different equilibrium shapes. Higher force densities correspond to shorter elements for a given force, and when the force densities are equal and evenly distributed around a node, a minimal surface (i.e., equilibrium shape) is generated. The method is independent of the initial node locations, numerically robust, and allows for easy attainment of the equilibrium shape. Additionally, the linearization makes the method independent of the material properties of the membrane. The force density method was initially used by Frei Otto in the design of the cable net roof for the Olympic Stadium in Munich, Germany (Figure 2.5a), and also for the cable net roof of the Aviary at the Munich Zoo (Figure 2.5b).



**Figure 2.5 :** (a) Munich Olympic Stadium by Frei Otto, Munich, Germany, 1972; (b) Munich Zoo Aviary by Frei Otto, Munich, Germany, 1980 (photo credit: (a-b) Atelier Frei Otto Warmbronn).

Particle-spring systems (Ochsendorf & Kilian, 2005) consist of lumped masses, called particles, which are connected by linear elastic springs. Each of the massless springs is assigned a constant axial stiffness, an initial length, and a damping coefficient. Springs generate a force when displaced from their rest length. Each particle in the system has a position, a velocity, and a variable mass, as well as a summarised vector for all the forces acting on it. The gravitational pull on a particle causes it to displace and subsequently stretch the springs it is attached to. The particle continues displacing until the sum of the spring forces matches the downward force of the particles. This occurs to every particle until eventually the entire system reaches a state of equilibrium. The particle-spring form finding method was implemented in the design of a cantilevering concrete shell canopy in Mexico City (Figure 2.6).



**Figure 2.6** : Cantilevering concrete shell canopy, Mexico City, Mexico, 2011 (photo credit: (Adriaenssens et al., 2014))

## 2.2 Numerical and analytical methods

### 2.2.1 Finite element method

The finite element method (FEM) is a numerical technique for solving problems which are described by partial differential equations (Nikishkov, 2004). In the field of structural engineering finite element analyses (FEA) are performed to gain understanding on the stress, strain and deflection behaviour of a certain structure or structural element. The finite element solution procedure is made up of the following steps (Nikishkov, 2004):

1. Discretise the solution region
2. Select the interpolation functions
3. Establish the matrix equations
4. Assemble the element equations
5. Solve the global equation system

The FEA process is often performed after the form finding procedure (Nguyen et al., 2020). The input parameters are the material properties, the permanent loads and variable loads. As a form finding tool, FEM is often used to determine the final geometry of the membrane structures, after the pretension forces and loads are applied. The F.A.B Shell

(Fabric – Arch – Base Shell) (Walia et al., n.d.) is an example of the implementation of FEA to determine the final shape of the structure (Figure 2.7). The authors first obtained the shape of the membrane formwork using the dynamic relaxation method. Next, a FEA was performed taking into account the material properties and loads induced by the self-weight of the membrane and the casted concrete layer. The deformed shape is the final shape of the structure.

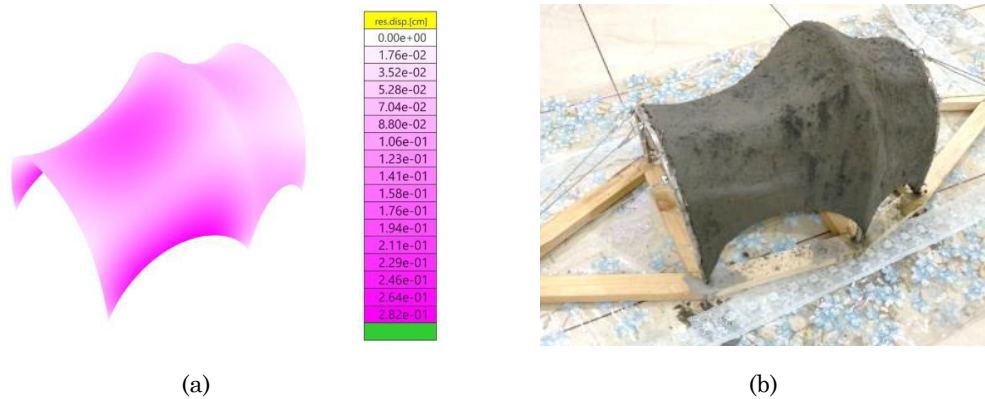


**Figure 2.7:** F.A.B. Shell project of ENPC: (a) finite element displacement results (b) small scale prototype (Walia, et al. 2021)

FEM offers powerful tools for structural analysis, but it is not without its drawbacks. Commercial FEA programs can sometimes function as black boxes, providing results without allowing for in-depth result verification or a deeper understanding of structural behaviour. Additionally, in cases involving specific material behaviours or complex structures, engineers may need to resort to writing custom FEA scripts because off-the-shelf software may not adequately model these scenarios with the required mechanical characteristics. These limitations underscore the importance of balancing the convenience of FEA with the need for comprehensive insight into the structural mechanics and ability to define material properties accurately.

### 2.2.2 Semi-analytical method

In the past, structural engineers relied on semi-analytical methods to determine the deformed configurations of structures (Conway, 1946; Levy, 1942; Seide, 1977; Timoshenko & Woinowsky-Krieger, 1985). This involved manually deriving all the necessary equilibrium equations and subsequently employing numerical tools for solutions. However, technological advancements in recent decades have made computational tools the norm, regarding structural analysis. Despite this, semi-analytical approaches are still used to enable engineers to grasp the fundamental mechanics underlying various structural phenomena. FEA software have user interfaces that require users to only provide input



parameters such as dimensions, support type, material properties, and load magnitudes, bypassing the derivation procedures that grant the final results.

However, semi-analytical methods are limited to simple geometries and material properties, whereas FEM allows for the analysis of complex structures with specific material properties.

## 2.3 Formwork systems

The previous section has illustrated how form-finding methods enable the design of lightweight structures. Concrete is a favourable construction material for such form found double-curved structures, like shells, due to its ability to be moulded into any desired shape. However, in practical applications, these structures remain relatively uncommon. This is primarily because it is inefficient to cast such complex shapes using conventional formwork techniques, which are both labour intensive and cause significant material waste, as they are typically single-use processes. Consequently, there is demand for more efficient formwork methods that capitalise on the mouldability of concrete. The following paragraphs will provide an overview of these formwork systems, along with their respective advantages and limitations.

### 2.3.1 Subtractive moulding methods

Commonly used types of formworks for producing curved surfaces are digitally fabricated timber formworks. These formworks can either be CNC-cut timber falsework to guide thin (plywood) plates (i.e., shipbuilding) (Figure 2.8a) or CNC-milled moulds (Figure 2.8b). The first approach is often used in combination with a falsework to cast entire concrete structures, like ZJA's Extended Waalbridge in Nijmegen (Figure 2.9a). The CNC-milled moulds are used to create single concrete elements, like the façade elements of Grimshaw's Elizabeth Line (Figure 2.9b). Both formwork types can produce single and double curved surfaces. To obtain a smooth surface, an additional finishing layer on top of the timber is sometimes necessary. However, this often limits the possibility of reusing the formwork.

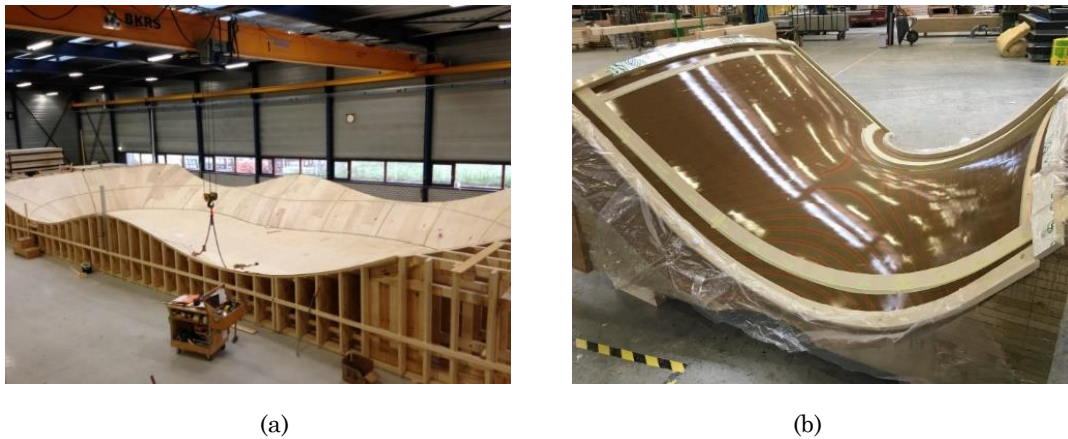


**Figure 2.8:** The two types of digitally fabricated timber formworks executed by Verhoeven: (a) the thin plate formwork and additional falsework for The Extended Waalbridge; (b) mould used to fabricate one of the concrete façade elements of The Elizabeth Line (photo credit: (a) Betoniek; (b) Verhoeven).



**Figure 2.9:** Examples of structures realised using the subtracted formwork method: (a) The Extended Waalbridge by ZJA, Nijmegen, The Netherlands, 2015; (b) The Elizabeth Line by Grimshaw, London, United Kingdom, 2019; (photo credit: (a) Raymond van der Hoogt; (b) Grimshaw).

Other categories of formworks that are used in the building industry are CNC-milled foams. The foams that are mostly used are Expanded Polystyrene (EPS), Extruded Polystyrene (XPS) and Polyurethane (PU). Even though CNC-milling foams has the advantage of producing high precision details, it is also very time-inefficient, as the material removal using milling takes much time. Usually after the CNC-milling is done, the foam is coated with a synthetic resin, like Polyurea. Once the polymer has hardened it is polished to finalise the process. The subtractive nature of CNC-milling of foams and the limited reusability of the moulds, causes this category of formworks to be considerably wasteful.

During CNC-wire cutting, a shape is cut out of a foam block using a hot wire. Subsequently, a mould can be created following the same process as described for the CNC milling method. It's important to note that while wire cutting is effective, it offers relatively less flexibility in shaping compared to milling. For the funicular ribbed concrete floor

prototype (Figure 2.10b) by Block Research Group (BRG) (Ranaudo et al., 2021), CNC wire-cut PU foam blocks were used to form the mould (Figure 2.10a).

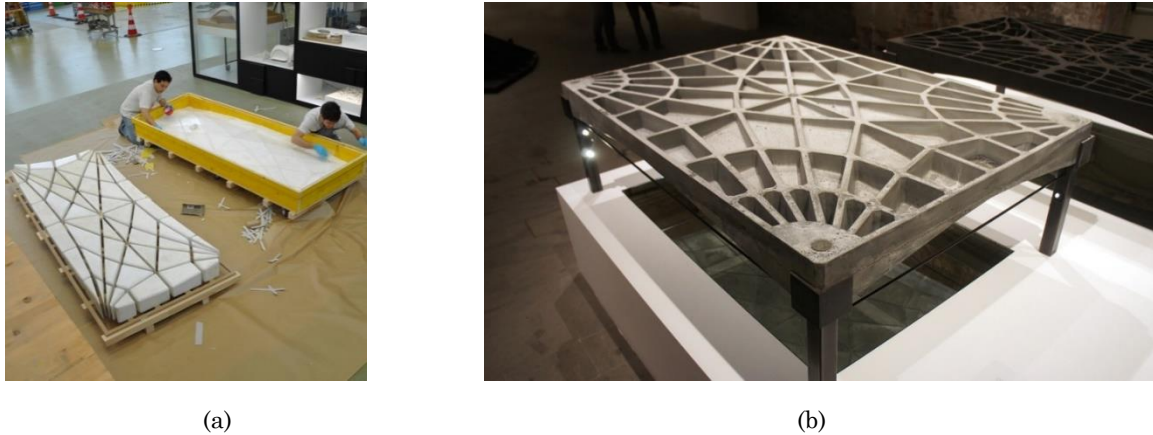


**Figure 2.10:** (a) A formwork system consisting of the CNC wire-cut polyurethane foam inserts (left) and the timber frame (right); (b) the final funicular ribbed concrete floor prototype by BRG, Venice, Italy, 2016; (photo credit: (a) BRG; (b) Nick Krouwel).

### 2.3.2 Adaptable moulds

An alternative approach to constructing form found structures, addressing the waste disadvantage of subtractive methods, involves dividing them into multiple segments to form a modular system. Each segment represents a concrete element created using an adaptive mould (Figure 2.11b). These elements are subsequently assembled on-site to compose the final shell structure. Studies have demonstrated the capability of adaptive moulds to produce double-curved geometries (Grünwald et al., 2015; Raun & Kirkegaard, 2015; Schipper et al., 2015). Commercial applications have also been reported (Adapa, 2022; Hoppermann et al., 2015; Kristensen & Raun, 2011; Vollers & Rietbergen, 2009). The functioning of adaptive moulds follows a step-by-step plan (Figure 2.11a). The mould, made from a flexible material (e.g. silicone), is supported by a subsystem that determines the desired final shape:

1. The mould is then filled with self-compacting concrete (SCC), which can be reinforced using fibres or textile reinforcement.
2. The SCC hardens for a short period of time in the flat position to obtain initial binding and stiffening. This prevents the concrete from flowing during the deformation process.
3. Next, the mould is carefully deformed into its desired final shape.
4. The concrete is then allowed to further harden until it reaches its ultimate strength.
5. Finally the (double-)curved panel is demoulded and the mould can be re-used to create the next panel (Schipper et al., 2015).

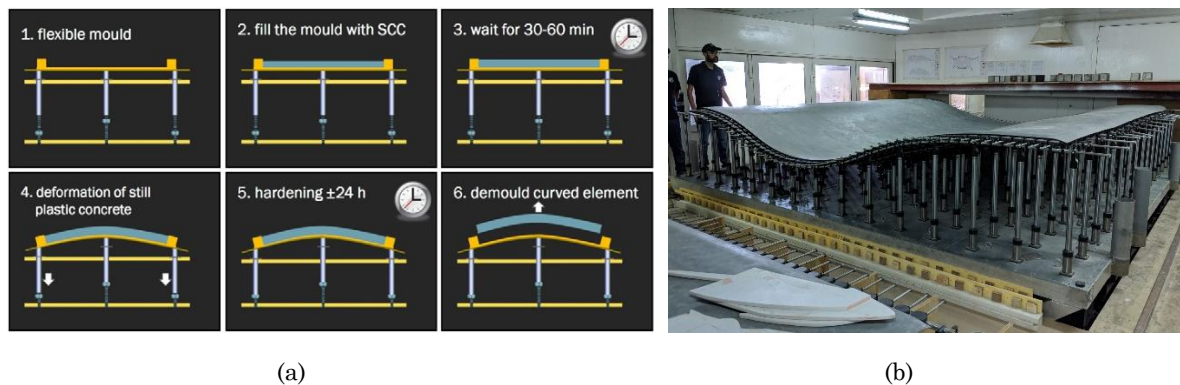


**Figure 2.11:** (a) the manufacturing steps for a curved element using an adaptive mould according to (Schipper et al., 2015): (1) flexible mould in flat state; (2) flexible mould filled with SCC; (3) first hardening stage; (4) gradual deformation towards desired shape; (5) second hardening stage; (6) demoulding of curved element; (b) Adapa D300 adaptive mould (Adapa, 2022)

Adaptive moulds are advantageous with regards to reusability and the ability to produce both synclastic and anticlastic elements. However, the technique is limited in terms of the geometric freedom, as it can only produce panels with limited curvature. Furthermore, the process requires deformation of the concrete during its hardening period. The strains that result from these imposed deformations can negatively affect both the structural strength of the panels, as well as the appearance of the panels, for example because of the presence of wrinkles and/or cracks.

### 2.3.3 Additive manufacturing

Adaptable moulds, alongside subtractive methods are limited to geometries that have no undercuts or inner voids. This is where another fabrication method, that can be used to create free form structures, is introduced: additive manufacturing. The two approaches of additive manufacturing for concrete structures that are mentioned in this paragraph are concrete 3D printing (C3DP) and formwork 3D printing (F3DP).

Various methods are available for concrete 3D printing (C3DP), with extruded concrete 3D printing (EC3DP) being the most widely adopted additive manufacturing technique in the construction industry. During the printing process, cementitious material is extruded in continuous strands, layered upon each other to construct the desired structure. The shape of the filament is determined by the chosen nozzle type, as the material is squeezed through the nozzle at the print head. EC3DP has proven successful in different applications, including its use by the Digital Building Technologies (DBT) research group at ETH Zurich to fabricate specially shaped columns for the Concrete Choreography project (Anton et al., 2021) (Figure 2.12a, Figure 2.12a). Additionally, the OBAYASHI Corporation employed this method to manufacture a shell-shaped bench (Figure 2.12b, Figure 2.12b).



**Figure 2.12:** Extruded concrete 3D printing for different implementations: (a) tailor-shaped columns; (b) cantilevering shell structure (photo credit: (a) Axel Crettenand; (b) (Sakagami et al., 2020)).

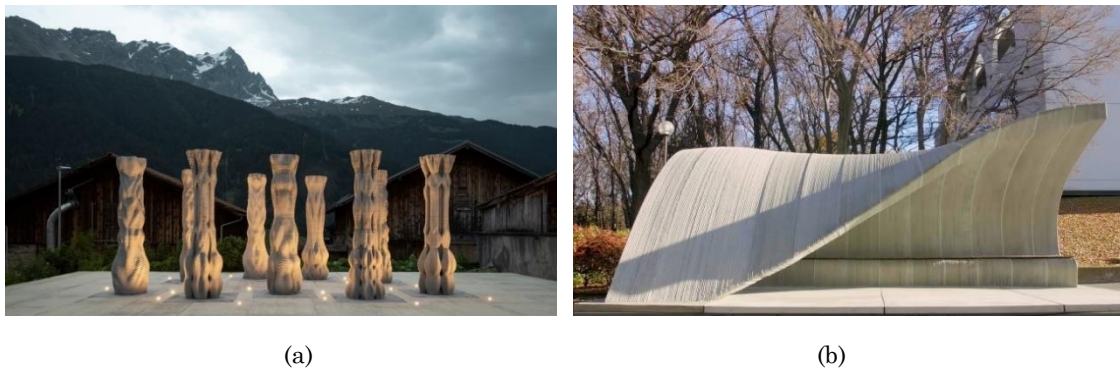


**Figure 2.13:** Examples of structures realised using the extruded concrete 3D printing method: (a) Concrete Choreography by DBT, Graubünden, Switzerland, 2019.; (b) the Shell-shaped bench by OBAYASHI Corporation, Japan, 2020 (photo credit: (a) Benjamin Hofer; (b) OBAYASHI Corporation).

One limitation of extruded concrete 3D printing (EC3DP) is the presence of delays between each layer of extruded concrete, leading to "cold joints" that exhibit weaker bonds between adjacent layers (Hack & Kloft, 2020). In contrast, shotcrete 3D printing (SC3DP) involves the pressurised spraying of concrete to create the 3D structure (Figure 2.15a). The dispersed stream of concrete during spraying (Figure 2.14a) promotes mechanical layer intermixing, resulting in enhanced layer bonding compared to EC3DP (Kloft et al., 2020). This method has been successfully employed to fabricate a double-curved wall (Figure 2.14b) at the Digital Building Fabrication Laboratory (DBFL) of TU Braunschweig (Kloft et al., 2019).

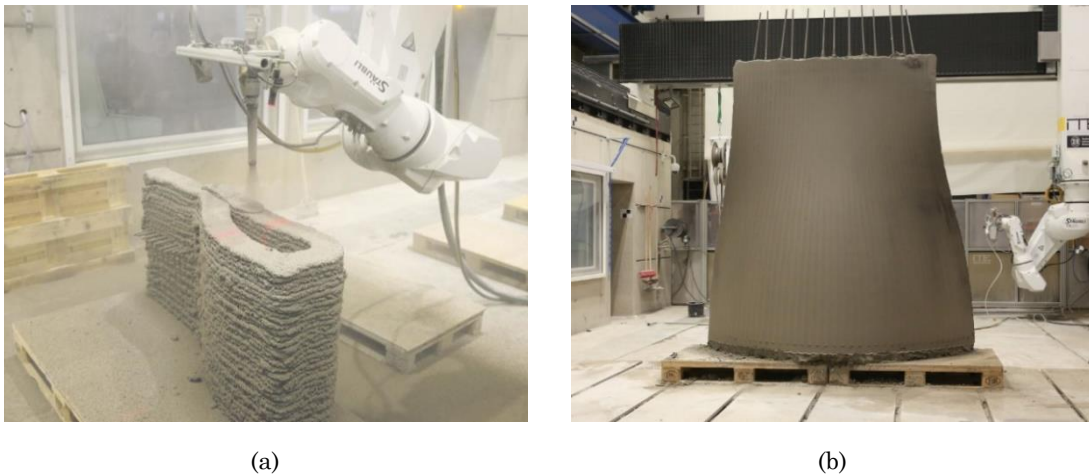


**Figure 2.14:** (a) Shotcrete 3D printing in the Digital Building Fabrication Laboratory at TU Braunschweig; (b) Double curved wall fabricated in the Digital Building Fabrication Laboratory at TU Braunschweig (photo credit: (a-b) ITE, TU Braunschweig).

When employed for fabricating moulds, F3DP encompasses three distinct methods (Figure 2.15):

1. Material extrusion: a liquid or paste, such as polymers, clay, or concrete, is extruded through a nozzle following a predetermined printing path.
2. Material jetting: drops of feedstock material, including foam or wax, are sprayed onto a substrate from a distance using one or more nozzles.
3. Binder jetting: a liquid binder is selectively applied to successive thin layers of powder (Jipa & Dillenburger, 2022).

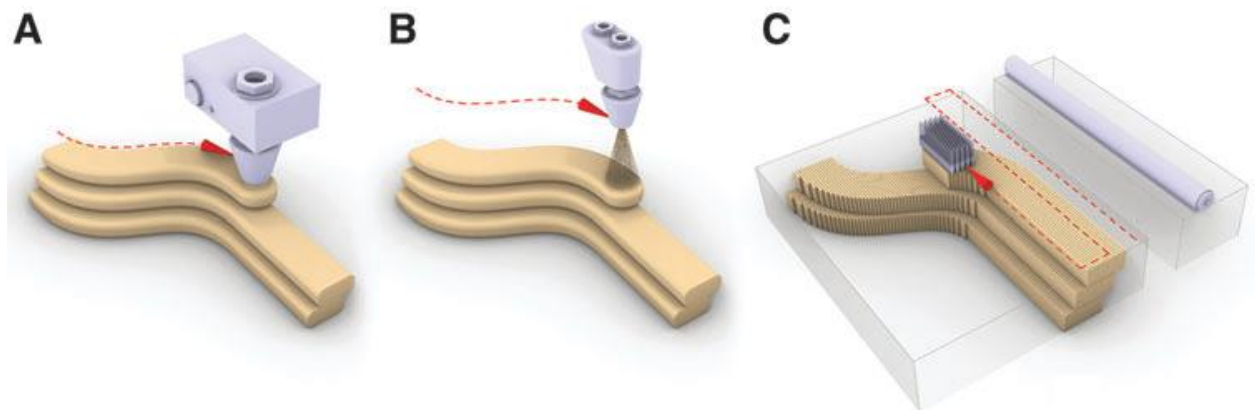


**Figure 2.15:** Three approaches for formwork 3D printing (F3DP): (a) material extrusion with polymers, clay, or concrete; (b) material jetting with foam or wax; (c) binder jetting (DBT, 2023)

All three methods have demonstrated successful applications. Notable projects utilizing material extrusion 3D printing include the Eggshell project by the Gramazio Kohler research group at ETH Zurich (Burger et al., 2020) (Figure 2.16a) and Cocoon, the 3D Printed clay formwork developed at the University of Michigan (Bruce et al., 2021) (Figure 2.16b). As for material jet 3D printing, a noteworthy project is the FreeFAB wax mould (FreeFAB, 2023) (Figure 2.17), facilitating recycling of the formwork material through remelting. The Smart Slab floor for the DFAB House (Aghaei Meibodi et al., 2018) (Figure 2.18) showcases the benefits of binder jet 3D printing, including geometric freedom, and the ability to produce large volumes with high precision.



**Figure 2.16:** Examples of structures realised using the material extrusion 3D printing method: (a) complex shaped concrete element by Gramazio Kohler research group, Zurich, Switzerland, 2020; (b) complex shaped concrete element upon demoulding (photo credit: (a) Gramazio Kohler research group; (b) (Bruce et al., 2021))



**Figure 2.17:** FreeFab wax moulds produced by material jetting 3D printing (FreeFAB, 2023).

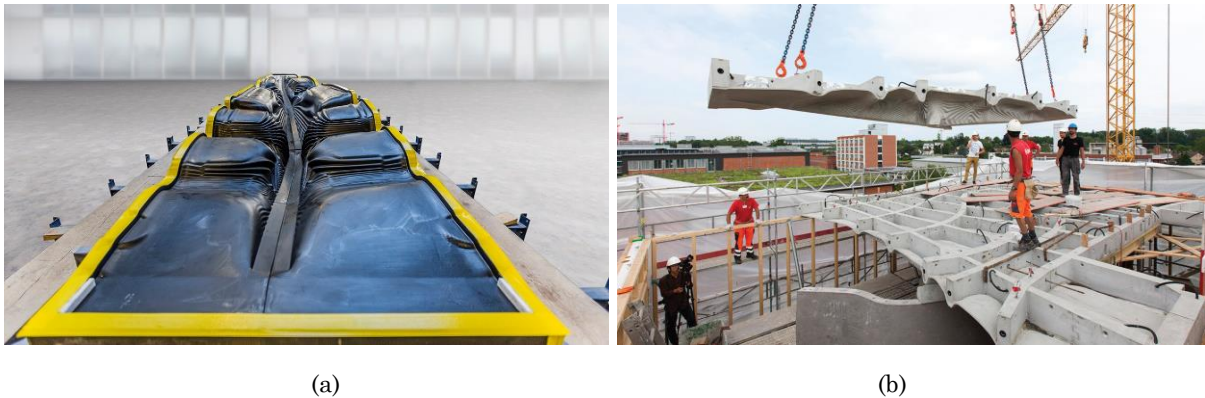


**Figure 2.18:** (a) section of the binder jet 3D printed mould for the Smart Slab; (b) assembly of precast slab sections at the construction site of the DFAB House (photo credit: (a) EMPA; (b) Tom Mundy).

### 2.3.4 Fabric formworks

Fabric formworks have been used in geotechnical and offshore engineering since the early 1900s (West, 2017). However, it was not until the 1960s that the new availability of high strength, low-cost fabrics stimulated the widespread use of these types of formworks (Lamberton, 1989). Flexible formworks have shown their potential to significantly increase the efficiency of the fabrication of doubly curved concrete structures by reducing manual labour and material waste (Lee et al., 2020). The use of fabric formworks allows to cast architecturally interesting, optimised structures that use up to 40% less concrete than an equivalent strength prismatic section (Orr et al., 2011).

Initial interest in the architectural possibilities of fabric formworks can be attributed to the Spanish architect Miguel Fisac, whose work in this field culminated in a patented method for the construction of prefabricated fabric formed wall panels (Figure 2.19) (Orr, 2010). Professor Mark West, based at the University of Manitoba's Centre for Architectural Structures and Technology (C.A.S.T), has conducted additional and ongoing research. This research explores the architectural potential of fabric formworks, not only for shells, panels, columns, and walls, but also for beams and trusses (Figure 2.20).





**Figure 2.19:** (a) Ybarra Hotel Tres Islas by Miguel Fisac, Las Palmas, Spain, 1972; (b) Facade detail of Iglesia de Nuestra Señora Flor del Carmelo (Our Lady Flower of Carmelite Parish) by Miguel Fisac, Madrid, 1983. (photo credit: Fundación Miguel Fisac)



**Figure 2.20:** (a) Prototype mould, with a coated polyethylene fabric; (b) Prototype fabric-formed concrete truss fabricated at C.A.S.T. (photo credit: Mark West)

The NEST HiLo roof structure (Figure 2.21b), built at EMPA in Dübendorf, Switzerland, presents a successful application of flexible formworks for large-scale vaulted concrete shells, combining a cable-net falsework with a woven textile shuttering (Figure 2.21a) (Veenendaal, 2017).

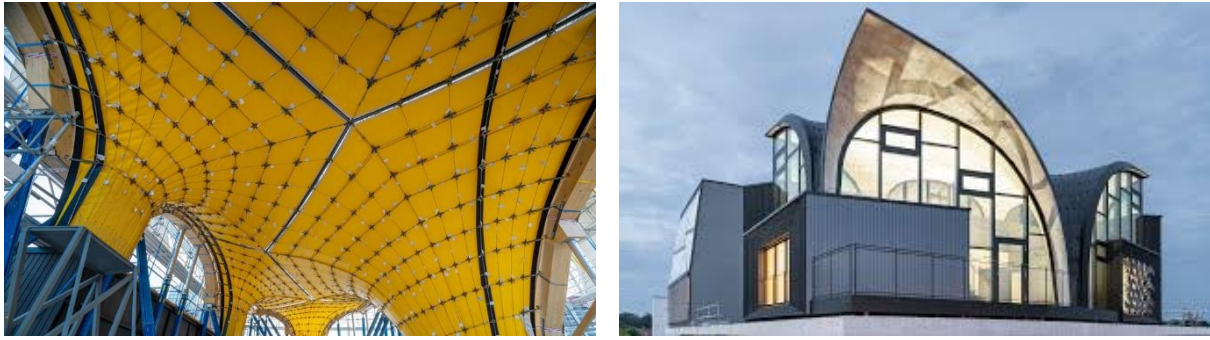


**Figure 2.21:** (a) cable-net falsework and woven textile shuttering of the NEST HiLo roof prototype; (b) final roof structure of NEST HiLo at EMPA in Dübendorf, Switzerland (photo credit: (a) Juney Lee; (b) EMPA)

Flexible formworks that use woven textiles can only produce doubly curved surfaces that are developable. The fabrication of more complex doubly curved surfaces requires generating cutting patterns, leading to the production of multiple patches that need to be assembled by stitching or sewing. The KnitCrete technology (Popescu, 2019) eliminates this problem by using weft-knitted textiles. These textiles present several advantages over conventionally woven fabrics in realizing complex geometries. They enable the creation of curved spatial surfaces with minimal to no additional effort by adjusting the length and width of the textile locally during the fabrication process. Furthermore, KnitCrete allows for custom placement of material and surface texturing, which helps control the performance of the formwork during the construction. A computational pipeline is used to transform the designed 3D geometry into a printing pattern. This printing pattern can then be shared with CNC knitting machines available anywhere around the world. The final product is a lightweight knitted textile that can be easily compacted and transported to the construction site (Popescu, 2019). At the construction site the textile is tensioned to obtain its desired shape (Figure 2.22a). Next, a thin layer of a special adhesive or cement-paste is sprayed on top of the fabric to stiffen it and make it the basis of the concrete structure (Figure 2.22b) (Popescu et al., 2021). Lastly, the structural concrete is applied manually to finish the structure (Figure 2.22c) (Popescu et al., 2021). The KnitCandela pavilion (Figure 2.22d), a collaborative project between the Block Research Group and Zaha Hadid Architects, was the first large-scale application of this novel formwork method. The concrete shell measures 5.8 x 5.8 x 4.1 m, with an area of approximately 50 m<sup>2</sup> (Popescu et al., 2021).

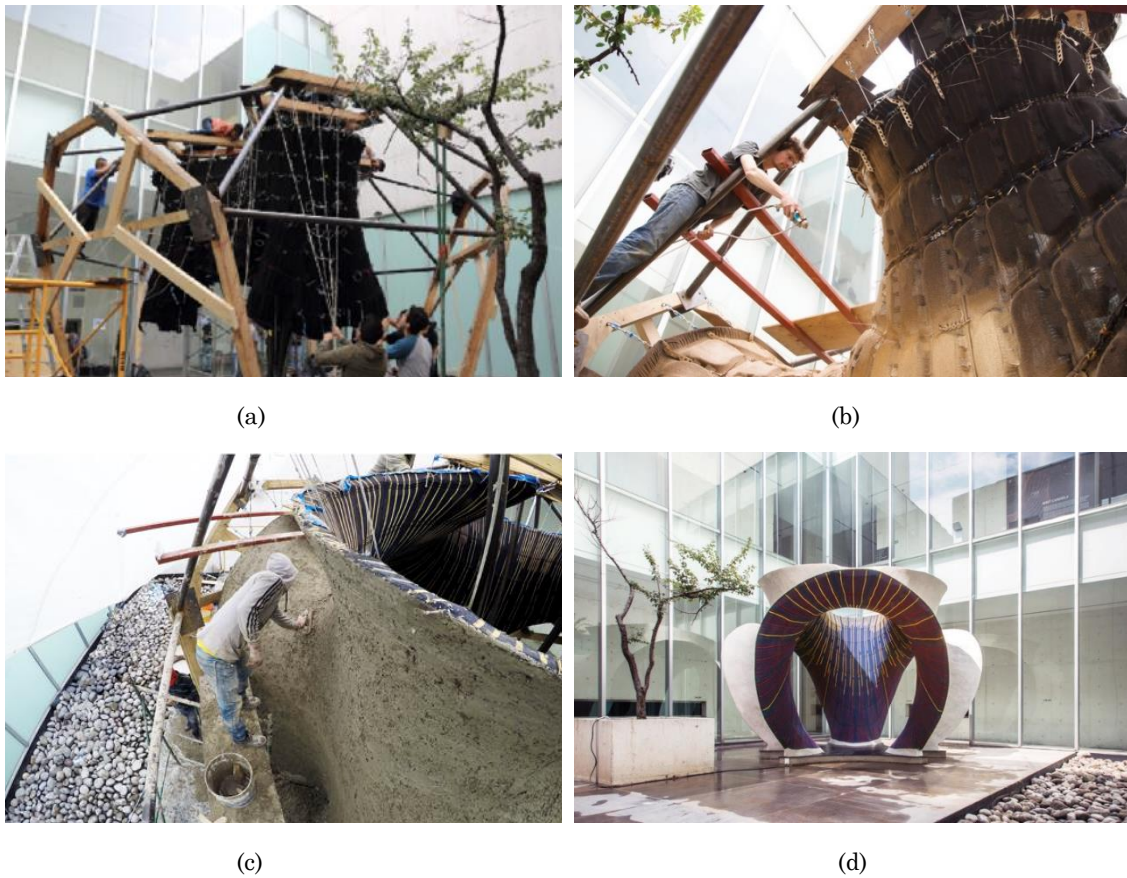


**Figure 2.22:** (a) Tensioning of the textile; (b) Freezing of the textile using high strength cement paste; (c) Applying the structural concrete; (d) Resulting shell structure (KnitCandela). (photo credit: (a)-(c) Mariana Popescu; (d) Juan Pable Allegre)

## 2.4. Summary

This chapter introduced a spectrum of physical and numerical form finding methods enabling the structural design of lightweight concrete structures. Alternatively, it showed how numerical and semi-analytical methods can be used to determine final deformed geometries of designs. Despite the availability of these tools, it's noteworthy that in practice, the preference for monolithic structural elements remains due to their cost-efficient construction. Transitioning from theories to practical applications, the chapter further navigates through various formwork systems designed to facilitate the fabrication of such bespoke concrete structure. Amid these systems, weft-knitted formwork systems emerge as unique contenders, distinguished by their lightweight attributes and ability to be assembled into intricate shapes without necessitating the support of falsework.



The background of the entire page is a close-up, textured blue mesh fabric. The mesh consists of a regular grid of small, diamond-shaped openings, with the threads appearing as a vibrant blue color. The lighting is even, highlighting the three-dimensional quality of the woven material.

**Part II:  
Approach**



## 3. Methodology

The primary aim of this research is to establish a method for modelling the deformation behaviour of uncoated knitted formwork under concrete pressure, to find the final funicular shape of the formed structure. This chapter gives an overview of the methodology, and the relevance of the different research approaches that are used.

### 3.1 Overview

Figure 3.1 presents an overview of the proposed methodology. The first stage of the research approach consists of material characterisation of the various cementitious mixtures (Figure 3.1a) and knitting patterns (Figure 3.1b) that are studied in this thesis. The findings from the consistency and strength tests of the mortars and biaxial tests of the textiles are used as input parameters for the subsequent membrane modelling stage (Figure 3.1c). This process consists of establishing the boundary conditions (BC) of the modelled knitted textiles and quantifying the loads caused by the concrete pressure. Next, the equilibrium equations are derived and solved using (semi-)analytical methods. The resulting deflection models are then used as starting points for the prototyping part of the research (Figure 3.1d). For this part of the research a forming system is established and used to fabricate the physical prototypes. Finally, the geometry of the prototypes are compared with the models to validate their accuracy.

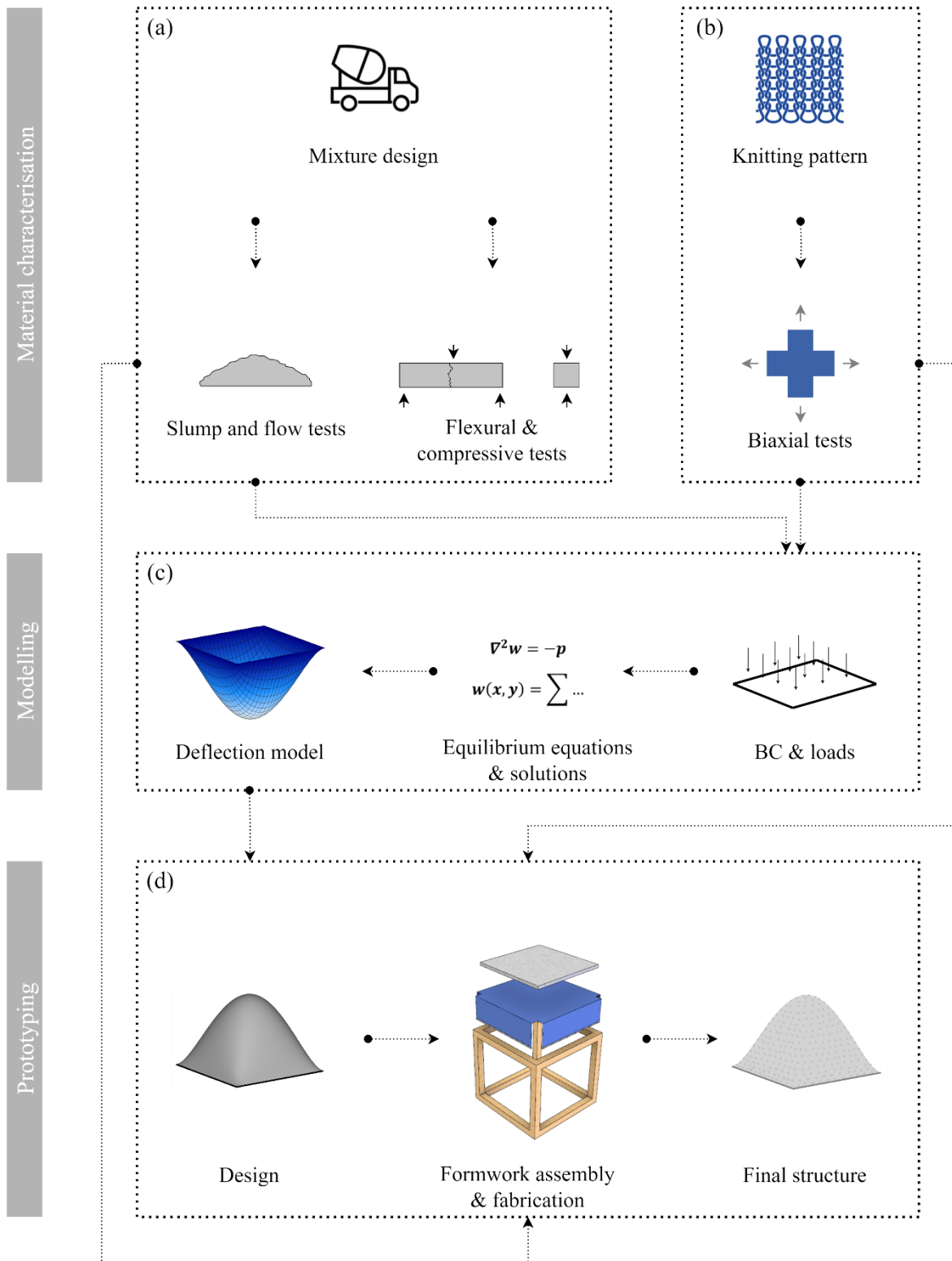


**Figure 3.1:** Methodology overview: (a) material characterization of cementitious mixtures; (b) material characterization of knit architectures; (c) membrane modelling process; (d) prototyping.



## 3.2 Material characterisation

Accurately modelling the deflection behaviour of the knitted flexible formwork necessitates a comprehensive understanding of the mechanical properties of the used knitted textile. The procedure involves the fabrication of multiple cruciform samples, which are subsequently subjected to biaxial testing using a makeshift testing machine. The resulting data is analysed and used to calculate key mechanical properties. By undertaking this systematic approach, valuable insights into the deformation characteristics and structural performance of the knitted textile can be gained, thereby facilitating the accurate modelling of its deflection behaviour in the context of flexible formwork applications. In Chapter 4, a comprehensive explanation of the knit design considerations and ensuing mechanical tests is provided.

The structural design approach developed during this research exploits the flexibility of the knitted formwork to create doubly curved geometries. The assessment of the fabrication potential of this flexible formwork system necessitates the development of a mortar that can effectively retain its shape during the physical form-finding process. In achieving a balance between low flowability and a certain degree of workability, the proportioning of the cementitious mixture plays a crucial role. These material requirements are essential to facilitate the construction process. Ensuring low flowability is imperative to maintain a consistent cross-section thickness when working on steep surfaces. Conversely, a sufficient degree of workability is necessary for ease of application of the cementitious material and decent self-compacting. Furthermore, understanding the mechanical strength of the mortar is crucial for evaluating the structural potential of this system. The methodology entails (i) creating multiple mixture designs, (ii) assessing their workability, (iii) fabricating samples, (iv) conducting comprehensive testing on these samples, and subsequently (v) analysing the resulting data. Through these systematic investigations, a deeper understanding of the material properties and performance characteristics of the mortar within the knitted flexible formwork system can be attained. A detailed explanation of the mixture design considerations and subsequent mechanical tests are provided in Chapter 4.

## 3.3 Membrane modelling

The desire to employ KnitCrete without the need for coating procedures to stiffen the flexible formwork, demands a modelling strategy that is capable of determining the deflection of the knitted fabric under hydrostatic loads.

The method used for the modelling depends on (i) availability, and (ii) academical motivation. FEM is a powerful tool for structural analysis. It is capable of accurately approximating the deformation behaviour of a structure. It is especially useful for complex shaped structures, where the stress distribution is not straight forward, or structures made up of materials with particular mechanical properties. However, FEM is not without its drawbacks. Commercial FEA programs can sometimes function as black boxes, providing

results without allowing for in-depth result verification or a deeper understanding of structural behaviour. Additionally, in cases involving specific material behaviours or complex structures, engineers may need to resort to writing custom FEA scripts because off-the-shelf software may not adequately model these accurately.

The lack of commercially available FEA programs capable of accurately modelling the intricate material behaviour of knitted textiles, coupled with the desire to establish a profound comprehension of the mechanics behind membrane deflections, has led to the selection of the semi-analytical approach as the preferred method. While the semi-analytical approach is limited to simple geometries and material properties, it involves manually deriving all the necessary equilibrium equations and subsequently proving strategies to solve them. A comprehensive theoretical explanation of this modelling approach is presented in Chapter 5.

### 3.4 Prototyping

Upon establishing the deflection models, they need to be validated. This is done by fabricating physical prototypes, with different geometries. The structural geometries of interest are one with a square shaped boundary and one with different dimensions in x-, and y-direction (i.e. rectangular). The geometries of these structures are then measured and compared with resulting geometries of the membrane models.

Before these prototypes can be constructed, a forming system needs to be established. The system relies on a prefabricated weft-knitted textile that serves as the basis for constructing the funicular element through tensioning and casting procedures. The weft-knitted textile is manufactured in an automated manner using existing industrial CNC flat-bed knitting machines. To fabricate the appropriate textile, the given 3D geometry must be translated into a 2D knitting pattern. This pattern is represented as a pixel-based diagram that outlines the machine's actions during the fabrication process. The computational approach for generating these patterns is beyond the scope of this thesis.

An inherent necessity to invert the concrete elements formed using this flexible formwork system to work effectively under compression presents challenges when attempting to cast these elements on-site. To invert them on-site, causes significant hindrance and requires extra attention on additional (point) loads during the structural design process. As a result, this thesis explores a prefabrication strategy where these elements are manufactured off-site and later transported to the construction site for assembly. Additional information regarding the formwork system, the prefabrication process, and geometric comparisons can be found in Chapter 6.

## 4. Material characterisation

This chapter is dedicated to investigating the mechanical properties of the weft-knitted textiles and consistency and strength properties of the mortars used in this research project. A comprehensive exploration of the design, testing, and data analysis of these materials will be presented. Multiple knitting patterns and mortar mixtures were examined to understand their material properties. Based on the findings, the optimal knitting architecture and mortar design were selected for further investigation in the subsequent phases of the research.

### 4.1 Knit properties

#### 4.1.1 Knit design and sample preparation

To accurately model the deflection behaviour of a knitted flexible formwork subjected to concrete (or mortar) induced hydrostatic loading, it is necessary to determine the Young's moduli and Poisson's ratios of the knitted textile through biaxial testing. In this research, three distinct knitting patterns, namely interlock, hexagonal, and tuck, are selected for investigation. The choice of these particular knitting architectures is made based on their anticipated characteristics of elasticity, strength, and permeability.

Following the guidelines outlined in the Japanese Standard MSAJ/M-02-1995, cruciform-shaped test specimens are employed to enable the simultaneous application of forces in both the x- and y-directions. This shape ensures that the samples can undergo deformation and strain in multiple directions, replicating real-world loading conditions. For each knitting pattern, three cruciform samples are fabricated to provide a statistically significant sample size for testing.

In the case of woven textiles, it is customary to cut the samples into cruciform shapes for testing purposes; however, for knitted textiles, this leads to the undesired unravelling of the fabric. To overcome this limitation, the test specimens are directly knitted into a cruciform shape, eliminating the need for cutting. To fabricate these bespoke cruciform samples a Steiger Vega 3.130 CNC flat-bed knitting machine was used. An iterative sample production approach ensured that the samples meet the specified dimensions, of approximately 300 mm x 280 mm, and fit in the testing apparatus. Each knitting pattern requires its own specific pattern generation due to their inherent geometrical differences. An elastic overlock stitch is applied along the edges of the samples to protect against unravelling. Typically, the arms of a cruciform test specimen are slit to achieve a defined and known stress level at the measurement field in the centre of the cruciform. This stress level is expected to closely match the stress in the arms, which can be calculated based on the

force measured near the actuators. However, due to the unravelling effect on the uncoated knitted fabric, it is not possible to introduce slits. Consequently, a correction of the recorded membrane stress is necessary. It is important to note that the stress correction is not included in the scope of the present work. Hence, the material properties provided below should be regarded as a preliminary approximation.

To secure the samples in the biaxial testing setup, channels are incorporated in the generated knitting pattern. These channels enable rods to pass through, as depicted in Figure 4.1, and hold the samples firmly in place during testing, ensuring accurate and consistent results.

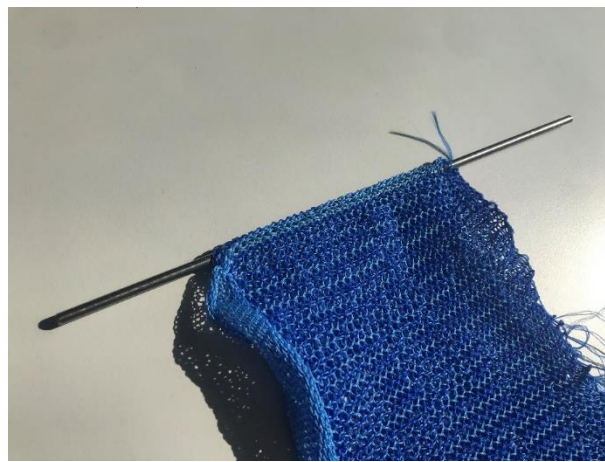


**Figure 4.1:** Cruciform arm with a rod inserted through the channel.

Considering the stresses, strains, and exposure to moisture during the casting process, high-performance polyester (PES) yarns are chosen as suitable candidates for the fabrics. High tenacity polyester yarns, characterised by low moisture absorption, average elasticity, and exceptional resistance (Tamke et al., 2015), offer desirable properties for withstanding the conditions during casting. Each yarn guide of the knitting machine accommodates four yarns, allowing for multiple yarns to be simultaneously incorporated into the knitting process. This feature enables the fabrication of samples with specific densities. The final cruciform samples are illustrated in Figure 4.2.

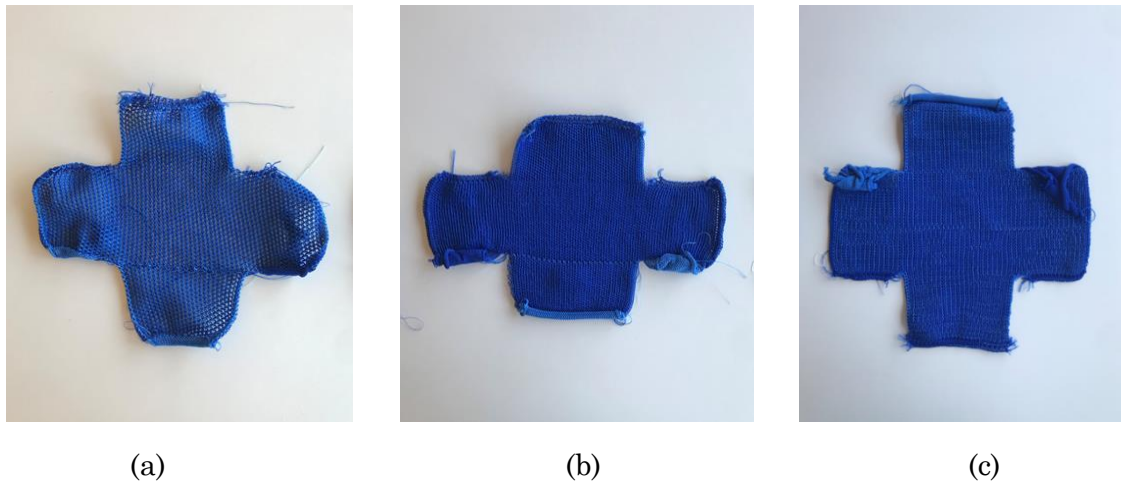


**Figure 4.2:** The final cruciform samples: (a) hexagonal; (b) tuck; (c) interlock.

#### 4.1.2 Biaxial test configuration

The biaxial tests are conducted using a makeshift biaxial test machine (Figure 4.3). Equipped with a load cell (LC) in each loading direction to measure the tensile forces applied by the hydraulic pump in both weft and warp directions. This set-up allows for simultaneous loading and measuring of the forces in the two directions. Additionally, two potential (POT) meters are fixed to the fabric, perpendicular to each other, allowing the measurement of the elongation of the textile in both weft and warp directions.

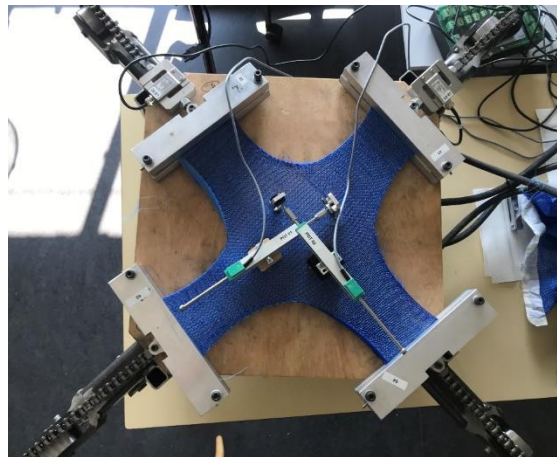


**Figure 4.3:** The biaxial test machine setup

The use of a hydraulic pump system in the biaxial test setup results in discontinuous loading, which may introduce jumps in the obtained results. To mitigate the impact of these disturbances, data cleaning procedures are employed to ensure the reliability and

accuracy of the measurements. Cleaning the data involved filtering out irregularities and inconsistencies caused by the discontinuous loading.

A total of nine biaxial tests are conducted, comprising three tests for each of the three knitting patterns (i.e., interlock, hexagonal, and tuck). Figure 4.4 provides the dimensions of the individual cruciform specimens used in these tests, as well as the initial distances between the POT meter pins before the textiles are subjected to loading.

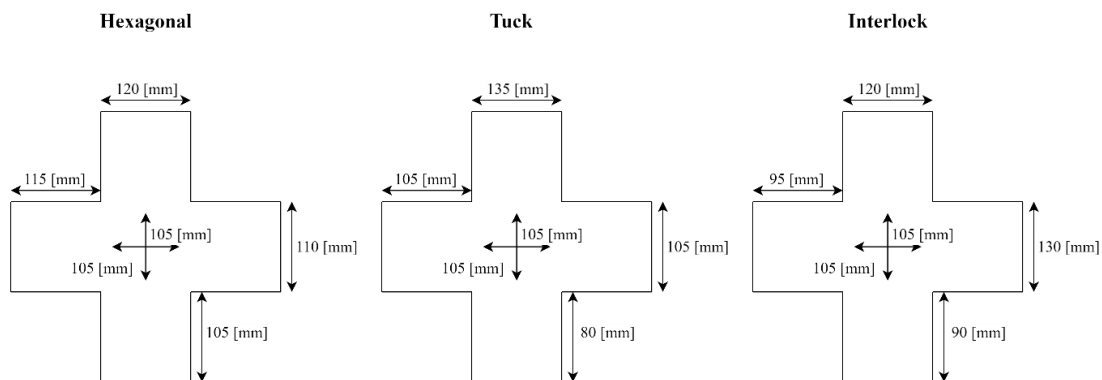


**Figure 4.4:** Plan views the dimensions of the hexagonal, tuck and interlock samples.

Currently no testing procedure exists for the biaxial testing of knitted fabrics, which is hence performed according to the testing procedure of the Japanese Standard MSAJ/M-02-1995 for biaxial testing of woven fabrics. Herewith, the unknown elastic mechanical properties of the material can be determined. The main characteristic of MSAJ/M-02-1995 is that five different predefined warp-to-weft stress ratios (1:1, 2:1, 1:2, 1:0, and 0:1) are consecutively applied on a cross shaped test specimen with the yarns parallel to the arms of the cross. However, the biaxial tensioning set-up used during this research is only capable of performing three warp-to-weft stress ratios: 1:1 (biaxial), 1:0 (uniaxial), and 0:1 (uniaxial). During the loading and unloading procedure, the warp-to-weft load ratio is held constant. Each test procedure results in a stress-strain-diagram. From this complete set of test data six stress-strain-paths can be extracted, one for each yarn direction, for the three load ratios.

### 4.1.3 Derivation of the material properties

The calculation of Young's modulus in knitted textiles involves analysing the stress-strain curves obtained during biaxial tension testing. Weft-knitted textiles display hyperelastic stress-strain curves (Figure 4.5), characterized by two linear elastic regions: region I with lower Young's moduli and region II with higher Young's moduli. By determining the slopes of the stress-strain curves in the linear elastic regions for both the x- and y-directions, the Young's moduli can be calculated using Equations (4.1) and (4.2).

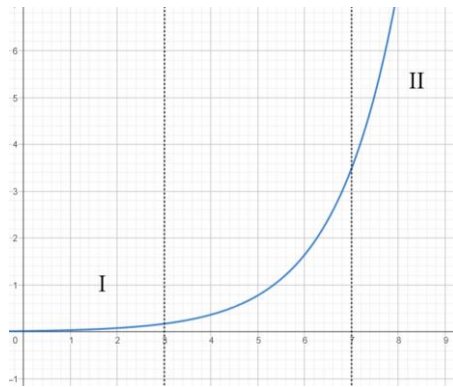


**Figure 4.5:** Example of a hyper-elastic curve with linear regions I and II

$$E_x = \frac{\sigma_x}{\varepsilon_x} \quad (4.1)$$

$$E_y = \frac{\sigma_y}{\varepsilon_y} \quad (4.2)$$

The calculation of Poisson's ratio in a material involves measuring the lateral strain that occurs perpendicular to the applied force. During biaxial tension testing, the lateral strain in the y-direction when a force is applied in the x-direction, and vice versa, is measured. These lateral strains represent the deformation that occurs perpendicular to the primary loading direction. To calculate Poisson's ratios in x-, and y-direction, the measured lateral strain is divided by the axial strain using the formulae:

$$v_x = -\frac{\varepsilon_y}{\varepsilon_x} \quad (4.3)$$

$$v_y = -\frac{\varepsilon_x}{\varepsilon_y} \quad (4.4)$$

These formulae quantify the ratio of transverse contraction to axial elongation, providing insight into how a material responds to applied forces in terms of its lateral and axial deformation behaviour. The calculation of Poisson's ratio is crucial for understanding the material's mechanical properties and can aid in the design and analysis of structures that experience multidirectional loading.

#### 4.1.4 Results and discussion

The test results are presented in two plots for each knitting pattern. The left plot (Figure 4.6a-c) illustrates the stress-strain relationship in both the warp and weft directions under biaxial loading (i.e., load ratio 1:1), while the right plot (Figure 4.6d-f) depicts the stress-strain relationship under uniaxial loading (i.e., load ratios 1:0 and 0:1).

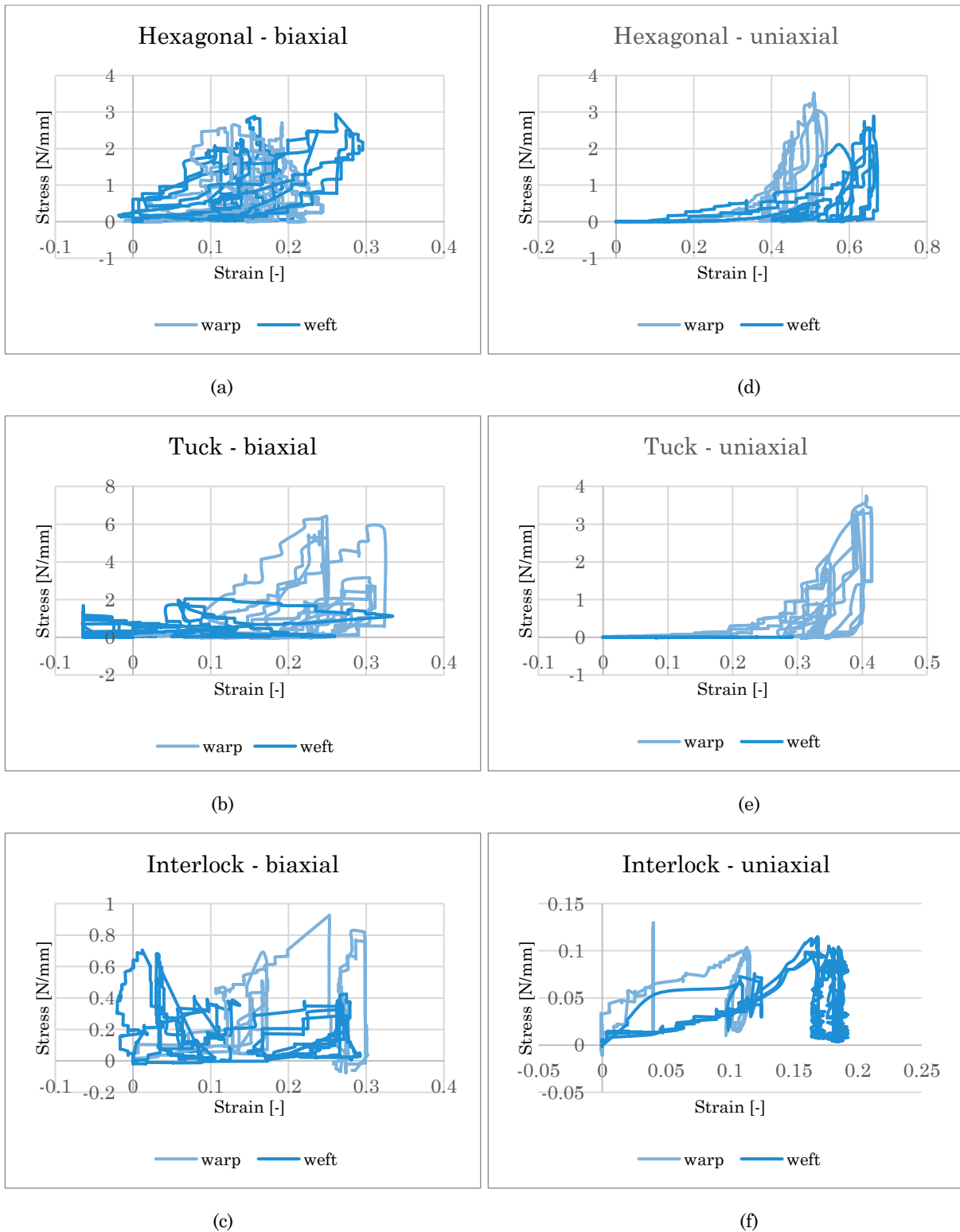
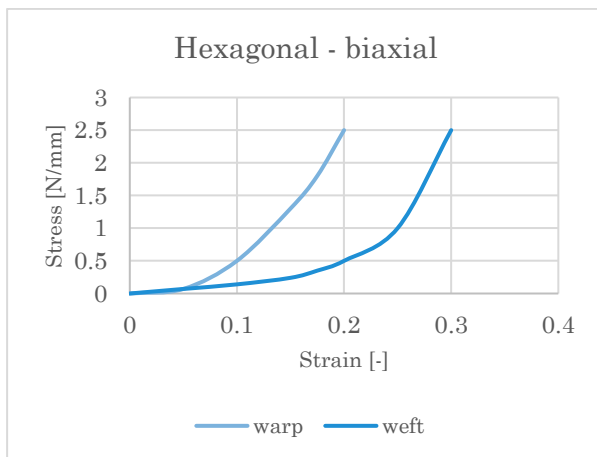


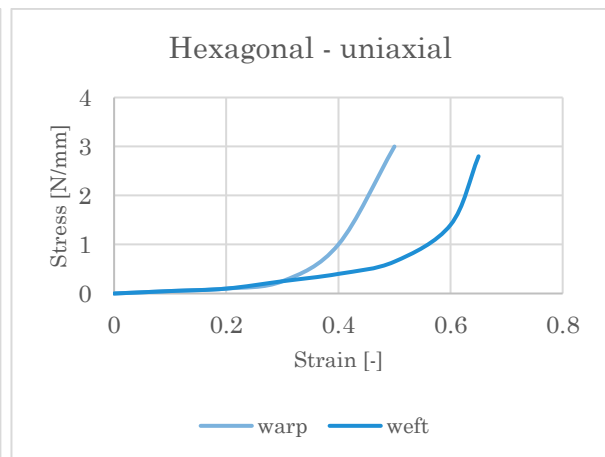
**Figure 4.6:** The raw stress-strain plots for: (a) the hexagonal knit pattern loaded 1:1, (b) the tuck knit pattern loaded 1:1, (c) the interlock knit pattern loaded 1:1, (d) the hexagonal knit pattern loaded 1:0 and 0:1, (e) the tuck knit pattern loaded 1:0 and 0:1, (f) the interlock knit pattern loaded 1:0 and 0:1,



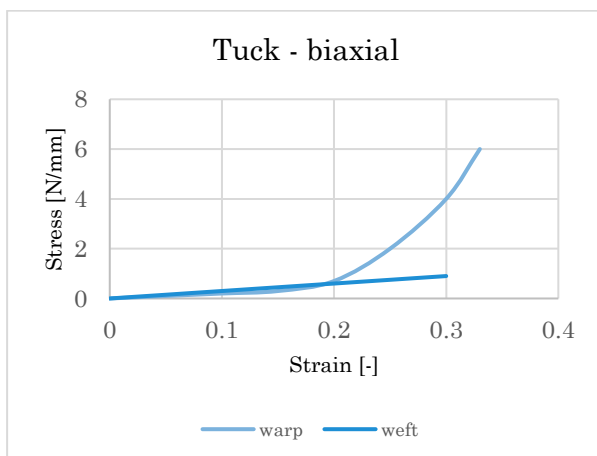
Subsequently, the raw data from Figure 4.7 is subjected to data cleaning and averaging to derive the final stress-strain relationships for both biaxial and uniaxial load cases for each knitting pattern. From these final stress-strain diagrams, the Young's moduli and Poisson's ratios are determined using Equations (4.1), (4.2), (4.3), and (4.4). The resulting material properties are presented in Table 4.1, offering valuable insights into the mechanical behaviour and characteristics of the knitted textile under different loading conditions for each knitting pattern.



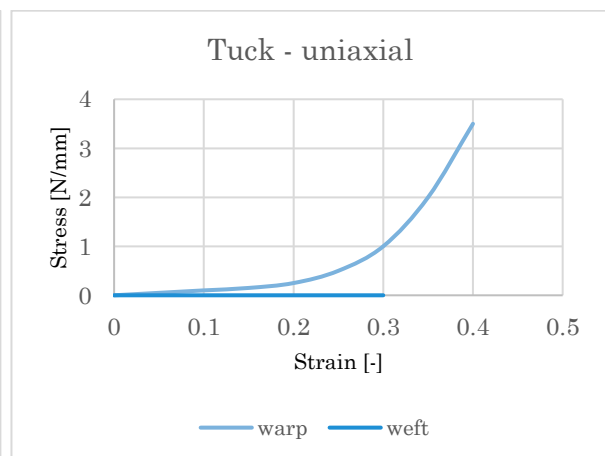
(a)



(d)



(b)



(e)

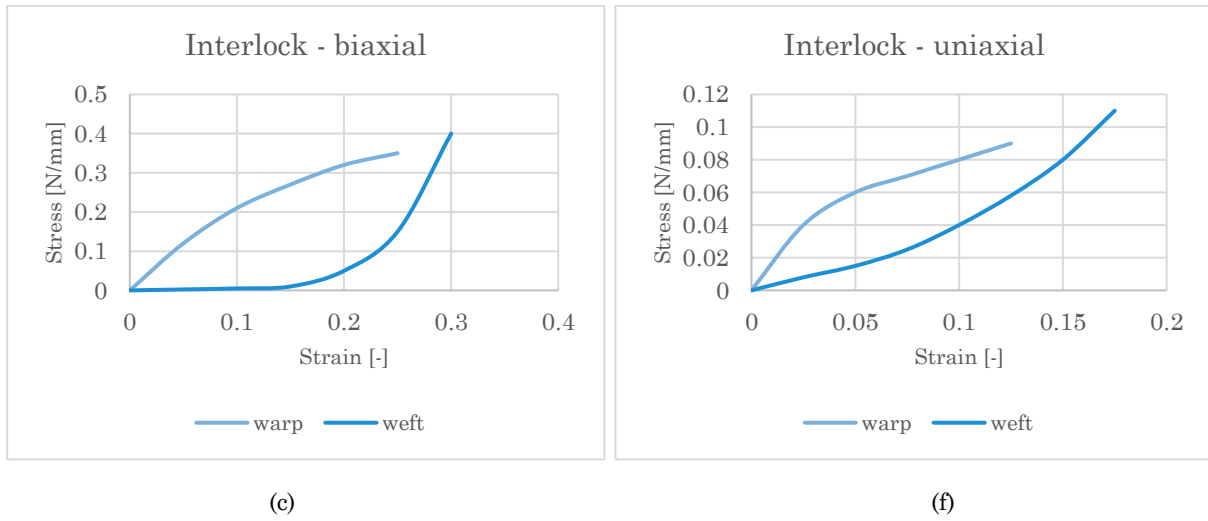


**Figure 4.7:** The final stress-strain plots for: (a) the hexagonal knit pattern loaded 1:1, (b) the tuck knit pattern loaded 1:1, (c) the interlock knit pattern loaded 1:1, (d) the hexagonal knit pattern loaded 1:0 and 0:1, (e) the tuck knit pattern loaded 1:0 and 0:1, (f) the interlock knit pattern loaded 1:0 and 0:1.

**Table 4.1:** Young's moduli and Poisson's ratios of the different knit architectures

Sample	$E_{y,I}$ [N/mm]	$E_{y,II}$ [N/mm]	$E_{x,I}$ [N/mm]	$E_{x,II}$ [N/mm]	$\nu_y$ [-]	$\nu_x$ [-]
Hexagonal	1 ( $\pm 0.85$ )	25.42 ( $\pm 0.83$ )	1 ( $\pm 1.17$ )	34.17 ( $\pm 7.50$ )	0.92 ( $\pm 0.07$ )	0.37 ( $\pm 0.05$ )
Tuck	1.25 ( $\pm 0.25$ )	34.54 ( $\pm 9.54$ )	0.05 ( $\pm 0.03$ )	-	2.08 ( $\pm 0.11$ )	0.52 ( $\pm 0.08$ )
Interlock	1.02 ( $\pm 0.95$ )	2.86 ( $\pm 1.66$ )	1.38 ( $\pm 0.22$ )	0.90 ( $\pm 0.30$ )	1.91 ( $\pm 0.50$ )	0.66 ( $\pm 0.47$ )

As expected, the tensile stiffness of the knitted textiles is notably low, characterised by initial Young's moduli ranging approximately between 1 ( $\pm 0.85$ ) and 1.38 ( $\pm 0.22$ ) N/mm. Among the knitting patterns, the tuck pattern exhibits the highest tensile stiffness of 34.54 ( $\pm 9.54$ ) N/mm in the warp direction. However, in the weft direction, this pattern necessitates substantial elongations before reaching the stiffening point, making it unattainable to obtain the second stage Young's modulus in this direction due to the size limitations of the testing set-up. On the other hand, the interlock pattern demonstrates the lowest overall tensile stiffness in both the weft and warp directions. In contrast, the hexagonal pattern displays superior stiffness properties, with second stage Young's moduli of 25.42 ( $\pm 0.83$ ) N/mm and 34.17 ( $\pm 7.50$ ) N/mm in the warp and weft directions, respectively.

Consistent with expectations, the Poisson's ratios exhibit considerable magnitudes, underscoring the anisotropic nature of the weft-knitted textiles. Notably, the tuck pattern's pronounced elongation in the weft direction, corresponds to a large Poisson's ratio of 2.08 ( $\pm 0.11$ ). In contrast, the hexagonal pattern showcases the most favourable Poisson's ratios among all the tested textiles, with  $\nu_y = 0.92$  ( $\pm 0.07$ ) and  $\nu_x = 0.37$  ( $\pm 0.05$ ). These findings emphasise the distinct mechanical behaviour of the knitted textiles in different directions,

with the hexagonal pattern demonstrating more balanced and desirable Poisson's ratios compared to the other knitting patterns.

In conclusion, the hexagonal knit pattern emerges as the preferred choice based on the results obtained from the biaxial tests. Its superior stiffness properties in comparison to the interlock pattern make it well-suited for the intended application. Additionally, the hexagonal pattern exhibits more desired ratios of Poisson's effect, as it does not demand significant initial elongation of the fabric before reaching the second stage of the hyper-elastic stress-strain curve. The consistent performance demonstrated by the hexagonal knitting pattern makes it the optimal candidate for fabricating the prototypes, as discussed further in Chapter 6.

## 4.2 Mortar properties

### 4.2.1 Mixture design and sample preparation

A flexible formwork is characterised by its large deformation during casting. To prevent the mortar from concentrating at the bottom, the consistency needs to be low enough that it doesn't flow easily but still workable enough to be able to apply with ease. Therefore the mixture design is based on optimizing the water-to-cement (w/c) ratio. Mixture designs in this study are formulated with w/c ratios of 30%, 35%, 40%, and 45%. A comprehensive overview of the specific mixture designs employed in this research is provided in Table 4.2.

**Table 4.2:** Recipe for the different mixtures

Type of component	M30	M35	M40	M45
<i>Mass per 1L [kg]</i>				
Water	0.190	0.222	0.254	0.285
Cement CEM III/B 42.5 N	0.634	0.634	0.634	0.634
Fine aggregates 0.125 – 0.25 mm	0.088	0.088	0.088	0.088
Fine aggregates 0.25 – 0.5 mm	0.131	0.131	0.131	0.131
Fine aggregates 0.5 – 1 mm	0.263	0.263	0.263	0.263
Fine aggregates 1 – 2 mm	0.394	0.394	0.394	0.394
Fine aggregates 2 – 4 mm	0.701	0.701	0.701	0.701
	<b>2.401</b>	<b>2.433</b>	<b>2.465</b>	<b>2.496</b>

During the mixing process of the mortar, achieving optimal workability is of great importance. The commonly employed approach in the concrete industry, known as the normal mixing approach (NMA), involves initially dry mixing all the solid materials, followed by the addition of water (and/or admixtures) for wet mixing until the concrete is formed (Zhao et al., 2022). This experimental work adopts the aforementioned mixing procedure. The specific steps involved in the mixing procedure are as follows:

## Chapter 4. Material characterisation

- Dry fine aggregates are mixed for a duration of 1 minute in the first step.
- Subsequently, the cement powder is added and mixed for an additional minute in the second step.
- Finally, water is gradually added at the end of the procedure and mixed for 2 minutes.

During this final step, mixing is initially conducted at a slow rate for 1 minute, followed by 30 seconds of fast mixing, and concluding with 30 seconds of slow mixing. Hand mixing is performed intermittently during these processes to ensure thorough incorporation of the dry mix with the water. A food-type mixer with a capacity of 2 L (Figure 4.8) is used to prepare the samples.



**Figure 4.8:** The mixer used to prepare the various mortar designs.

Following each batch mixing, a workability test is conducted in accordance with EN 1015-3:1999. The slump of the mortar is measured by filling and subsequently removing a truncated conical mould, as illustrated in Figure 4.9a. Additionally, the standard flow table test (Figure 4.9b) is employed to evaluate the spread of the mortar both before and after impacting the table.



**Figure 4.9:** Images of: (a) the slump test; (b) the standard flow table test.

Subsequently, the mortar specimens are cast into oil-coated foam moulds of  $40 \times 40 \times 160$  mm (Figure 4.10). To simulate the construction process, the samples are not compacted using vibrations, as this will not be possible with a flexible formwork. Following casting, each specimen is covered with a plastic sheet and stored at room temperature for 24 hours. Thereafter, the specimens are demoulded and transferred to a curing room with a temperature of  $20\text{ }^{\circ}\text{C}$  and a relative humidity of 85% for an additional 6 and 27 days. Mechanical testing is conducted 7 days after casting for the first test group, and after 28 days for the second test group.



**Figure 4.10:** A standard sized foam mould after casting the mortar.

#### 4.2.2 Flexural and compressive test configuration

A total of four mixture designs are tested to assess their flexural and compressive strength, following the guidelines outlined in EN 1015-11:1999. The flexural strength is

## Chapter 4. Material characterisation

evaluated using prisms with dimensions of  $40 \times 40 \times 160$  mm, while the compressive strength is determined from the halves of these prisms after flexural failure.

The flexural strength of the various mortar mixtures is determined by subjecting the prisms to a three-point bending test. A single concentrated force is applied at the centre of the span, gradually increasing until failure occurs. The distance between the support points is 100 mm. Figure 4.11 depicts the research element prepared for testing on the control machine. Table 4.3 provides the specific technical parameters associated with the bending test setup.



**Figure 4.11:** A specimen placed in the flexural test set-up and ready for testing.

**Table 4.3:** Technical parameters for the flexural strength test configuration

<b>Rate [kN/sec]</b>	0.100
<b>Start load [kN]</b>	0.100
<b>Stop load [%]</b>	20
<b>Area [mm<sup>2</sup>]</b>	266.67

Following the provisions outlined in EN 1015-11:1999, the compressive strength of the mortar is determined using the prism halves obtained from the bending tests. Axial compression is applied to the mortar specimens through steel plates with a square shape and dimensions of  $400 \times 400$  mm. Figure 4.12 illustrates the test specimen, prepared and ready for testing. Table 4.4 presents the specific technical parameters associated with the compression test setup.

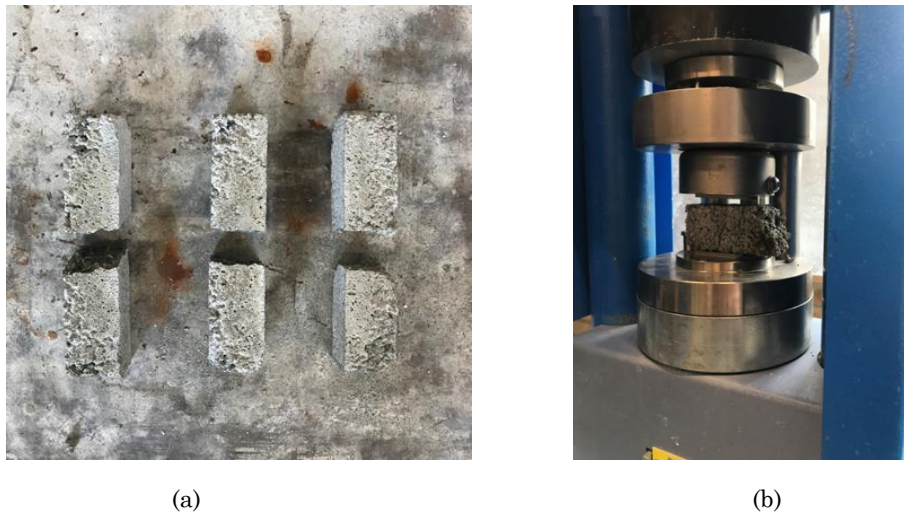


**Figure 4.12:** (a) the split prisms obtained from the flexural tests; (b) a halved prism placed in the compressive test set-up and ready for testing.

**Table 4.4:** Technical parameters for the flexural strength test configuration

<b>Rate [kN/sec]</b>	2.400
<b>Start load [kN]</b>	1.000
<b>Stop load [%]</b>	20
<b>Area [mm<sup>2</sup>]</b>	1600

### 4.2.3 Results and discussion

Table 4.5 provides the results of the slump and flow tests conducted for each mixture. Among the tested mixtures, M30, M35, and M40 exhibit no slump once the truncated conical mould is removed, indicating minimal flowability. Mixture M45 displayed a slump of 10 mm, indicating a limited degree of flow. Notably, as the water content increases, so does the flowability of the mixture, implying that higher water contents facilitated greater flow in the mortar

**Table 4.5:** Results of the slump and flow tests

<b>Mixture</b>	<b>Slump [mm]</b>	<b>Flow [mm]</b>
M30 (w/c = 30 %)	0	100
M35 (w/c = 35 %)	0	117
M40 (w/c = 40 %)	0	150
M45 (w/c = 45 %)	10	170

Figure 4.13 illustrates that the various mixtures lead to different surface finishes in the specimens. Notably, an increase in the w/c ratio results in a more compacted appearance

of the specimens. This observation can be attributed to the consistency of the mixture, where higher w/c ratios contribute to greater flowability and a higher degree of self-compaction. As a consequence, mixtures with higher flowability exhibit a more compacted surface finish in the specimens.

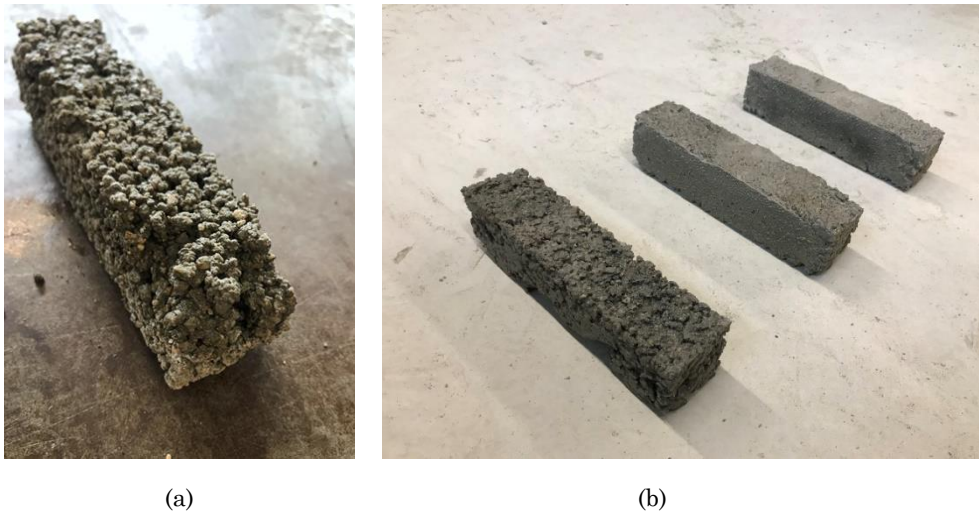


**Figure 4.13:** Specimen made with mixtures: (a) M30; (b) M35, M40, and M45 (from left to right).

Figure 4.14 presents the results of the three-point bending tests. The data indicates that the specimens with a water-to-cement ratio of 40% (M40) achieve the highest flexural strengths, measuring 12.43 ( $\pm 0.76$ ) MPa on the 7th day and 13.35 ( $\pm 0.16$ ) MPa on the 28th day. An evident increase in flexural strength is observed as the water-to-cement ratio increases up to 40%. However, beyond this ratio, a slight decline in flexural strength presents itself. As anticipated, the flexural strength of the test specimens exhibit a consistent increase with prolonged curing time.



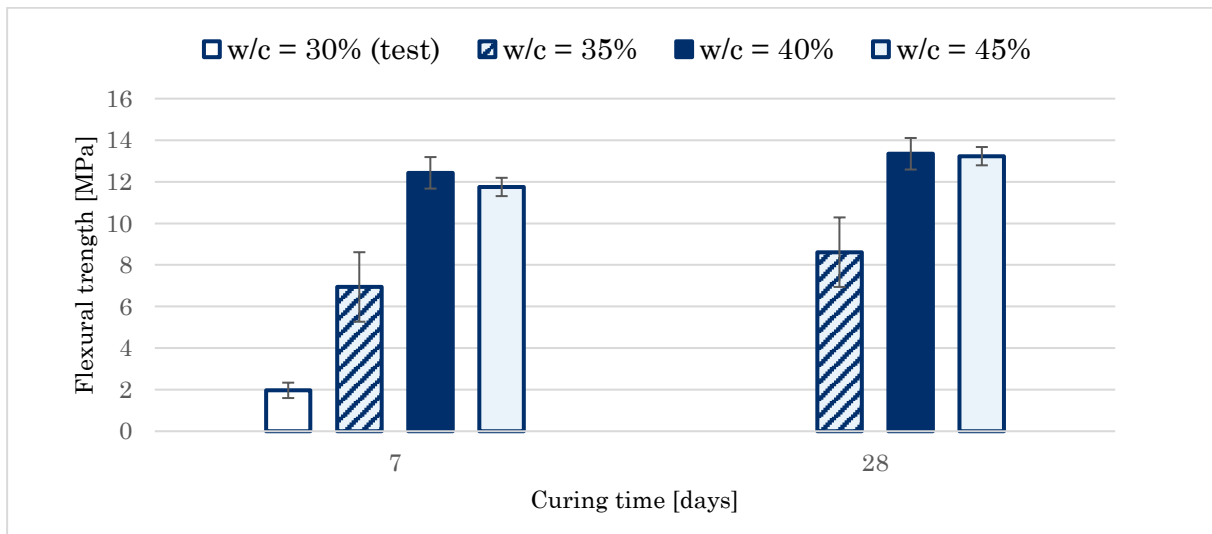


**Figure 4.14:** Flexural strength in relation with the curing time (days) for all tested mixtures.

The results of the compression tests are depicted in Figure 4.15. Among the tested specimens, those with a water-to-cement ratio of 40% (M40) exhibit the highest compressive strengths, measuring 39.66 ( $\pm 1.98$ ) MPa on the 7th day and 46.60 ( $\pm 5.29$ ) MPa on the 28th day, respectively. Similarly to the flexural test results, an increase in the w/c ratio up to 40% leads to a significant increase in compressive strength. However, beyond this threshold, a slight reduction in compressive strength is observed. As anticipated, the compressive strength of the test specimens demonstrates a consistent increase with curing time.

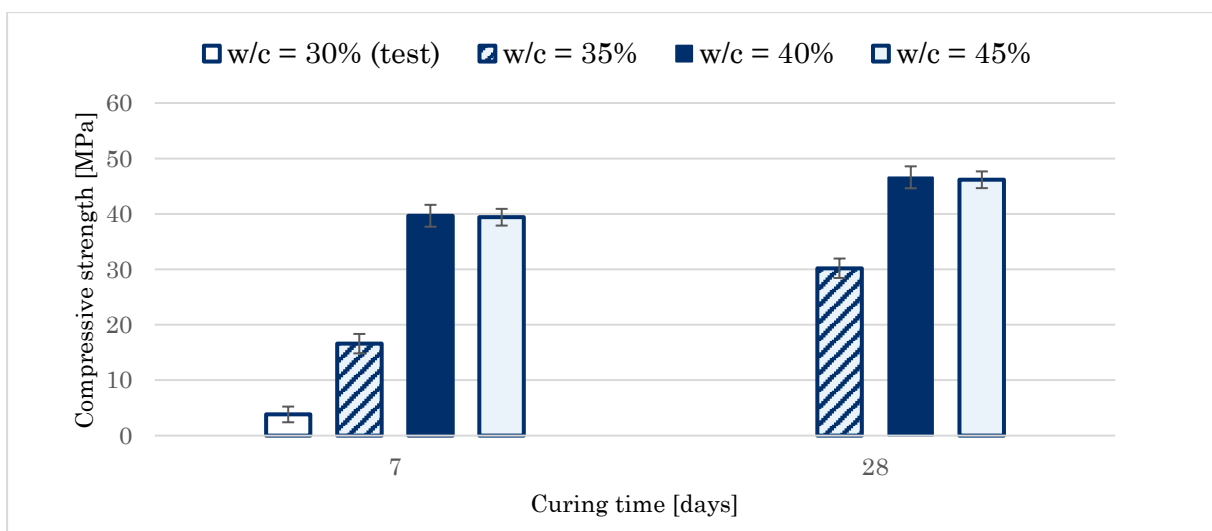


**Figure 4.15:** Compressive strength in relation with the curing time (days) for all tested mixtures.

The observed increase in both flexural and compressive strength with higher water-to-cement ratios can be attributed to the enhanced self-compacting. A more densely packed specimen with reduced entrapped air voids leads to improved mechanical strength. However, once the water-to-cement ratio exceeds 40%, the higher water content contributes to increased matrix porosity, adversely affecting the mechanical strength and initiating a decrease in strength. Furthermore, significant deviations in maximum strength are occasionally noticed among specimens with the same mixture. This variation can be attributed to the absence of mechanical compaction using vibration tables or pins. Since the specimens are only lightly compacted by hand, inconsistencies in compactness between samples may emerge, resulting in significantly lower flexural and compressive strength for specimens with inferior manual compaction.

To abide the set workability and consistency requirements while optimising the structural potential, the M40 mortar mixture is selected. This particular mixture exhibits adequate self-compaction while effectively preventing excessive flow during casting on steep surfaces. Furthermore, the M40 mixture demonstrates the highest levels of both flexural and compressive strength, making it suitable for use in structures with concrete strength classes up to C30/37 without the risk of it failing before the structural concrete.

Additionally, to further enhance the potential strength of the mortar used for constructing the prototypes (see Chapter 6), a systematic step-by-step application process will be implemented to ensure maximum compaction of the mortar. This comprehensive approach aims to maximise the strength and integrity of the final structure.

# 5. Membrane model

Given the lack of Finite Element Analysis (FEA) tools capable of accurately simulating the deflection behaviour in weft-knitted formworks, and with an academic motivation to gain deeper insights into the deflection characteristics of such membranes, this chapter embarks on developing membrane deflection models using (semi-)analytical methods. Section 5.1 introduces the fundamentals of membrane theory. In Section 5.2, the derivation process of the vertical equilibrium equation for uniformly loaded rectangular membranes is elucidated. Section 5.3 presents the linear model and outlines an analytical approach for its solution. Lastly, Section 5.4 presents the nonlinear models and the (semi-)analytical methods to solve or approximate their solution.

## 5.1 Introduction to membrane theory

A membrane is defined as a flat structural element with thickness much smaller than its other dimensions (Leissa & Qatu, 2011). It lacks flexural rigidity, making it incapable of withstanding bending loads. It can also only endure tensile loads, causing it to be vulnerable to wrinkling when subjected to compressive forces. The displacement ( $w$ ) of the membrane is described as a function of two spatial variables ( $x$  and  $y$ ), denoted as  $w(x, y)$ , making it a two-dimensional generalisation of a string.

For a structure to qualify as a membrane, it must satisfy the following conditions, as summarised from Ventsel and Krauthammer (2001):

1. Boundaries are free from transverse shear forces and moments. Any applied loads must lie out of plane to the middle surface.
2. The normal displacements and rotations at the edges are unconstrained, allowing these edges to displace freely in the direction of the normal to the middle surface.
3. The membrane should possess a smoothly varying, continuous surface.
4. The components of surface and edge loads must be smooth and continuous functions of the coordinates.

To gain a deeper understanding of the distinction between plates and membranes, the equation that defines the flexural rigidity of a plate can be analysed (Ventsel & Krauthammer, 2001):

$$D = \frac{Eh^3}{12(1-\nu^2)}, \quad (5.5)$$

where  $E$  is the elastic modulus of the material,  $h$  is the thickness of the material, and  $\nu$  is Poisson's ratio. It is noteworthy that as the thickness ( $h$ ) of a structural element decreases, the flexural rigidity ( $D$ ), as given in the equation above approaches zero. This particular limit provides a mathematical demonstration of the transformation of a structural element from a thin plate to a membrane (Ventsel & Krauthammer, 2001).

## 5.2 Derivation of vertical equilibrium equation for uniformly loaded rectangular membranes

Figure 1.1 illustrates a three-dimensional depiction of an infinitesimal element in a representative displaced configuration. This element is positioned at the middle surface of the membrane and has dimensions  $dx \times dy$  in the plane of the membrane and a thickness  $h$ . The membrane stress resultants ( $T_x$ ,  $T_{xy}$ , etc.) acting on each side of the element are displayed. These resultants have force per unit tangent length dimensions and are related to the stresses by  $T_x = \sigma_x h$ ,  $T_{xy} = \tau_{xy} h$ , and so forth. Here,  $T_x$  and  $T_y$  represent normal stress resultants, while  $T_{xy}$  and  $T_{yx}$  correspond to shear stress resultants. The orientation of these stress resultants conforms to the conventional notation employed in the theory of elasticity (Timoshenko & Woinowsky-Krieger, 1985). Additionally, the figure includes a pressure ( $p$ ) distributed over the membrane's surface, measured in units of force per area.

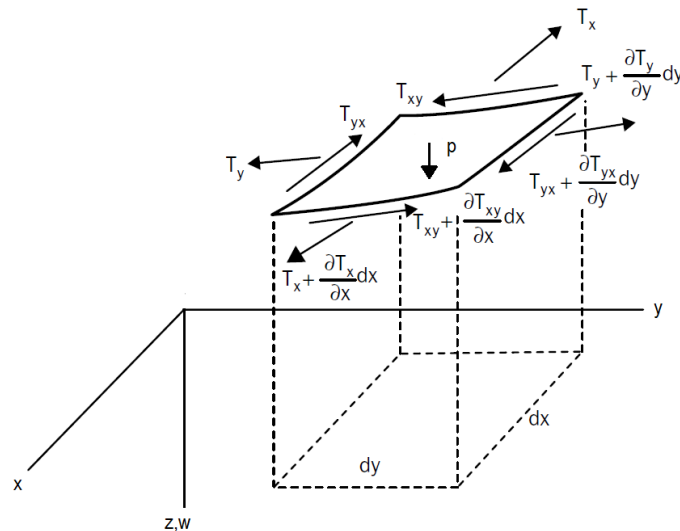


**Figure 5.1:** Free body diagram of an infinitesimal part of a rectangular membrane (adopted from Leissa & Qatu, 2011)

Given the assumption that the displacements cause small slopes in all directions and at all points on the membrane, the force equilibrium in the z-direction is expressed. The first order differential quantities cancel each other out, thus reducing the extent of the equilibrium equation. Dividing the whole equilibrium equation by the area  $dxdy$ , defining that  $T_{xy} = T_{yx}$  (internal moment equilibrium), and taking the limit of  $dx$  and  $dy$  to zero gives the final membrane equation (Leissa & Qatu, 2011).

$$\frac{\partial}{\partial x} \left( T_x \frac{\partial w}{\partial x} \right) + \frac{\partial}{\partial y} \left( T_y \frac{\partial w}{\partial y} \right) + \frac{\partial}{\partial x} \left( T_{xy} \frac{\partial w}{\partial y} \right) + \frac{\partial}{\partial y} \left( T_{xy} \frac{\partial w}{\partial x} \right) = -p \quad (5.6)$$

The membrane stresses  $T_x$ ,  $T_y$ , and  $T_{xy}$  in Equation 5.2 depend on the strain of the membrane. Assuming that there are no external forces in x-, and y-direction and the load is perpendicular to the membrane, the equations of equilibrium of an element in the xy plane are (Leissa & Qatu, 2011):

$$\frac{\partial T_x}{\partial x} + \frac{\partial T_{xy}}{\partial y} = 0 \quad (5.7)$$

$$\frac{\partial T_y}{\partial y} + \frac{\partial T_{xy}}{\partial x} = 0 \quad (5.8)$$

Multiplying Equation (5.3) by  $\frac{\partial w}{\partial x}$ , and Equation (5.4) by  $\frac{\partial w}{\partial y}$ , and then subtracting both from (5.2), the latter becomes:

$$T_x \frac{\partial^2 w}{\partial x^2} + 2T_{xy} \frac{\partial^2 w}{\partial x \partial y} + T_y \frac{\partial^2 w}{\partial y^2} = -p \quad (5.9)$$

Equation (5.5) serves as the foundational framework for deriving both the linear and non-linear membrane deflection solutions, which will be investigated in Sections 5.3 and 5.4, respectively.

### 5.3 Derivation of linear membrane deflection solution

The solution to the linearised membrane equation serves as a good preliminary approximation, effectively streamlining the complexity of the problem by simplifying the stress-strain interrelationships within the membrane. Nonetheless, this solution is suitable solely for small deflections, as its accuracy diminishes with increasing deflection magnitudes.

### 5.3.1 Assumptions

To characterise the membrane as a linear system, it necessitates the adoption of the following foundational assumptions:

1. The slope, caused by out-of-plane displacement ( $w$ ), is considered small.
2. The effect of the in-plane displacements ( $u$  and  $v$ ) on the gross response of the membrane are negligible when compared with the deflection ( $w$ ).

Given these assumptions, for small slopes, the deflection behaviour remains independent of the membrane material and relies solely on the applied tension stress.

### 5.3.2 Linear solution

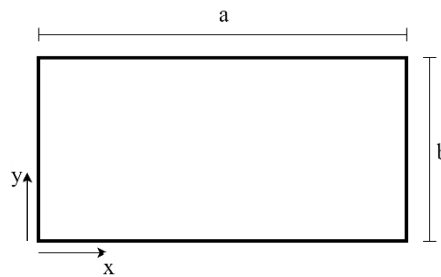


**Figure 5.2:** A rectangular membrane with dimensions  $a$  and  $b$ , where the coordinate origin is taken at the bottom-left corner.

The boundary conditions (BC), derived from Figure 5.2, are denoted as:

$$\begin{aligned} w(0, y) &= 0 \\ w(a, y) &= 0 \\ w(x, 0) &= 0 \\ w(x, b) &= 0 \end{aligned} \tag{5.10}$$

The solution for the displacement  $w$  can also be assumed with the proviso that it adheres to the specified BC. These BC, as expressed in Equation (5.6), have been demonstrated in literature (Levy, 1942; Timoshenko & Woinowsky-Krieger, 1985) to be fulfilled by the following Fourier series:

$$w(x, y) = \sum_{m,n=1}^{\infty} W_{mn} \sin\left(\frac{m\pi x}{a}\right) \sin\left(\frac{n\pi y}{b}\right) \tag{5.11}$$

where  $W_{mn}$  is the coefficient of the infinite series solution. Next, Equation (5.7) is substituted into Equation (5.5) to give:

$$W_{mn} \sin\left(\frac{m\pi x}{a}\right) \sin\left(\frac{n\pi y}{b}\right) = -\frac{p}{T_x \frac{m^2 \pi^2 x^2}{a^2} + T_{xy} \frac{mn \pi^2 xy}{ab} + T_y \frac{n^2 \pi^2 y^2}{b^2}} \tag{5.12}$$

Multiplying both sides of Equation (5.8) by  $\sin\left(\frac{i\pi x}{a}\right)\sin\left(\frac{j\pi y}{b}\right)$ , where  $i$  and  $j$  also are integers, and integrating over the area of the membrane, it is seen that:

$$\begin{aligned} & \int_0^a \int_0^b W_{mn} \sin\left(\frac{m\pi x}{a}\right) \sin\left(\frac{n\pi y}{b}\right) \cdot \sin\left(\frac{i\pi x}{a}\right) \sin\left(\frac{j\pi y}{b}\right) dx dy \\ &= - \int_0^a \int_0^b \frac{p}{T_x \frac{m^2 \pi^2 x^2}{a^2} + T_{xy} \frac{mn \pi^2 xy}{ab} + T_y \frac{n^2 \pi^2 y^2}{b^2}} \sin\left(\frac{i\pi x}{a}\right) \sin\left(\frac{j\pi y}{b}\right) dx dy \end{aligned} \quad (5.13)$$

$$\begin{aligned} & \int_0^a \int_0^b \sin\left(\frac{m\pi x}{a}\right) \sin\left(\frac{n\pi y}{b}\right) \cdot \sin\left(\frac{i\pi x}{a}\right) \sin\left(\frac{j\pi y}{b}\right) dx dy \\ &= \begin{cases} 0, & \text{if } i \neq m, \text{ or } j \neq n \\ \frac{ab}{4}, & \text{if } i = m, \text{ or } j = n \end{cases} \end{aligned} \quad (5.14)$$

Next, the orthogonality properties are used to determine the amplitudes  $W_{mn}$ . Equations (5.9) and (5.10), then, result in the formulation of  $W_{mn}$ , which in this case is a coefficient of double Fourier series:

$$W_{mn} = -\frac{4}{ab} \int_0^a \int_0^b \frac{p}{T_x \frac{m^2 \pi^2 x^2}{a^2} + T_{xy} \frac{mn \pi^2 xy}{ab} + T_y \frac{n^2 \pi^2 y^2}{b^2}} \sin\left(\frac{m\pi x}{a}\right) \sin\left(\frac{n\pi y}{b}\right) dx dy \quad (5.15)$$

The obtained linear solution for the displacement  $w$  will be used to predict the deflection of the textile formwork under hydrostatic pressure within the prototype fabrication process (refer to Chapter 6).

## 5.4 Derivation of nonlinear membrane deflection solution

As previously highlighted, the linear membrane deflection model provides a simple initial estimate suitable for small deflections in a membrane. However, within the context of a weft-knitted textile formwork, substantial deflections are expected. Hence, the application of large deflection theory becomes imperative. The forthcoming nonlinear model, based on this theory, consequently necessitates the incorporation of the orthotropic characteristics of the membrane material and their implications on internal stress-strain relations. Furthermore, the model accounts for the influence of in-plane displacements on the overall deflection behaviour of the membrane.

In this section, two distinct approaches are described. The first approach, (to the author's best knowledge) was originally proposed by Timoshenko & Woinowsky-Krieger (1985) and is subsequently modified to align with the specific requirements of this research (i.e., orthotropic material properties and rectangular geometries), utilises the energy method to approximate the solution for membrane deflection. The second approach, originally

obtained by Föppl (1907), necessitates the introduction of an additional equation, complementing Equation (5.5), to facilitate the deflection solution. The first method can be solved analytically, whereas the second method mandates numerical solution procedures. It is also important to mention that the first approach is an approximation which does not properly satisfy the equation of motion, while the second one, although an approximation, does satisfy the equation of motion provided that an infinite number of components is used in the series.

The equations for the membrane forces  $T_x$ ,  $T_y$ , and  $T_{xy}$  are derived from the kinematic and constitutive equations. In structural mechanics, kinematic equations relate strains to displacement. The total membrane strains in the x- and y-directions result from both extension and rotation, and for large deflections, they can be expressed using the following equations (Timoshenko & Woinowsky-Krieger, 1985)

$$\varepsilon_x = \frac{\partial u}{\partial x} + \frac{1}{2} \left( \frac{\partial w}{\partial x} \right)^2 \quad (5.16)$$

$$\varepsilon_y = \frac{\partial v}{\partial y} + \frac{1}{2} \left( \frac{\partial w}{\partial y} \right)^2 \quad (5.17)$$

$$\gamma_{xy} = \frac{\partial u}{\partial y} + \frac{\partial v}{\partial x} + \frac{\partial w}{\partial x} \frac{\partial w}{\partial y} \quad (5.18)$$

Where,  $u(x, y)$  and  $v(x, y)$  are the in-plane displacements in x-, and y-direction, respectively, and  $w(x, y)$  is the out-of-plane displacement in z-direction.

In structural mechanics, constitutive equations characterise stress-strain relations. The membrane strains in the x- and y-directions result from elongation in the loading direction and perpendicular shortening due to the Poisson effect. These relations are formulated as equations (Timoshenko, 1985):

$$\varepsilon_x = \frac{1}{E_x h} (T_x - \nu_y T_y) \quad (5.19)$$

$$\varepsilon_y = \frac{1}{E_y h} (T_y - \nu_x T_x) \quad (5.20)$$

$$\gamma_{xy} = \frac{1}{G_{xy} h} T_{xy} \quad (5.21)$$

By substituting Equation (5.12) into Equation (5.15), Equation (5.13) into Equation (5.16), and Equation (5.14) into Equation (5.17) and subsequently solving, the expressions defining the membrane forces  $T_x$ ,  $T_y$ , and  $T_{xy}$  as functions of  $u$ ,  $v$  and  $w$  are obtained:

$$T_x = \frac{h(E_y \nu_y \left( \frac{\partial v}{\partial y} + \frac{1}{2} \left( \frac{\partial w}{\partial y} \right)^2 \right) + E_x \left( \frac{\partial u}{\partial x} + \frac{1}{2} \left( \frac{\partial w}{\partial x} \right)^2 \right))}{\nu_x \nu_y - 1} \quad (5.22)$$



$$T_y = \frac{h(E_x \nu_x \left( \frac{\partial u}{\partial x} + \frac{1}{2} \left( \frac{\partial w}{\partial x} \right)^2 \right) + E_y \left( \frac{\partial v}{\partial y} + \frac{1}{2} \left( \frac{\partial w}{\partial y} \right)^2 \right))}{\nu_x \nu_y - 1} \quad (5.23)$$

$$T_{xy} = G_{xy} \left( \frac{\partial u}{\partial y} + \frac{\partial v}{\partial x} + \frac{\partial w}{\partial x} \frac{\partial w}{\partial y} \right) \quad (5.24)$$

### 5.4.1 Energy-method solution

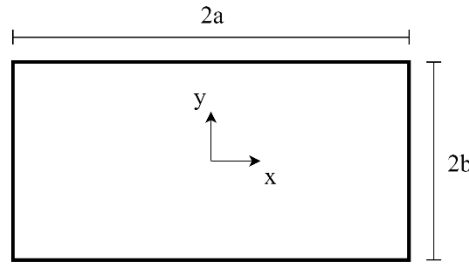


**Figure 5.3:** A rectangular membrane with dimensions  $2a$  and  $2b$ , where the coordinate origin is taken at the centre.

The strain energy of a rectangular membrane (Figure 5.3), which is due solely to stretching of its middle surface, is given by the expression:

$$U_{strain} = \frac{1}{2} \int_{-a}^a \int_{-b}^b (T_x \varepsilon_x + T_y \varepsilon_y + T_{xy} \gamma_{xy}) dx dy \quad (5.25)$$

Subsequently, substitute Equations (5.12-5.14) and Equations (5.18-5.20) into Equation (5.21) to formulate an expression for the strain energy that is a function of the displacements  $u$ ,  $v$  and  $w$ .

Next, suitable expressions need to be assumed for the displacements  $u$ ,  $v$  and  $w$ . These expressions should adhere to the established BC and will involve various arbitrary parameters. Determining the magnitudes of these parameters is accomplished by applying the principle of virtual displacements. For the case of a uniformly loaded rectangular membrane with dimensions  $2a$  and  $2b$  (Figure 5.2), the displacements  $u$ ,  $v$  and  $w$  must be zero at the boundaries. Moreover, symmetry dictates that  $w$  is an even function of  $x$  and  $y$ , whereas  $u$  and  $v$  are odd functions of  $x$  and of  $y$ , respectively. These criteria are met by using the following displacement expressions:

$$u = c_1 \sin\left(\frac{\pi x}{a}\right) \cos\left(\frac{\pi y}{2b}\right) \quad (5.26)$$

$$v = c_2 \sin\left(\frac{\pi y}{b}\right) \cos\left(\frac{\pi x}{2a}\right) \quad (5.27)$$

$$w = w_0 \cos\left(\frac{\pi x}{2a}\right) \cos\left(\frac{\pi y}{2b}\right) \quad (5.28)$$

These solutions, although they satisfy the BC, do not satisfy the nonlinear equation of motion. Nonetheless, it could represent a reasonable approximation.

These functions are then substituted into Equation (5.25). From the principle of virtual displacement the following three equations are derived:

$$\frac{\partial U_{strain}}{\partial c_1} = 0 \quad (5.29)$$

$$\frac{\partial U_{strain}}{\partial c_2} = 0 \quad (5.30)$$

$$\frac{\partial U_{strain}}{\partial w_0} \delta w_0 = \int_{-a}^a \int_{-b}^b p \delta w_0 \cos\left(\frac{\pi x}{2a}\right) \cos\left(\frac{\pi y}{2b}\right) dx dy \quad (5.31)$$

Solving Equations (5.25-5.27) yields the expressions for the parameters  $c_1$ ,  $c_2$ , and  $w_0$ .

### 5.4.2 Fourier series expansion method

The preceding section outlined a loose approximation of the nonlinear membrane deflection solution. In this section, a more precise solution for the nonlinear problem is presented. This approach requires two equations: a modified version of the vertical force equilibrium equation derived from Equation (5.5), and a consistency equation.

The consistency equation is obtained by taking the second derivatives of the strain expressions (Equations (5-12-5.14)) (Timoshenko & Woinowsky-Krieger, 1985):

$$\frac{\partial^2 \varepsilon_x}{\partial y^2} + \frac{\partial^2 \varepsilon_y}{\partial x^2} - \frac{\partial^2 \gamma_{xy}}{\partial x \partial y} = \left( \frac{\partial^2 w}{\partial x \partial y} \right)^2 - \frac{\partial^2 w}{\partial x^2} \frac{\partial^2 w}{\partial y^2} \quad (5.32)$$

Replacing the strain components with the constitutive expressions gives an equation in terms of  $T_x$ ,  $T_y$ , and  $T_{xy}$ :

$$\frac{\frac{\partial^2 T_x}{\partial y^2} - \nu_y \frac{\partial^2 T_y}{\partial y^2}}{E_x h} + \frac{\frac{\partial^2 T_y}{\partial x^2} - \nu_x \frac{\partial^2 T_x}{\partial x^2}}{E_y h} - \frac{\partial^2 T_{xy}}{\partial x \partial y} = \left( \frac{\partial^2 w}{\partial x \partial y} \right)^2 - \frac{\partial^2 w}{\partial x^2} \frac{\partial^2 w}{\partial y^2} \quad (5.33)$$

The solutions of Equations (5.15-5.17) are greatly simplified by the introduction of the (Airy) stress function (Airy, 1863). As is easily checked, Equations (5.3) and (5.4) are satisfied by taking an arbitrary unknown function  $\phi$  of  $x$  and  $y$  and putting the following expressions for the stress components:

$$T_x = h \frac{\partial^2 \phi}{\partial y^2} \quad (5.34)$$

$$T_y = h \frac{\partial^2 \phi}{\partial x^2} \quad (5.35)$$

$$T_{xy} = -h \frac{\partial^2 \phi}{\partial x \partial y} \quad (5.36)$$

If these expressions for the forces are substituted in Equation (5.29) the final equation is obtained:

$$\frac{1}{E_x} \frac{\partial^4 \phi}{\partial y^4} + \frac{1}{E_y} \frac{\partial^4 \phi}{\partial x^4} - \frac{E_x E_y - G_{xy} E_x \nu_x - G_{xy} E_y \nu_y}{E_x E_y G_{xy}} \frac{\partial^4 \phi}{\partial x^2 \partial y^2} = \left( \frac{\partial^2 w}{\partial x \partial y} \right)^2 - \frac{\partial^2 w}{\partial x^2} \frac{\partial^2 w}{\partial y^2} \quad (5.37)$$

The second equation necessary to determine  $\phi$  and  $w$  is obtained by substituting expressions (5.30) – (5.31) into the original vertical force equilibrium equation, denoted as Equation (5.5). This procedure yields the following equation:

$$\frac{\partial^2 \phi}{\partial y^2} \frac{\partial^2 w}{\partial x^2} + \frac{\partial^2 \phi}{\partial x^2} \frac{\partial^2 w}{\partial y^2} - 2 \frac{\partial^2 \phi}{\partial x \partial y} \frac{\partial^2 w}{\partial x \partial y} = -\frac{p}{h} \quad (5.38)$$

Now that the two core equations are established, the next step is to assume the solutions for  $\phi$  and  $w$  that satisfy the BC. This process follows the same approach as employed in Section 5.3 for the linear model. The assumed solution for  $w$  is already defined in Equation (5.7). Similarly the vertical pressure  $p$  can be expressed through a double Fourier series:

$$p(x, y) = \sum_{m,n=1}^{\infty} P_{mn} \sin\left(\frac{m\pi x}{a}\right) \sin\left(\frac{n\pi y}{b}\right) \quad (5.39)$$

In existing literature (Levy, 1942; Seide, 1977; Timoshenko & Woinowsky-Krieger, 1985) suitable expression for the stress function  $\phi$  is found to be in the form:

$$\phi(x, y) = \frac{T_x y^2}{2ah} + \frac{T_y x^2}{2bh} + \sum_{m,n=0}^{\infty} \Phi_{mn} \cos\left(\frac{m\pi x}{a}\right) \cos\left(\frac{n\pi y}{b}\right) \quad (5.40)$$

Upon establishing the assumed solutions, Equations (5.7), (5.35), and (5.36) are substituted into Equations (5.33) and (5.34). This gives a system of two nonlinear algebraic equations, which can be solved numerically using a preferred method (e.g., mathematical optimisation or finite difference).





**Part III:  
Results**



# 6. Prototypes

This chapter is dedicated to validating the membrane models introduced in Chapter 5 through the construction of physical prototypes and the subsequent comparison with model-generated results. Section 6.1 provides a comprehensive exposition of the design, deflection model, the geometrical measurement, and comparison procedures for the squared prototype. Subsequently, in Section 6.2, the same steps are detailed for the rectangular prototype, encompassing its design, deflection model, the geometrical measurement, and comparative analyses.

## 6.1 Prototyping framework and construction strategy

The prototypes constructed for this study share the same forming system, prefabrication steps, and construction procedure. The sole differences among them relate to the boundary geometry and structural dimensions. Consequently, this section is dedicated to elucidating the overarching prototyping framework and construction strategy.

### 6.1.1 System

Figure 6.1 shows an exploded axonometric view of the formwork system, comprising of several key components for the construction process:

- The timber frame (a) serves as primary support for the structure during its early stages until it attains sufficient strength. Simultaneously, plywood plate (b) is employed to temporarily support the textile, facilitating the easy and controlled application of mortar.
- The stay-in-place formwork layer consists of a custom knitted textile (e) with integrated channels to accommodate the insertion of bars (d). These bars are essential for uniformly distributing the prestress on the textile when it is loaded with weighted sandbags (c).
- Following prestressing, a layer of mortar (f) is uniformly applied onto the formwork, causing the textile membrane to deflect and ultimately take its final intended shape.

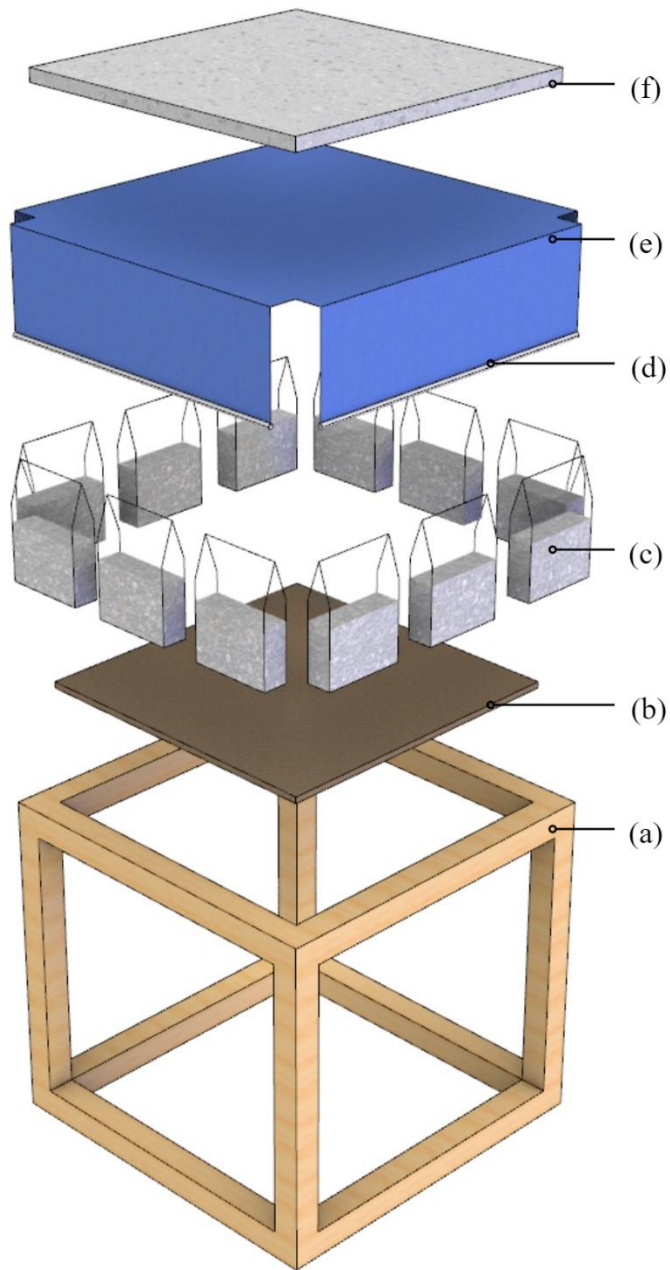


**Figure 6.1:** Exploded view of the forming system: (a) timber frame; (b) temporary support plate; (c) weighted sandbags; (d) bars; (e) knitted textile; (f) mortar.



## 6.1.2 Prefabrication

The prefabrication process of the flexible formwork consists of three parts. Initially, an external frame is constructed to provide structural support and containment. Then, the bespoke weft-knitted textile is fabricated to exact specifications, incorporating channels and tailored to the desired geometry. Lastly, the optimum mixture design selected in Chapter 4 is mixed, ensuring appropriate consistency and flowability for its application onto the textile formwork.

The external frame (Figure 6.2a) is built out of 44 x 44 mm timber elements, specifically arranged to form a structurally robust framework. The design of the frame is configured to feature a precisely measured opening at the top, meeting the dimensions of the designed shell structure. A timber plate (Figure 6.2b) is precisely cut to match the exact dimensions of this opening, ensuring a snug fit within the designated space.



**Figure 6.2:** The base of the formwork: (a) external timber frame; (b) precisely cut plywood plate that fits in the opening.

Both prototypes are built using a knitted textile with a hexagonal pattern as flexible formwork. To simplify the process, the knitting pattern previously used for the hexagonal cruciform specimen described in Chapter 4 are scaled up to match with the desired dimensions of the current design. Consequently, the dimension of the arms and channels are maintained. As for the yarn parameters, the same material and amount of yarn are used as prescribed in Chapter 4 four PES yarns per guide.

The mortar used for this prototype is based on design mixture M40<sup>1</sup>, which is deemed to exhibit the most favourable flowability-to-workability relationship based on prior assessments (see Chapter 4). The mixing procedure adheres to the guidelines outlined in the normal mixing approach (NMA), as described in Chapter 4.

<sup>1</sup>M40 is the mortar mixture design with a water-to-cement ratio of 40% (see Section 4.2)

### 6.1.3 Construction

The construction process of the element comprises three sequential phases. Initially, the formwork system is assembled, and the appropriate amount of prestress is introduced. Subsequently, the application of mortar follows, ensuring the proper thickness throughout. Lastly, a crucial waiting period is observed, allowing sufficient time for the mortar to strengthen adequately. Once the requisite strength is achieved, the element is demoulded, resulting in the finished structure.

#### Formwork assembly

The construction process involves several crucial steps. Firstly, a temporarily wooden plate is carefully positioned within the opening of the external frame. Prior to casting the mortar onto the textile, the textile itself must undergo prestressing. This is achieved by employing 4 mm steel rods that are inserted into the textile's channels, ensuring even distribution of tension across its width. Subsequently, weighted sandbags are symmetrically hooked onto the rods, facilitating equal prestressing on both sides. The weight of the sandbags is calculated to result in prestress values of 0.1 N/mm in both x- and y-direction. The resulting tensioned formworks can be seen in Figure 6.3. With the weft-knitted formwork now prestressed, the mortar can be effectively cast on top.



**Figure 6.3:** The prestressed fabrics: (a) squared geometry; (b) rectangular geometry.

#### Concreting

During the construction process, the mortar is applied manually onto the textile, as depicted in Figure 6.4a-b. This is done diligently to ensure a uniform thickness of the mortar layer across the entire textile surface (Figure 6.4c). Subsequently, the temporary plate positioned beneath the textile is removed to allow the textile to take its intended deformed shape (Figure 6.4d). Notably, uncoated edges emerge during this stage (Figure 6.4e), which are promptly covered with a uniform layer of mortar. Once the entire textile is

evenly covered with mortar, both the top and bottom surfaces are covered with foil (Figure 6.4f) to prevent excessive drying during the 7-day hardening period. To minimise any potential unwanted deformation of the formwork system, all forms of vibrations are avoided throughout the casting period and for the subsequent 7-day period. Upon reaching the seventh day, with the mortar having attained sufficient strength, the structural element is extracted from the formwork and allowed to continue curing until the 28<sup>th</sup> day.

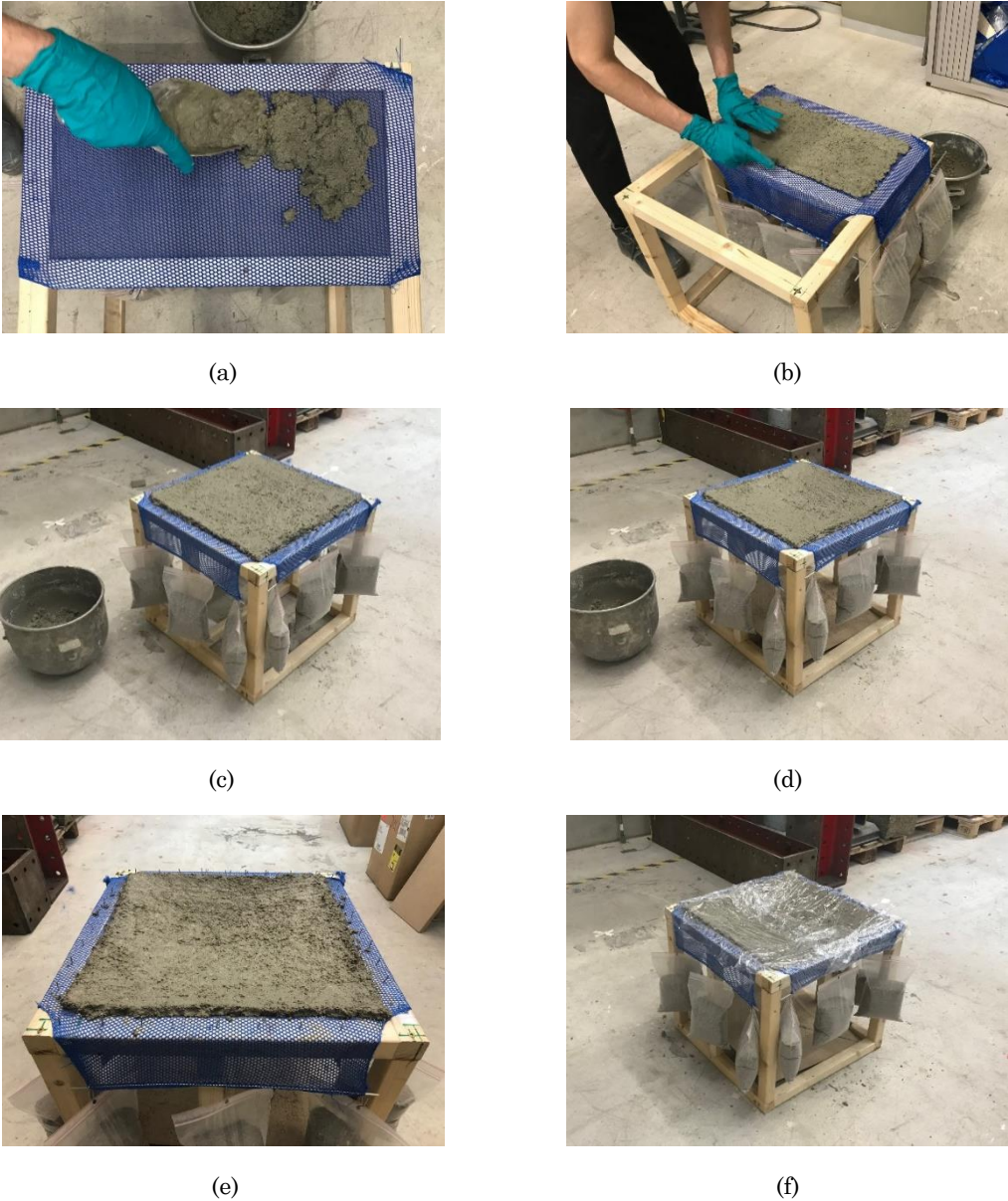


**Figure 6.4:** The concreting process: (a) application of a mortar layer onto the formwork; (b) uniform distribution achieved manually; (c) measurement of thickness at distinct reference points; (d) temporary support removal, enabling the formwork to assume its intended shape; (e) filling of exposed textile sections with mortar; (f) covering of the formwork using foil.

## 6.2 Squared shell



**Figure 6.5:** Finished squared shell prototype

### 6.2.1 Design

This first double-curved funicular shell is constructed to evaluate the accuracy of the models for geometries with the same dimensions in both directions. Furthermore, the design takes practical constraints in mind, including available space and manoeuvrability within the laboratory. Consequently, the prototype's dimensions are restricted, resulting in a chosen length and width of 500 mm, and a height of 65 mm. The thickness of the mortar layer is selected to result in the desired membrane deflection. For this prototype, a mortar layer thickness of 15 mm is adopted to meet the specific design preferences and experimental objectives.

### 6.2.2 Model

To predict the final geometry of the structure after the casting process, the linear membrane model and nonlinear energy-method are used. The input parameters for the linear membrane model are given in Table 6.1. This model assumes constant tensile stresses ( $T_x$ ,  $T_y$ ) in the x- and y-direction. These stresses are equal to the applied prestresses at the boundaries of the membrane. For this specific case the prestresses are set to be equal in both directions. Furthermore, the hydrostatic pressure ( $p$ ) is calculated using the thickness and the mortar density given in Table 4.2.

**Table 6.1:** Input parameters used for the linear membrane model

Parameters	
Width in x-direction (a)	500 [mm]
Length in y-direction (b)	500 [mm]
Tensile stress in x-direction ( $T_x$ )	0.1 [N/mm]
Tensile stress in y-direction ( $T_y$ )	0.1 [N/mm]
Shear stress ( $T_{xy}$ )	0 [N/mm]
Hydrostatic pressure (p)	$2.418 \cdot 10^{-4}$ [N/mm <sup>2</sup> ]

The deflection contour plot that results from the linear membrane model is shown in Figure 6.6. The maximum deflection at the midpoint of the membrane is predicted to be 65.02 mm. Figure 6.7 gives a visual representation of the resulting shell geometry upon inversion.

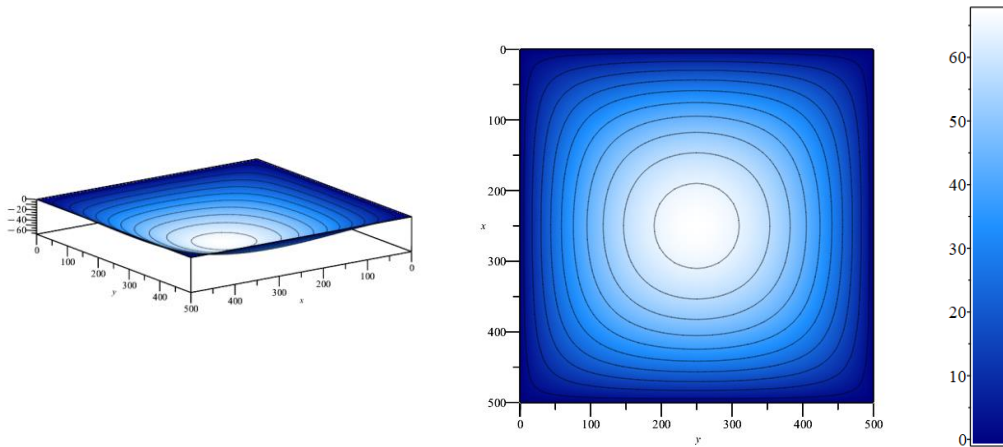


**Figure 6.6:** Contour plots of membrane deflection in mm, according to the linear model



**Figure 6.7:** Resulting shell geometry, according to the linear model

The nonlinear model, based on the energy-method, requires additional input parameters (see Table 6.2). These are the parameters that relate to the orthotropic material properties of the modelled knitted membrane.

**Table 6.2:** Additional input parameters used for the energy-method model

Parameters	
Young's modulus in x-direction ( $E_x$ )	34.17 [MPa]
Young's modulus in y-direction ( $E_y$ )	25.42 [MPa]
Shear modulus ( $G_{xy}$ )	0 [MPa]
Poisson ratio in x-direction ( $\nu_x$ )	0.37
Poisson ratio in y-direction ( $\nu_y$ )	0.5
Membrane thickness (h)	1 [mm]

Figure 6.8 shows the deflection contour plot obtained using the energy method. In this model the maximum midpoint deflection is 23.80 mm. Figure 6.9 offers a graphical depiction of the inverted shell geometry.

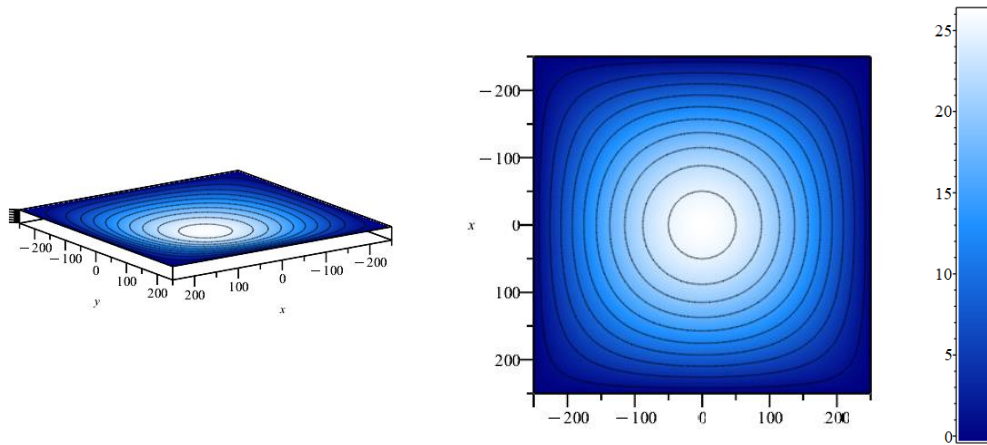


**Figure 6.8:** Contour plots of membrane deflection in mm, according to the energy-method

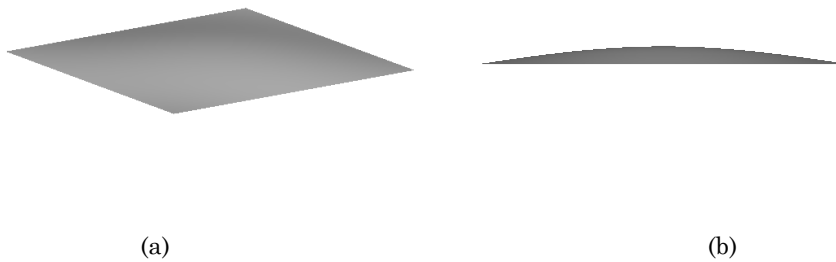


**Figure 6.9:** Resulting shell geometry, according to the energy-method

### 6.2.3 Measurement and comparison

The geometry of the structure is measured using the LiDAR scanner of an iPhone. Upon scanning the 3D object is uploaded to Rhinoceros (Figure 6.10a) for further analysis and to get the required data for the subsequent comparison step. First, the exact boundaries of the prototype within the scan are set (Figure 6.10b). Next, two lines, that represent the x- and y-axes through the centre of the element, are drawn and projected onto the mesh surface (Figure 6.10c). Finally, reference points in these curves are generated and exported for further use (Figure 6.10d).

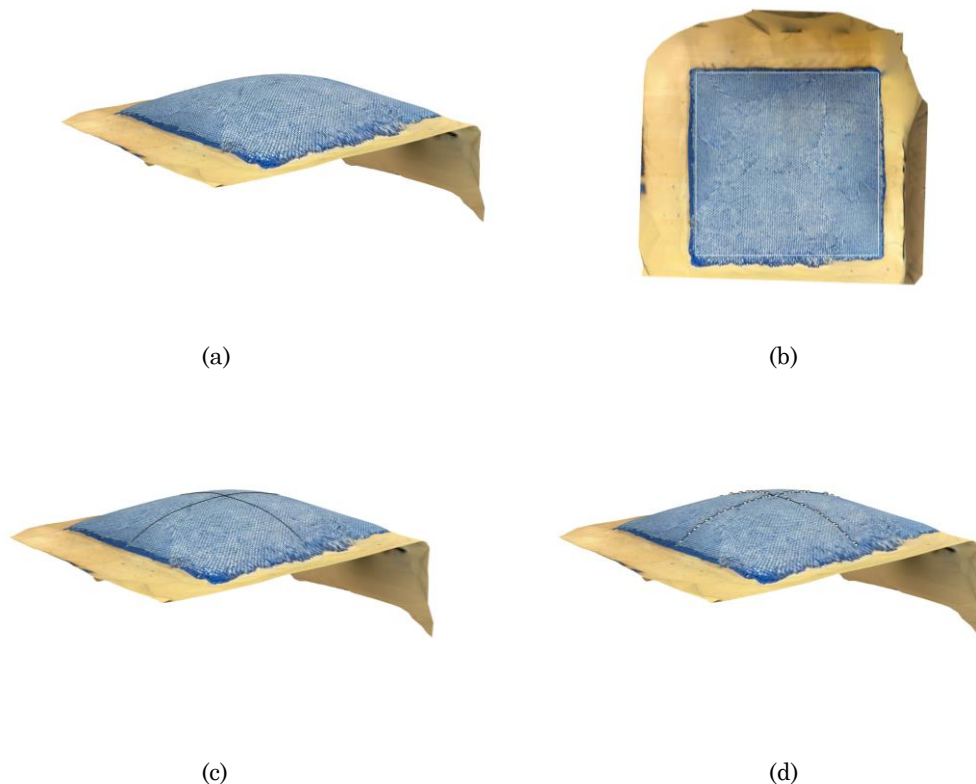


**Figure 6.10:** Geometrical measurement procedure for the squared prototype: (a) 3D object uploaded to Rhinoceros; (b) boundaries are set; (c) biaxial symmetry lines are drawn and projected onto the mesh surface; (d) reference points are generated.

The next step involves comparing the results derived from both the linear membrane deflection model and the energy-method membrane deflection model with the actual geometry measurements. First, the deflection curves along the symmetry axis are plotted. Additionally, a catenary curve is plotted to represent the theoretical funicular shape. The primary focus is on the magnitude of the maximum deflections and the shapes of these curves. This allows for a comprehensive assessment of the models' accuracy and alignment with the physical measurements.

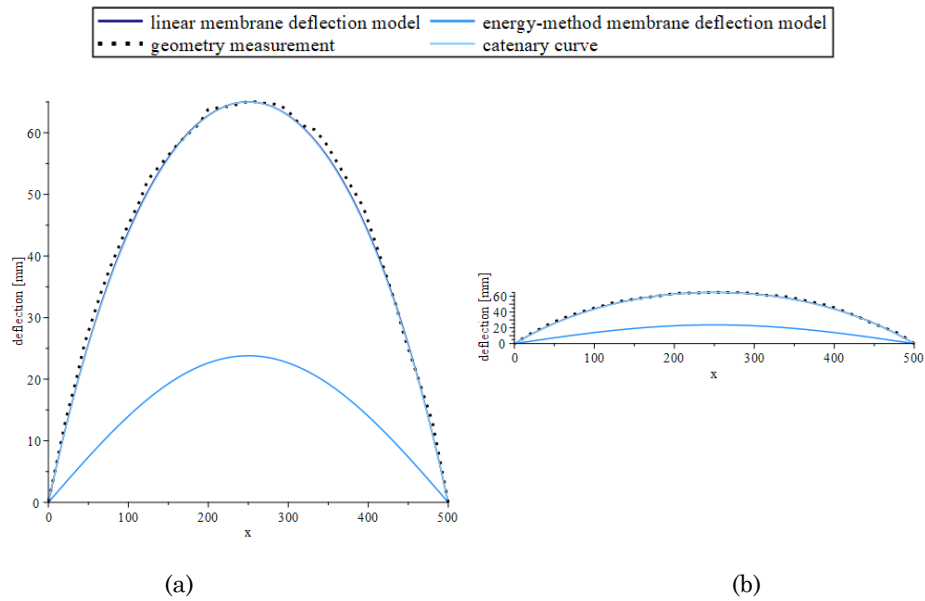


**Figure 6.11:** The deflection curves along the x-axis: (a) enlarged graph; (b) 1:1 scale graph.

The deflection curves along the x-axis (Figure 6.11) reveal that the linear model yields remarkably similar outcomes when compared to the physical measurements. Specifically, the maximum deflection predicted by the model is 65.02 mm, closely aligning with the measured value of 65.14 mm. On closer examination of the shape, minor distinctions are noticeable between the catenary curve and the parabolic curve resulting from the linear model. In contrast, the maximum deflection predicted by the energy-method model diverges significantly from the physical measurements. Moreover, it deviates from the anticipated catenary shape. This discrepancy can be attributed to the sinusoidal nature of the results obtained from the energy-method approach.



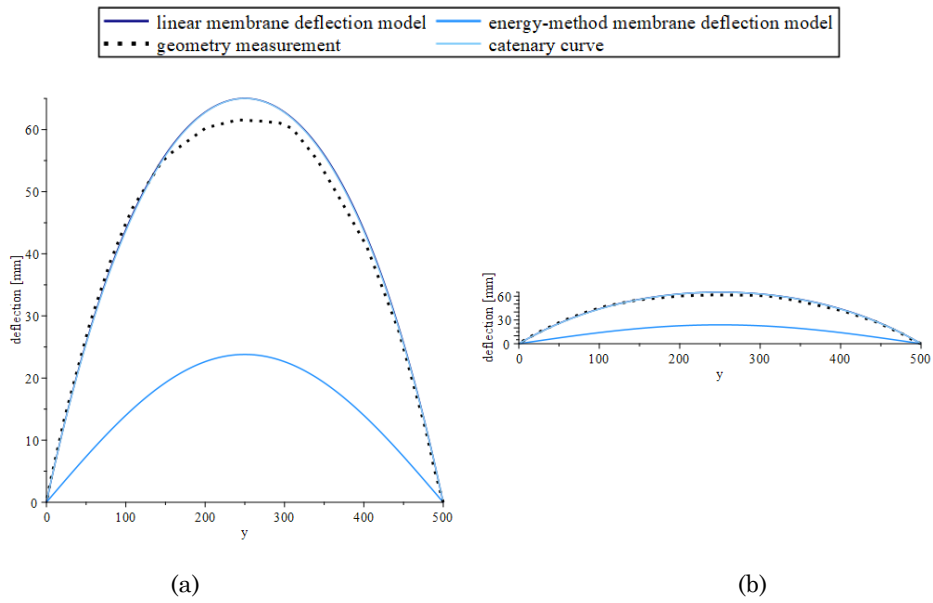


**Figure 6.12:** The deflection curves along the y-axis: (a) enlarged graph; (b) 1:1 scale graph.

The same steps are applied to examine the curves in the y-direction (Figure 6.12). In this instance, the maximum deflection measured (61.56 mm), along with the shape of the measurement curve, exhibits slight disparities when compared to the model. These discrepancies can be ascribed to the measurement's accuracy, as the original 3D model integrates interpolations, potentially resulting in disregarded reference points during the projection process. As anticipated, the energy-method model again diverges significantly from the physical measurements.

## 6.3 Rectangular shell



**Figure 6.13:** Finished rectangular shell prototype

### 6.3.1 Design

To evaluate the accuracy of the models for geometries with different dimensions in x-, and y-direction, this second shell is constructed. In this case a length-to-width ratio of 1:2 is chosen, resulting in a length of 500 mm and a width of 250 mm. The height is set at 17 mm. To obtain the deflection that provides this desired height, a mortar layer thickness of 10 mm is adopted.

### 6.3.2 Model

The linear model used for predicting the deflection behaviour of this prototype uses the same input parameters as the ones used for the squared prototype (see Table 6.1). The only difference being the width (a) is now 250 mm.

Figure 6.14 displays the deflection contour plot generated by the linear membrane model, projecting a maximum deflection of 17.54 mm at the membrane's midpoint. The visual representation of the inverted shell geometry is presented in Figure 6.15.

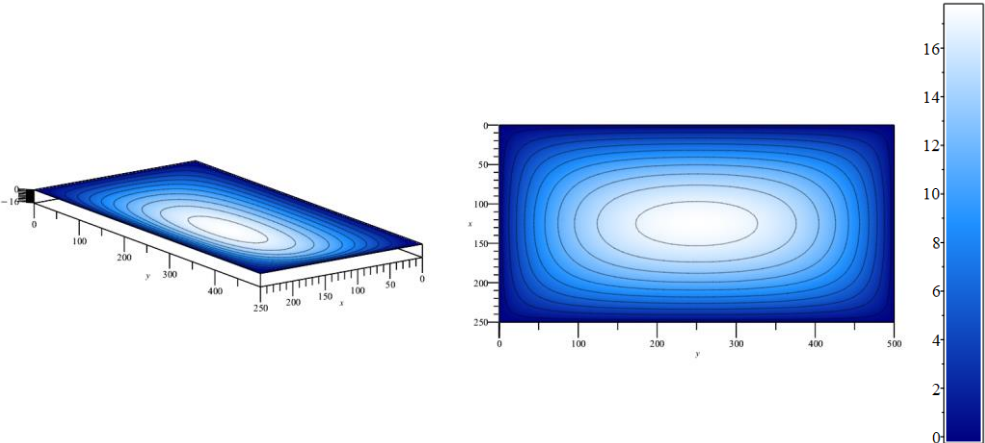


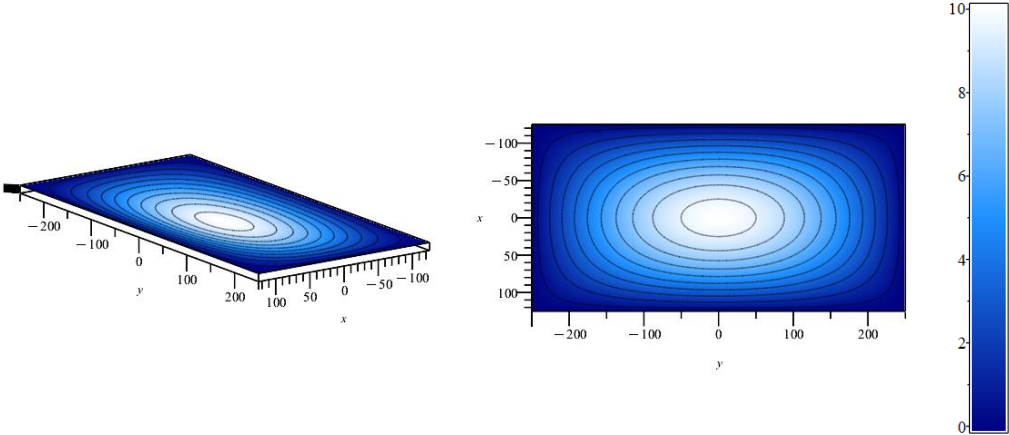
Figure 6.14: Contour plots of membrane deflection in mm, according to the linear model



Figure 6.15: Resulting structure after inverting model: (a) perspective view; (b) elevation view

The energy-method used for this geometry uses the same additional input parameters, as detailed in Table 6.2.

Figure 6.16 illustrates the deflection contour plot derived from the energy method. This model predicts a maximum midpoint deflection of 9.98 mm. Figure 6.7 illustrates the shell geometry after inversion.



**Figure 6.16:** Contour plots of membrane deflection in mm, according to the energy method

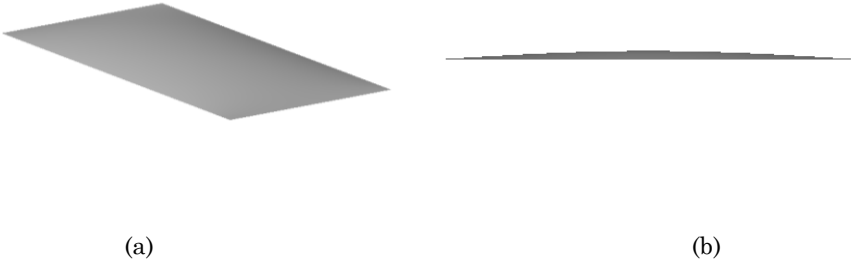


**Figure 6.17:** Resulting structure after inverting model: (a) perspective view; (b) elevation view

### 6.3.3 Measurement and comparison

The same measurement procedure that was used for the squared prototype is used for the rectangular prototype. Figure 6.18 gives an overview.

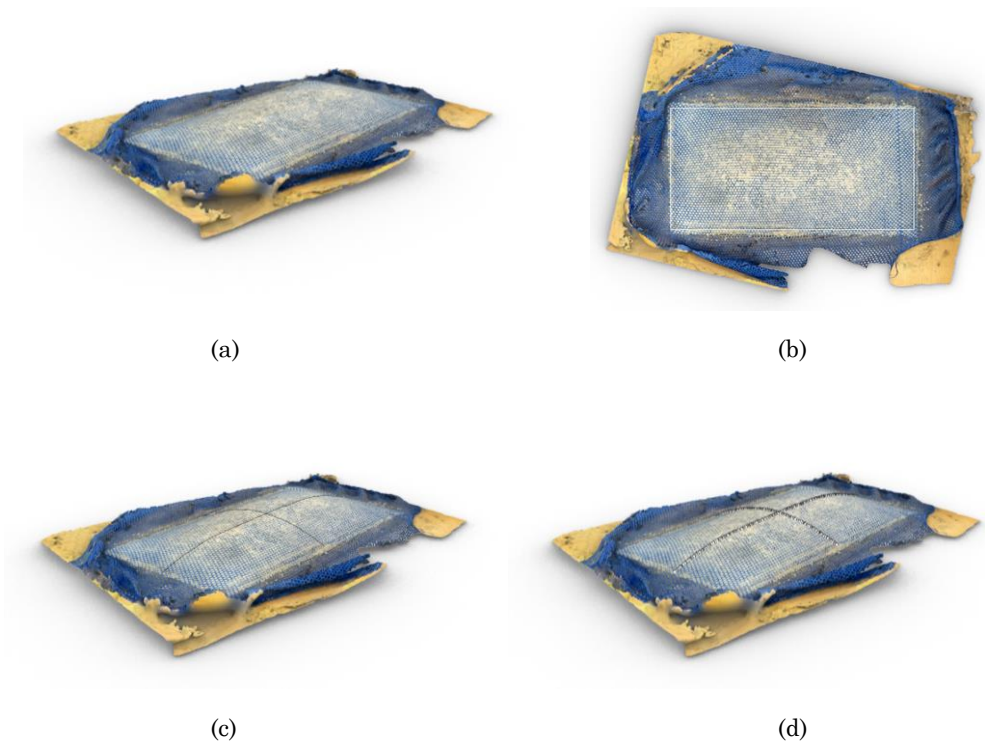


**Figure 6.18:** Geometrical measurement procedure for the squared prototype: (a) 3D object uploaded to Rhinoceros; (b) boundaries are set; (c) biaxial symmetry lines are drawn and projected onto the mesh surface; (d) reference points are generated.

The plots of the different deflection curves in x-, and y-direction are given in Figures 6.19 and 6.20.

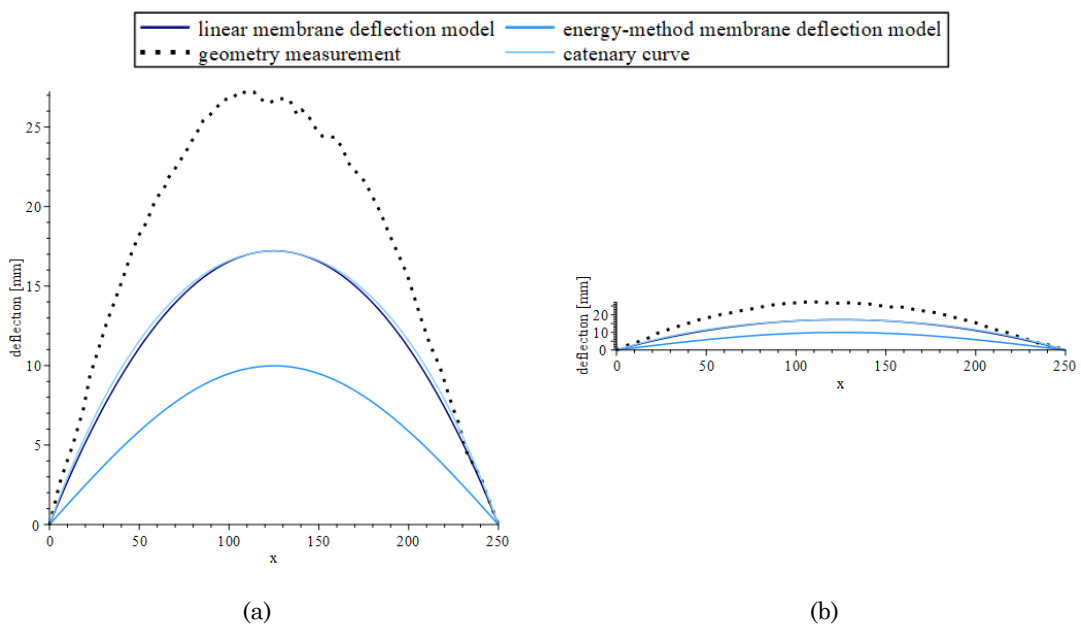


**Figure 6.19:** The deflection curves along the x-axis: (a) enlarged graph; (b) 1:1 scale graph.

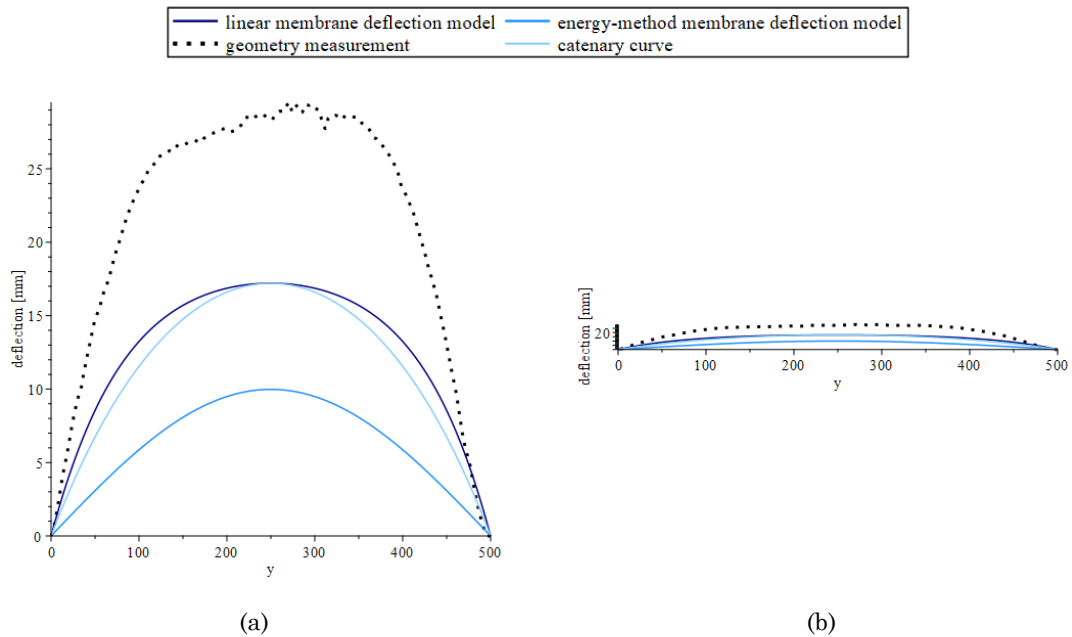


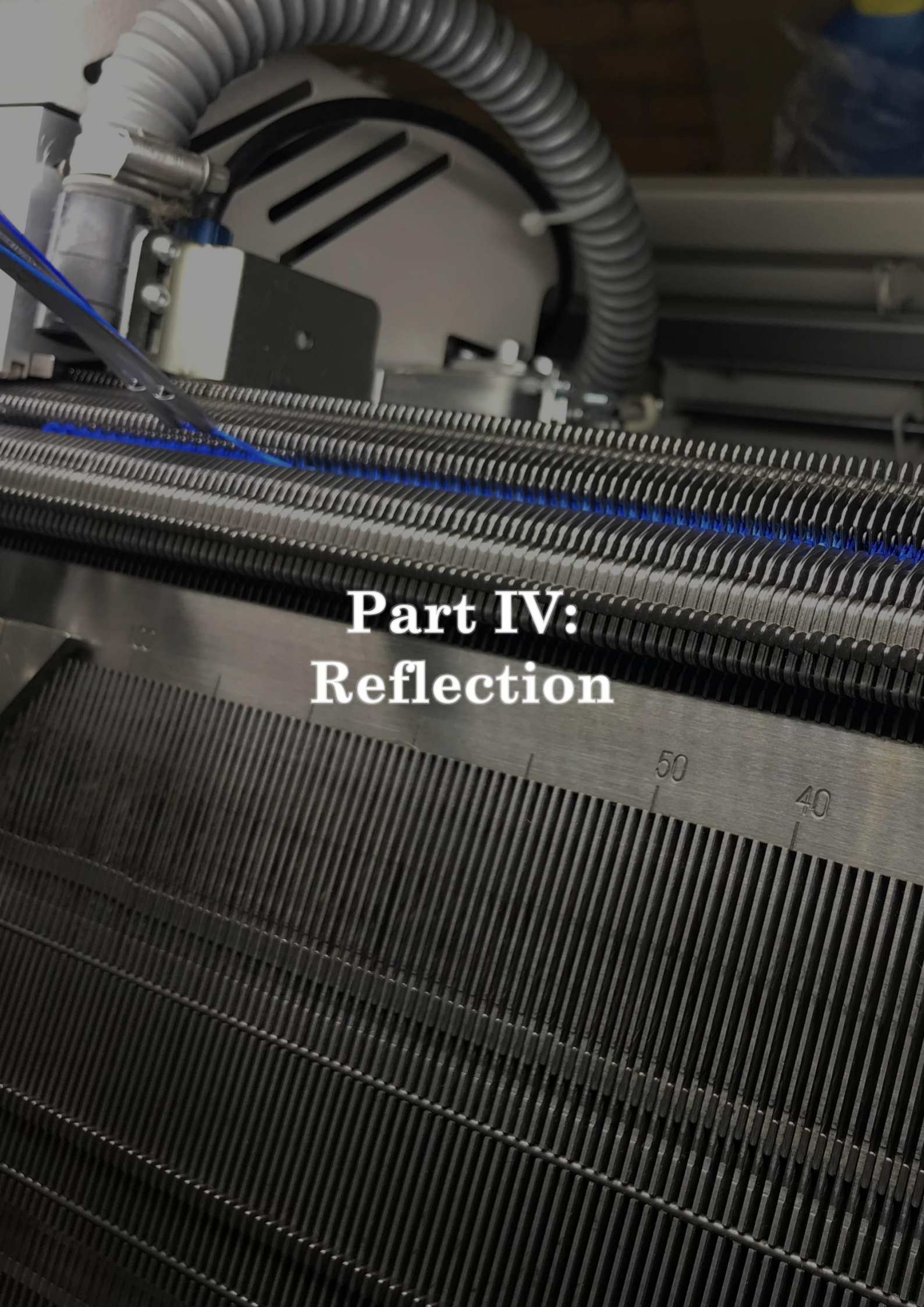
**Figure 6.20:** The deflection curves along the y-axis: (a) enlarged graph; (b) 1:1 scale graph.

For the rectangular element, the linear model results yield less accurate outcomes when compared to the squared prototype. The maximum deflection predicted by the model is 17.21 mm, whereas the deflection curves in the x- and y-direction, based on the physical measurements, record maximum values of 27.24 mm and 29.37 mm, respectively. In terms of shape, the parabolic curve obtained from the linear model demonstrates only slight deviation from the theoretical catenary shape in the x-direction. However, in the y-direction, the discrepancy between the parabolic and catenary shapes is more pronounced. This variation can be attributed to the relatively low height-to-span ratio of the element. The remaining observations align with those reported for the squared element. Namely, the maximum deflection predicted by the energy-method model diverges significantly from the physical measurements. Moreover, the sinusoidal curve shape resulting from the energy-method approach substantially deviates from the theoretical catenary shape.

## 6.4 Discussion

The observed large deflections and corresponding steep slopes in the knitted formworks signify that nonlinear deformations have indeed taken place, making the assumptions of the linear model invalid. Consequently, the correspondence of results from the linear model with the experimental findings for the square geometry appear counterintuitive. In contrast, the disparity between the linear model and physical measurements for the rectangular geometry aligns more logically with the observed nonlinear behaviour, providing a clearer understanding of the discrepancy.





**Part IV:  
Reflection**

50

40





## 7. Discussion

This chapter serves as a critical thought experiment aimed at examining the practical applications of the research findings. Section 7.1 focuses on how the membrane modelling can be used in the design of structures in a general context. This section provides insights into the potential impact of applying these findings to structural engineering. In parallel, Section 7.2 concentrates on the specific application of the forming system in the construction of concrete structures, showcasing tangible real-world applications of the research outcomes.

### 7.1 Design

This thesis has successfully demonstrated the feasibility of approximating the deformed configuration of flexibly formed concrete elements. In addition to the straightforward funicular designs characterized by simple boundary conditions, as presented in Chapter 6, the membrane models are also capable of predicting more intricate shapes, as depicted in Figure 7.1. The ability to model these diverse geometries through (semi-)analytical methods significantly enriches the array of design options available, thereby offering novel avenues for innovation and optimization in structural engineering and design. Furthermore, similar to Sergio Musmeci's innovative use of soap films to gain insights into stress flow within shells, as discussed in Chapter 2, the results obtained from the membrane models can provide similar insights throughout the structural design process.

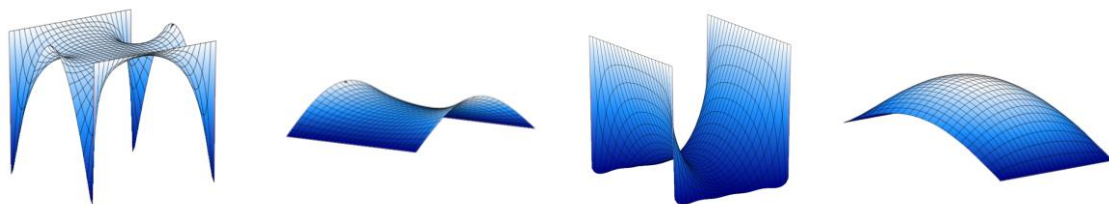


**Figure 7.1:** Examples of various design that can be obtained from the membrane models

## 7.2 Construction

The proposed forming system demonstrates promise for practical application within the construction industry, particularly in the realm of horizontal elements such as floors and roofs. The system's efficacy hinges on its ability to facilitate the efficient and precise formation of these critical structural components. Through a comprehensive assessment of its potential applications in construction, the system's suitability and advantages will be rigorously evaluated. This evaluation will consider factors such as material compatibility, cost-effectiveness, and ease of implementation to ascertain its viability as a reliable solution for horizontal element construction.

The proposed method offers two distinct implementation approaches. The first approach involves using the forming method for the construction of scaled up versions of the elements presented in Chapter 6. However, there are inherent limitations related to human dimensions, the strength of the knitted textile, and the practicality of flipping these elements that restrict their size to less than approximately 2 x 2 m. These smaller elements can be arranged next to one another to create larger assemblies, such as roofs. The second approach involves crafting multiple small elements, each with different geometries, which are then configured to serve as formworks. This approach enables the creation of substantial ribbed concrete elements and offers the advantage of incorporating reinforcement cages before the structural concrete is poured. Both approaches share the advantage of enabling the removal and reuse of the knitted textile formwork from the concrete, potentially requiring only a single piece of textile for the fabrication of an entire roofing or flooring system, thus enhancing sustainability and cost-effectiveness in construction practices.

## 8. Conclusions

This thesis has laid the groundwork for methods to determine the final (funicular) shape of flexibly formed concrete(-like) structures, driven by the global imperative to build more material-efficient structures. The various chapters provided the context, problem statement, and literature review supporting the stated need for accurately calculating the final deformed shape of these flexible formwork systems. Chapter 3 offered an overview of the methodological framework, elucidating the motivation for conducting tests, developing models, and constructing artefacts integral to the method. Chapter 4 presented the material characterization process applied to diverse mortar mixtures and knitting patterns. This chapter also provided test results and subsequent recommendations regarding preferred mixtures and patterns. Chapter 5 introduced (semi-)analytical models designed to predict the deflection behaviour of membrane formworks. Lastly, Chapter 6 detailed the fabrication of prototypes and their corresponding measurements to validate the models' findings. This chapter concisely summarises the thesis contributions, highlights the benefits of the proposed uncoated moulding and modelling approaches, acknowledges their limitations, and outlines possible avenues for future research.

### 8.1 Contributions

The thesis contributes to the field of design and concrete construction through the development of modelling approaches for forming systems using stay-in-place knitted moulds.

Aligned with the objective to determine the final geometry of flexibly formed concrete structures, the main contributions of the thesis can be linked back to the three main areas of work described in Chapter 3:

- material characterisation,
- membrane modelling, and
- prototyping.

The following sections will expand and detail on these contributions.

#### 8.1.1 Material characterisation

The findings presented in this thesis have established a fundamental understanding of the material behaviour of various knit architectures and mortar mixture designs. Despite

the anticipated subpar accuracy of the biaxial setup, it effectively provided essential insights into the heterogeneous and hyperelastic characteristics inherent to knitting materials. Additionally, the mortar tests have offered valuable insights into the interplay between water-to-cement ratios and the rheological attributes of cementitious mixtures, as well as their influence on the flexural and compressive strengths resulting cured mortar.

### 8.1.2 Membrane modelling

The membrane modelling part of this thesis introduced of methods for determining the response of linear and nonlinear membrane models. A modelling workflow was established to predict the deflection responses of membranes under diverse loading and geometries. The workflow consisted of deriving the equilibrium equations and solving them using (semi-)analytical approaches. This methodology enhanced the understanding regarding the underlying mechanical principles that govern deformation phenomena, providing a comprehensive framework to investigate and comprehend the intricate behaviour of membrane structures.

### 8.1.3 Prototyping

The prototypes constructed during this research project validated the accuracy of the (semi-)analytical models and the feasibility of the proposed forming system for fabricating funicular concrete structures. These prototypes successfully demonstrated the system's capacity to generate synclastic concrete(-like) structures. Furthermore, the prototypes highlighted the system's efficiency by eliminating the requirement for single-use custom formworks, thereby reducing wastage. Geometrical measurements of the prototypes played a crucial role in validating the deflection models, facilitating comparisons between the resulting shapes and those predicted by the models. Particularly, for squared structures with modest slopes, it was evident that the linear model could accurately simulate their ultimate shapes, affirming the model's precision in such scenarios.

## 8.2 Advantages

### **Mechanics comprehension**

(Semi-)analytical methods for determining the deformation behaviour of membrane structures necessitate the establishment of equilibrium equations, kinematic relationships, and constitutive relations before a solution can be obtained. Consequently, opting for (semi-)analytical approaches to compute formwork deflection as opposed to finite element methods (FEM) allows for a more profound understanding of the underlying mechanics governing deformation phenomena.

### **Simplified fabrication**

The primary aim of accurately predicting and controlling the final deformed shapes of formworks after casting, reduces the reliance on iterative empirical tests during fabrication of the knitted textile. This goal streamlines the manufacturing process by eliminating the need for repeated testing and adjustment, saving both time and resources. Moreover, it removes the need to stiffen textiles through coating. Consequently, these advantages collectively simplify the fabrication process.

### **Reusability**

The introduced forming system in this thesis is designed for prefabrication applications, eliminating the need for the knitted textile to serve as permanent stay-in-place formwork. The lack of coating makes it easier to reuse the textile. This approach enhances sustainability, as it further minimises material use and waste.

### **Geometry**

The deformations observed in flexible formworks naturally yield funicular shapes. Such synclastic geometries, which in the original KnitCrete technology are only attainable through the use of inflatables, can now be easily fabricated. The inherent synclastic shapes that result from the deformations of flexible formworks, simplify the construction process by reducing the need for specialised equipment like inflatables, thereby enhancing the versatility of architectural designs that can be realised using knitted formworks.

### **Structural efficiency**

The innate way of weft-knitted formwork to deform into a 2D catenary geometry ensures that the resulting funicular shaped concrete(-like) structure is loaded purely in compression. Consequently, the final structure fully capitalises on concrete's remarkable compressive strength while mitigating the impact of its weakness to tensile stresses. This makes it possible to potentially create exceptionally slender concrete structures, characterised by their elegant and efficient design.

## **8.3 Limitations**

### **Textile testing**

The biaxial tests conducted in this study adhere to the Japanese Standard MSAJ/M-02-1995 for biaxial testing of woven fabrics, which does not fully correspond to the material characteristics of weft-knitted textiles. Consequently, this misalignment can impact the precision of the obtained results. Furthermore, the make-shift biaxial testing setup that

is used during this research is limited in (i) size, (ii) loading precision, and (iii) loading diversity. These limitations further restrict the accuracy of the resultant data.

### **Modelling accuracy**

The linear model is constrained to scenarios characterised by small deflections during the casting process, making it independent on the specific material used for the formwork. However, as demonstrated in the experimental part of this thesis, the actual deflections are large. Consequently, it becomes crucial to consider the material of the formwork, as neglecting this factor could lead to counterintuitive and inaccurate results.

When larger deflections occur, additional strains are induced. These necessitate the inclusion of quadratic terms in the kinematic relations and the specification of material properties in the constitutive relations.

The energy-method offers an elegant analytical approach to approximate the behaviour of membranes experiencing large deflections. However, the comparative results presented in this thesis reveal that its accuracy falls below the expected standards. Consequently, it is advisable to employ the nonlinear model through a semi-analytical approach, as it is expected to provide more precise and reliable results, surpassing the limitations associated with the energy-based method.

### **Geometrical complexity**

(Semi-)analytical methods use Fourier series to define the assumed solutions of the unknown deformations. Since these series are constructed from sums of trigonometric functions, their applicability is primarily constrained to boundary conditions with rectangular shapes and simply supported configurations. Consequently, the versatility of the (semi-)analytical solution approach is restricted, as it can only effectively model a limited range of geometries adhering to these specific boundary conditions.

### **Material intricacy**

Knitting is a very heterogeneous material, with distinct material characteristics in the weft and warp directions. Additionally, this material demonstrates hyperelastic behaviour, characterised by a low initial stiffness that increases as internal tensile stresses increase. Despite the nonlinear models effectively capturing the orthotropic material properties inherent in knitted textiles, they fall short of modelling its hyperelastic stress-strain behaviour. The models proposed in this research are limited to representing constant stiffness properties, thus providing an incomplete depiction of the intricate material response of knitted textiles.

## Size

As the dimensions of the structural elements expand, they introduce complexities during the casting process. This process relies on the manual application of the cementitious mixture, however, at a certain size threshold, workers are unable to reach the central regions of the formwork effectively. Furthermore, as the dimensions increase, so do the loads exerted on the knitted textile, leading to higher stresses. Consequently, the size limit of structural elements is directly tied to the manufacturability and the ultimate strength of the textile material, which set an upper boundary for feasible element dimensions.

## 8.4 Future work

Transforming the tensioned knitted formwork into a load-bearing concrete structure represents an innovative and exciting challenge. The opportunities and limitations discussed in Section 7.2 and Section 7.3 point towards the following avenues of future research:

- advanced investigation of mechanical properties of knitted textiles using proper testing equipment,
- development of testing strategies tailored to weft-knitted textiles,
- development a numerical workflow to solve the nonlinear model using the Fourier series expansion method,
- development of a bespoke FEA tool for the deformation prediction of complex shaped flexible formwork systems with intricate material properties,
- development of automated concrete application techniques.





# Bibliography

Adapa. (2022). Adaptive moulds. <https://adapamoulds.com/>

Adriaenssens, Sigrid, Block, Philippe, Veenendaal, Diederik, Williams, & Chris. (2014). Shell Structures for Architecture: Form Finding and Optimization.

Airy, G. B. (1863). On the Strains in the interior of Beams. *Philosophical Transactions of the Royal Society*.

Anton, A., Reiter, L., Wangler, T., Frangez, V., Flatt, R. J., & Dillenburger, B. (2021). A 3D concrete printing prefabrication platform for bespoke columns. *Automation in Construction*, 122. <https://doi.org/10.1016/j.autcon.2020.103467>

Bos, F., Wolfs, R., Ahmed, Z., & Salet, T. (2016). Additive manufacturing of concrete in construction: potentials and challenges of 3D concrete printing. *Virtual and Physical Prototyping*, 11(3), 209–225. <https://doi.org/10.1080/17452759.2016.1209867>

Bruce, M., Clune, G., Xie, R., Mozaffari, S., & Adel, A. (2021). Cocoon: 3D Printed Clay Formwork for Concrete Casting.

Conway, H. D. (1946). The large deflections of rectangular membranes and plates. *The London, Edinburgh, and Dublin Philosophical Magazine and Journal of Science*, 37(274), 767–778. <https://doi.org/10.1080/14786444608521568>

DBT. (2023). Concrete Choreography. <https://dbt.arch.ethz.ch/project/concrete-choreography/>

Föppl, A. (1907). *Vorlesungen über technische Mechanik*.

FreeFAB. (2023). FreeFAB wax moulds. <https://www.freefab.com/>

García de Soto, B., Agustí-Juan, I., Hunhevicz, J., Joss, S., Graser, K., Habert, G., & Adey, B. T. (2018). Productivity of digital fabrication in construction: Cost and time analysis of a robotically built wall. *Automation in Construction*, 92, 297–311. <https://doi.org/10.1016/J.AUTCON.2018.04.004>

Gibbons, O., & Orr, J. J. (2020). How to calculate embodied carbon. Institution of Structural Engineers (Great Britain).

Hack, N., & Kloft, H. (2020). Shotcrete 3D Printing Technology for the Fabrication of Slender Fully Reinforced Freeform Concrete Elements with High Surface Quality: A Real-Scale Demonstrator. In *RILEM Bookseries* (Vol. 28, pp. 1128–1137). Springer. [https://doi.org/10.1007/978-3-030-49916-7\\_107](https://doi.org/10.1007/978-3-030-49916-7_107)

Happold, E., & Liddell, W. I. (1975). Timber lattice roof for the Mannheim Bundesgartenschau.

## Bibliography

- Ingold, L., & Rinke, M. (2015). Sergio Musmeci's search for new forms of concrete structures.
- Jipa, A., & Dillenburger, B. (2022). 3D Printed Formwork for Concrete: State-of-the-Art, Opportunities, Challenges, and Applications. *3D PRINTING AND ADDITIVE MANUFACTURING*, 9. <https://doi.org/10.3929/ethz-b-000507436>
- Kloft, H., Krauss, H. W., Hack, N., Herrmann, E., Neudecker, S., Varady, P. A., & Lowke, D. (2020). Influence of process parameters on the interlayer bond strength of concrete elements additive manufactured by Shotcrete 3D Printing (SC3DP). *Cement and Concrete Research*, 134. <https://doi.org/10.1016/j.cemconres.2020.106078>
- Kloft, H., Lowke, D., & Hack, N. (2019). An innovative and efficient technology for 3d printing of large-scale concrete components at TU Braunschweig.
- Lamberton, B. A. (1989). Fabric forms for concrete. 58–67.
- Lee, M. (2023). Concrete structures with stay-in-place flexible formwork and integrated tex-tile reinforcement - An exploration of the design space and mechanical behaviour. Institute of Structural Engineering.
- Lee, M., Mata-Falcón, J., Popescu, M., Block, P., & Kaufmann, W. (2020). Potential Approaches for Reinforcing Complex Concrete Structures with Integrated Flexible Formwork. *Second RILEM International Conference on Concrete and Digital Fabrication*, 28, 669–679. [https://doi.org/https://doi.org/10.1007/978-3-030-49916-7\\_67](https://doi.org/https://doi.org/10.1007/978-3-030-49916-7_67)
- Leissa, A. W., & Qatu, M. S. (2011). *Vibrations of Continuous Systems*.
- Levy, S. (1942). Bending of rectangular plates with large deflections.
- Linkwitz, K., & Schek, H.-J. (1971). *Einige Bemerkungen zur Berechnung von vorgespannten Seilnetzkonstruktionen*. Springer-Verlag.
- Mata-Falcón, J., Bischof, P., Huber, T., Anton, A., Burger, J., Ranaudo, F., Jipa, A., Gebhard, L., Reiter, L., Lloret-Fritschi, E., Van Mele, T., Block, P., Gramazio, F., Kohler, M., Dillenburger, B., Wangler, T., & Kaufmann, W. (2022). Digitally fabricated ribbed concrete floor slabs: a sustainable solution for construction. *RILEM Technical Letters*, 7, 68–78. <https://doi.org/10.21809/rilemtechlett.2022.161>
- Nguyen, T. N., Hien, T. D., Nguyen-Thoi, T., & Lee, J. (2020). A unified adaptive approach for membrane structures: Form finding and large deflection isogeometric analysis. *Computer Methods in Applied Mechanics and Engineering*, 369. <https://doi.org/10.1016/j.cma.2020.113239>
- Nikishkov, G. P. (2004). Introduction to the finite element method.
- Ochsendorf, J., & Kilian, A. (2005). Particle-spring systems for structural form finding. In *Article in Journal of the International Association for Shell and Spatial Structures*. <https://www.researchgate.net/publication/279894928>

- Orr, J. J. (2010). Innovative concrete structures using fabric formwork. SEMC. <https://www.researchgate.net/publication/265420800>
- Orr, J. J., Darby, A. P., Ibell, T. J., Evernden, M. C., & Otlet, M. (2011). Concrete Structures Using Fabric Formwork. *Structural Engineer*, 89(8), 20–26. <https://doi.org/10.17863/CAM.17019>
- Otto, F., & Rasch, B. (1995). *Frei Otto, Bodo Rasch: Finding Form*.
- Popescu, M. (2019). *KnitCrete - Stay-in-place knitted formworks for complex concrete structures*. ETH Zürich.
- Popescu, M., Reiter, L., Liew, A., Van Mele, T., Flatt, R. J., & Block, P. (2018). Building in Concrete with an Ultra-lightweight Knitted Stay-in-place Formwork: Prototype of a Concrete Shell Bridge. *Structures*, 14, 322–332. <https://doi.org/10.1016/j.istruc.2018.03.001>
- Popescu, M., Rippmann, M., Liew, A., Reiter, L., Flatt, R. J., Van Mele, T., & Block, P. (2021). Structural design, digital fabrication and construction of the cable-net and knitted formwork of the KnitCandela concrete shell. *Structures*, 31, 1287–1299. <https://doi.org/10.1016/j.istruc.2020.02.013>
- Ramm, E. (1991). *Shape finding methods of shells*.
- Ranaudo, F., van Mele, T., & Block, P. (2021). A low-carbon, funicular concrete floor system: Design and engineering of the HiLo floors. *IABSE Congress, Ghent 2021: Structural Engineering for Future Societal Needs, 2016–2024*. <https://doi.org/10.2749/ghent.2021.2016>
- Sakagami, H., Okawa, H., Nakamura, M., Anabuki, T., Ishizeki, Y., & Kaneko, T. (2020). *Design and Construction of Shell-shaped Bench using a 3D Printer for Construction (Vol. 2020)*.
- Scheder-Bieschin, L., Spiekermann, K., Popescu, M., Bodea, S., Van Mele, T., & Block, P. (2023). Design-to-Fabrication Workflow for Bending-Active Gridshells as Stay-in-Place Falsework and Reinforcement for Ribbed Concrete Shell Structures. In *Towards Radical Regeneration* (pp. 501–515). Springer International Publishing. [https://doi.org/10.1007/978-3-031-13249-0\\_40](https://doi.org/10.1007/978-3-031-13249-0_40)
- Schipper, H. R., Grünewald, S., Eigenraam, P., Raghunath, P., & Kok, M. A. D. (2015). Production of Curved Precast Concrete Elements for Shell Structures and Free-form Architecture using the Flexible Mould Method.
- Schneider, M., Romer, M., Tschudin, M., & Bolio, H. (2011). Sustainable cement production-present and future. In *Cement and Concrete Research (Vol. 41, Issue 7, pp. 642–650)*. Elsevier Ltd. <https://doi.org/10.1016/j.cemconres.2011.03.019>
- Seide, P. (1977). Large deflections of rectangular membranes under uniform pressure. *Int. J. Non-Linear Mechanics*, 12, 397–406.

## Bibliography

Swilling, M., Hajer, M., Baynes, T., Bergesen, J., Labbé, F., Kaviti Musango, J., Ramaswami, A., Robinson, B., Salat, S., & Suh, S. (2018). The weight of cities: re-resource requirements of future urbanization. <http://postfossil.city/en/finalists/african-alternativesandwww.karlschulschenk.com/@karlschulschenk>.

Tamke, M., Deleuran, A., Gengnagel, C., Schmeck, M., Cavalho, R., Fanguero, R., Monteiro, F., Stranghöner, N., Uhlemann, J., Homm, T. H., & Ramsgaard Thomsen, M. (2015). Designing CNC Knit for Hybrid Membrane and Bending Active Structures. <http://cita.karch.dkwww.arch.udk-berlin.dewww.uni-due.de/iml/>

Timoshenko, S., & Woinowsky-Krieger, S. (1985). Theory of plates and shells.

Uratani, J. M., & Griffiths, S. (2023). A forward looking perspective on the cement and concrete industry: Implications of growth and development in the Global South. In *Energy Research and Social Science* (Vol. 97). Elsevier Ltd. <https://doi.org/10.1016/j.erss.2023.102972>

Veenendaal, D. (2017). Design and form finding of flexibly formed concrete shell structures.

Ventsel, E., & Krauthammer, T. (2001). *Thin Plates and Shells; Theory, Analysis, and Applications*; Edition 1. <https://doi.org/10.4324/9780429221316>

Walia, K., Oval, R., & Baverel, O. (n.d.). F.A.B Shell (Fabric -Arch -Base Shell) : Concrete Shell Building using Fabric Membranes and Telescopic Arches as Formwork. <https://www.researchgate.net/publication/354648016>

Wangler, T., Lloret, E., Reiter, L., Hack, N., Gramazio, F., Kohler, M., Bernhard, M., Dillenburger, B., Buchli, J., Roussel, N., & Flatt, R. (2016). Digital concrete: Opportunities and challenges. *RILEM Technical Letters*, 1, 67–75. <https://doi.org/10.21809/rilemtechlett.2016.16>

West, M. (2017). *The fabric formwork book: methods for building new architectural and structural forms*.